VNIVERSITAT DE VALÈNCIA

DEPARTAMENT D'ÒPTICA

INVERSE NONLINEAR DESIGN IN SILICON WAVEGUIDES

DOCTORAL THESIS

David Castelló Lurbe

September 2014

VNIVERSITAT DE VALÈNCIA

DEPARTAMENT D'ÒPTICA

INVERSE NONLINEAR DESIGN IN SILICON WAVEGUIDES

Tesi desenvolupada al
Programa de Doctorat en Física per

DAVID CASTELLÓ LURBE

dirigida per

PROF. ENRIQUE SILVESTRE MORA i
PROF. VÍCTOR TORRES COMPANY

Setembre 2014

Inverse nonlinear design in silicon waveguides

David Castelló Lurbe
Departament d'Òptica, Universitat de València, 46100 Burjassot (Spain)

Abstract

Silicon based platforms offer, among other advantages, great possibilities to develop nonlinear applications. Particularly, the design of a silicon-on-insulator (SOI) waveguide for supercontinuum (SC) generation pumping at telecom wavelengths will be proposed in this thesis. In spite of this fact, this work addresses the design of waveguides from a wider approach.

On the one hand, the generalized nonlinear Schrödinger equation is theoretically analyzed and an analytical model is proposed to study new frequency generation by means of optical wave-breaking (OWB). This strategy allows to calculate the higher-order dispersion required to optimize the spectral broadening during OWB, as well as the frequencies of the radiated dispersive waves. Although it is an approximate model, it becomes very useful to relate the parameters involved in realistic waveguides, often exclusively studied by means of numerical simulations.

On the other hand, our second goal is to find a waveguide where the above phenomenon takes place. Dispersion engineering becomes a time-consuming task if several geometric degrees of freedom are available. Here, inverse dispersion engineering through an iterative procedure is applied. At each step, new values for all the parameters providing dispersion profiles closer to the target are determined based on an analytical expression for the derivatives of the propagation constant. These homemade tools lead to a slot SOI waveguide with the suitable properties to induce a coherent near octave spanning SC generation based on OWB pumping at telecom wavelengths.

Keywords: Silicon-on-insulator waveguides, supercontinuum generation, generalized nonlinear Schrödinger equation, optical wave-breaking, dispersive waves, inverse dispersion engineering.

List of Publications

This thesis is based on the following appended papers:

I. D. Castelló-Lurbe, E. Silvestre, P. Andrés i V. Torres-Company, "Spectral broadening enhancement in silicon waveguides through pulse shaping," Opt. Lett. **37**, 2757–2759 (2012).

II. D. Castelló-Lurbe, P. Andrés, and E. Silvestre, "Dispersion-to-spectrum mapping in nonlinear fibers based on optical wave-breaking," Opt. Express **21**, 28550–28558 (2013).

III. V. Torres-Company, D. Castelló-Lurbe, and E. Silvestre, "Comparative analysis of spectral coherence in microresonator frequency combs," Opt. Express **22**, 4678–4691 (2014)

IV. D. Castelló-Lurbe, V. Torres-Company, and E. Silvestre, "Inverse dispersion engineering in silicon waveguides," to appear in J. Opt. Soc. Am. B. **31**.

V. D. Castelló-Lurbe, V. Torres-Company, and E. Silvestre, "Supercontinuum generation based on resonant optical wave-breaking", to be published.

Agraïments

M'agradaria donar les gràcies als directors d'aquesta tesi, Enrique Silvestre i Víctor Torres-Company. Al primer, per les nombroses discussions científiques i en relació a la ciència, totes dues sempre productives, així com la confiança dipositada en mi. Al segon, per haver marcat un punt d'inflexió a la meua tesi, dirigint-la cap a l'àrea de la fotònica del silici. També vull manifestar-li la meua gratitud per ampliar la meua visió de la ciència, estimulant la nostra participació directa a la comunitat científica, així com fer possible la meua estada a Chalmers University of Technology (Goteborg, Suècia). No voldria oblidar-me de Pedro Andrés, qui, amb bon criteri, fou el promotor d'aquesta sinèrgia i coautor de part dels treballs d'aquesta tesi. La seua afabilitat, així com l'atenció i preocupació per cadascun dels estudiants, són sempre de valor. Una tesi doctoral és un projecte a llarg termini. Transcorre, indefectiblement, per diferents etapes, els condicionants de les quals són difícilment predictibles. Mereix, per tant, ser avaluada globalment. Així, tot plegat, acabe amb la convicció d'haver estat afortunat per les circumstàncies que l'han emmarcada.

Vull també donar les gràcies a Mariola Brines per la seua revisió gramatical del capítol introductori d'aquesta tesi.

També vull agrair als meus pares la confiança, els valors i les oportunitats que m'han proporcionat per optar a aquest títol de doctor. I no puc oblidar-me de la meua estimada Sara, amb qui he compartit tots aquestos anys de tesi.

Amb el permís del seu autor, acabe aquestos agraïments amb el següent comentari: "La investigació, un punt d'equilibri entre el plaer intel·lectual i la productivitat". Almenys aquesta tesi ha pogut ser completada tenint aquesta idea ben present. I això també és d'agrair.

Aquest treball ha estat finançat fonamentalment pel contracte predoctoral VALi+d de la Generalitat Valenciana (2010-2014). Cal agrair també el suport econòmic procedent del Plan Nacional I+D+i sota el projecte TEC2008-05490 del Ministerio de Ciencia e Innovación (España), de l'ajuda PROMETEU 2009-077 i de l'Swedish Research Council (VR).

"Say, Pop, I noticed something: When I pull the wagon the balls rolls to the back of the wagon, and when I'm pulling it along and I suddenly stop, the ball rolls to front of the wagon," and I say, "why is that?" And he said, "That nobody knows", he said. "The general principle is that things that are moving try to keep on moving and things that are standing still tend to stand still unless you push on them hard". And he says, "This tendency is called inertia but nobody knows why it's true." Now that's a deep understanding– he didn't give me a name, he knew the difference between knowing the name of something and knowing something."
(Richard P. Feynman: *The pleasure of finding things out*, Perseus Books Group, New York, 1999)

Summary (in Catalan)

La tecnologia fotònica basada en silici és objecte d'intensa investigació tant al món acadèmic com a la indústria. Un dels seus principals atractius rau en la seua elevada compatibilitat amb tècniques ja desenvolupades per a la integració de circuits electrònics, cosa que podria reduir el seu cost. A més, el silici ofereix una gran diversitat d'efectes no lineals que poden ser aprofitats per processar senyals òptics en xips compactes a velocitats superiors als dispositius electrònics actuals. En particular, l'objectiu d'aquesta tesi ha estat dissenyar una guia integrada en una plataforma híbrida de silici i sílice per generar espectres supercontinus. Aquest projecte presentava diferents reptes que calia superar. En primer lloc, la presència de mecanismes d'absorció no lineals inherents a l'estructura material del silici que limiten, en gran mesura, la capacitat d'eixamplament espectral d'aquest tipus de guies. En segon lloc, la preferència per treballar en condicions que preserven, en qualsevol cas, la robustesa del sistema front a fluctuacions del senyal d'entrada excloïa l'ús de certs mecanismes d'alta eficiència de generació de noves freqüències. Per últim, calia desenvolupar un procediment sistemàtic per determinar dissenys realistes de seccions transversals de guia on tinguera lloc la fenomenologia buscada. Malgrat que aquesta tesi no incorpora resultats experimentals, les seues conseqüències pràctiques són paleses i en justifiquen el seu interés.

El plantejament aplicat per assolir aquestos objectius contenia dues vies d'estudi. Per una banda, les simulacions numèriques basades en models ben establerts foren clau per avaluar la viabilitat de les nostres propostes. Per altra banda, tot model físic es caracteritza per una série de paràmetres que descriuen el sistema real l'evolució del qual és analitzada. Lògicament, la dinàmica d'un sistema no està només determinada per l'estructura matemàtica del model que el descriu, sinó també per les seues característiques físiques. En aquest sentit, part dels nostres esforços foren destinats al desenvolupament d'eines teòriques que proporcionen un coneixement quantitatiu de les característiques

que deuen mostrar els sistemes perquè determinats processos hi esdevinguen. Ja que aquest tipus d'anàlisi està lligat a equacions generals, i no només a sistemes experimentals concrets, una part important de la introducció d'aquesta tesi ha estat dedicada a l'estudi detallat de les hipòtesis en què se sustenten. En particular, he remarcat les implicacions físiques lligades a un tractament pertorbatiu de la no linealitat d'un sistema (concretament, la propagació unidireccional i monomode de polsos de llum). A més, he modelitzat la no linealitat fent ús de l'anomenat senyal analític del camp, cosa que ha permés identificar interaccions no lineals addicionals (com la suma de tercer ordre de freqüències o la radiació ressonant negativa) que, habitualment, són negligides. Aquest desenvolupament ha proporcionat un enfoc més ampli al model de propagació no lineal que apliquem en aquesta tesi, a més d'oferir noves propostes per a futurs treballs.

Aquestes idees constitueixen el marc on s'inscriu el nostre procediment de disseny no lineal invers, des del punt de vista del qual, l'Article V, que inclou la nostra proposta per assolir l'objectiu plantejat en aquesta tesi, és una aplicació. Els avanços teòrics que requerí aquest treball final foren presentats a l'Article II, on el disseny no lineal és, pròpiament, abordat; i a l'Article IV, que comportà la implementació d'un programa per al càlcul de les seccions transversals que satisfan les propietats físiques desitjades. Així, presente a continuació els aspectes clau dels mètodes que hem desenvolupat i que, finalment, han estat aplicats amb èxit per assolir els fins d'aquesta tesi.

La propagació no lineal de polsos a guies pot ser descrita a través de l'anomenada equació no lineal d'Schrödinger generalitzada. Aquest model és vàlid posat que la contribució no lineal siga una pertorbació de l'índex efectiu i que s'excite un únic mode de la guia. Des d'una perspectiva matemàtica, un coneixement analític de les solucions d'aquesta equació és només possible sota condicions sovint allunyades de les exigides perquè es produesca un vast eixamplament espectral. Amb la motivació d'extraure alguna mena d'informació quantitativa entorn d'aquesta física, a l'Article II considerarem una llei de conservació, generalment aplicada per a una *dispersió de la velocitat de grup* (GVD) constant, per a guies amb una GVD arbitrària. Per completesa, he incorporat a la introducció d'aquesta tesi una versió més general que també inclou una dispersió arbitrària del coeficient no lineal de la guia. La interpretació física de les funcions involucrades que proposarem em permeté construir un model analític simplificat de la propagació d'un pols que experimenta el procés d'*optical wave-breaking* (OWB). Aquest tractament obrí les portes per calcular quina deu ser la corba de dispersió d'una guia perquè l'eixamplament espectral induït per aquest procés siga realment eficient. És, precisament, la disponibilitat d'una expressió analítica que relaciona l'eficiència de la generació de

noves freqüències durant el procés d'OWB amb les característiques dispersives de la guia, la que fa possible invertir el procés i deduir quin és el perfil de la dispersió adient per reproduir l'anterior comportament. Aquests resultats foren presentats a l'Article V.

És evident que el plantejament que acabe d'exposar resulta incomplet si no es proporciona una estructura que oferesca la dispersió deduïda. Aquest és, en realitat, un nou problema de disseny invers. En relació a aquest tipus de tasques, el nostre grup ja havia fet importants avanços durant els últims anys. Tanmateix, havien estat aplicats per a fibres de cristall fotònic (PCF). La plataforma de silici i sílice (silici sobre aïllant o SOI) presenta un alt contrast d'índex, a diferència de les PCF, tret que té incidència als càlculs involucrats a les tasques de disseny invers. A l'Article IV, es deduí una expressió, a partir d'un resultat teòric previ del grup, que permet calcular les derivades de la constant de propagació respecte dels diferents paràmetres geomètrics, aplicable també per a guies d'alt contrast d'índex. En aquest cas, però, resultà clau atendre a les condicions de contorn del camp elèctric. Aquests càlculs s'implementaren amb èxit i feren possible l'obtenció de dissenys realistes amb diferents tipus de perfils de la dispersió. En particular, dissenyàrem una secció transversal on s'induïa un eixamplament espectral molt significatiu a través del mecanisme d'OWB. Cal dir, per completesa, que el perfil del pols d'entrada té una especial relevància en aquestes guies per poder inhibir l'impacte de les pèrdues no lineals. Aquest tema fou investigat a l'Article I, on es posà de manifest la millora de l'eixamplament espectral soferta per polsos asimètrics.

Pel que fa a l'Article III, fou una col·laboració a un estudi numèric entorn de la influència del soroll a la generació de pintes de freqüència a anells microressonadors i la formació de polsos. Aquest treball entroncava directament amb el segon dels objectius abans indicats. A més a més, les eines de disseny invers també poden ser aprofitades per determinar com deu ser la secció transversal d'aquests sistemes perquè l'impacte del soroll es reduesca o millore l'estabilitat dels polsos.

A tall de conclusió, caldria emfatitzar tres aspectes d'aquesta tesi. En síntesi, he pogut calcular un disseny de guia on la producció de fonts de llum de banda ampla és possible, superant així les limitacions imposades pels processos d'absorció no lineals. Tanmateix, considere que les eines desenvolupades per arribar a aquest resultat també tenen valor en si mateix. Per un costat, el programa de disseny de seccions tranversals ofereix una gran versatilitat. De fet, aquest algoritme converteix el disseny de guies d'interfícies rectes i compostes de qualsevol tipus de materials en un procediment sistemàtic i eficient per a cadascuna de les geometries que es consideren. Per un altre costat, he comprovat que, almenys per a la dinàmica d'interés d'aquesta tesi, és possible

extraure informació física a partir de l'anàlisi de l'evolució de certes quantitats integrades que caracteritzen el pols. Aquestes funcions, a més, no comporten cap tipus de restricció sobre les característiques físiques del sistema. Més enllà de l'aplicació particular d'aquest projecte, aquest enfoc obri noves possibilitats per estudiar la propagació no lineal de polsos.

Contents

Chapter 1

Introduction

Before explaining the motivation and aim of this thesis, I would like to briefly comment what is the spirit where it relies. Nowadays, new technologies are increasingly solving human needs by taking advantage of complex physical processes, such as nonlinear light-matter interactions, having the concomitant impact on the social and economic spheres. Certainly, a detailed knowledge of these systems requires intense experimental research in each area leading to short-term applications and, subsequently, apparent benefits for the society. Despite not containing experimental results, this thesis always keeps practical purposes on mind, although, as any theoretical work, it could only produce material benefits in the mid- or even long-term. Therefore, I consider that theoretical research in engineering areas represents a necessary approach to improve our understanding of physical systems and thus enhance their usefulness.

With this aim, we lead our effort in a two-fold direction. On the one hand, numerical simulations of realistic systems will be always performed to check the feasibility of our proposals. On the other hand, we try to determine the conditions, *i.e.*, the value of the physical parameters, where the phenomena under study take place through theoretical analysis of the models. The equations will be both used as a means to simulate actual systems and also as objects of study themselves. Therefore, the applicability conditions of our conclusions will be defined by the approximations assumed in the derivation of the equations. From my point of view, this fact justifies the importance of understanding the hypothesis connected to the equations. Note that we do not pursue to resign from numerical studies but use them in a more efficient way.

All issues addressed in this dissertation arise around nonlinear pulse propagation in waveguides. In spite of the majority of our results being applied to silicon-on-insulator (SOI) waveguides, due to its relevance among the integrated photonics technologies [1], they are not restricted to this platform. The scope of our main conclusions corresponds to those systems governed by the equations we handle. For that reason, I review the derivation of both the eigenvector equation, corresponding to the electric and magnetic modes fields of a translational-invariant system, and the generalized nonlinear Schrödinger equation (GNLSE), commonly used to describe the nonlinear propagation of pulses. I especially concentrate on the assumptions made to derive the propagation equation. As many other theories, this equation can be only analytically solved for some specific cases. For example, its stationary states, the so-called solitons, can be calculated through the inverse scattering method [2] and the evolution of pulses until the so-called wave-breaking through a Madelung transform and WKB method [3]. These mathematical procedures find complete solutions of the propagation equation, namely, both the amplitude and phase of the output pulse. In addition, perturbation theory can also be applied when the pulse contains a nearly stationary solution [4, 5]. Notwithstanding, these methods always imply restrictions on the physical features of the waveguide. Particularly, this kind of complete solutions does not include arbitrary dispersion profiles. Nevertheless, this is an important property of the waveguides whose description must be carefully done when supercontinuum (SC) generation problems are addressed. Indeed, these systems are usually highly sensitive to dispersive properties across the large spectral range involved in such cases [6]. Accordingly, strategies including all dispersive orders would be desirable. On the whole, solving this equation involves a fundamental challenge from a mathematical point of view: how to treat simultaneously local terms in both the time (nonlinearities) and frequency (dispersion) domains. Its inherent complexity often demands numerical simulations for realistic systems [6]. In contrast to this full numerical strategy, where a complete knowledge of the pulse is sought, we try to obtain physical information from some integrated quantities of the pulse. These functions (that depend on z-coordinate) satisfy a conservation law of the GNLSE, that will be demonstrated in the next chapter. Their physical interpretation was proposed in Paper II, and they were successfully applied to SC generation pumped at the normal dispersion regime in Paper V.

Indeed, any practical study must relate to the physical properties (those that define the system within the theoretical framework), the geometry and the materials (properties that can be partially controlled during the fabrication process). It is worth noticing that silicon-based waveguides allow dispersion

engineering due to its high index contrast, namely, the difference between the refractive indices of the core and the cladding, that is 2 or 3 orders of magnitude higher than the index contrast of conventional fibers (we will return to this point in Chapter 3). Consequently, tools enabling control of, for example, the dispersion profile through a proper geometric design can be of great interest for this technology. Nonetheless, vectorial effects have significant impact, thus difficulting any analytical approach. In fact, trial and error procedures are usually adopted to develop design tasks [7–10]. Commercially available mode solvers allows to apply this strategy in a straightforward manner, although it becomes time-consuming when several degrees of freedom must be incorporated to obtain precise control of the dispersion. Here we take advantage of a previous theoretical result of our group [11], that was applied to the scalar case, and derive a closed expression that offers an excellent numerical precision and notably reduces the computational effort even for full-vectorial systems, such as SOI waveguides. We use this tool to find realistic designs of SOI waveguides that show several dispersion profiles matching targets initially fixed.

On the one hand, Fig. 1.1 schematically represents the perturbative treatment commonly applied to study the nonlinear pulse propagation in waveguides. It assumes that the nonlinear polarization induced when a light pulse propagates breaks the translational symmetry along the propagation direction by changing the constant of motion (eigenvalue) related to this symmetry, while the electromagnetic field along the transverse plane is still well-described by means of the unperturbed solutions (eigenmodes). Furthermore, it allows to study the pulse propagation in two steps. In fact, this work provides tools to deal separately with these steps. On the other hand, Fig. 1.1 compares direct design procedures that always connect the pulse propagation study to an specific waveguide cross-section, with the inverse design. The starting point of design tasks is usually the material distribution according to the cross-section geometry. This information is contained in the permittivity distribution, $\varepsilon(\mathbf{x}_t, \omega)$, that corresponds to the input to compute the waveguide physical properties from Maxwell's equations. These features describe the waveguide within the context of the pulse propagation or, in other words, they are the input for the equation governing the pulse evolution. The output pulse is calculated by solving the propagation equation. This method is the direct design. However, the above starting point will be the ending point in the inverse design. Our approach can be formulated in two stages (see Fig. 1.1). At the inverse nonlinear design step, the problem could be stated as *what are the waveguide physical properties that produce a particular nonlinear behavior?* For example, we could discuss about the dispersion needed to optimize

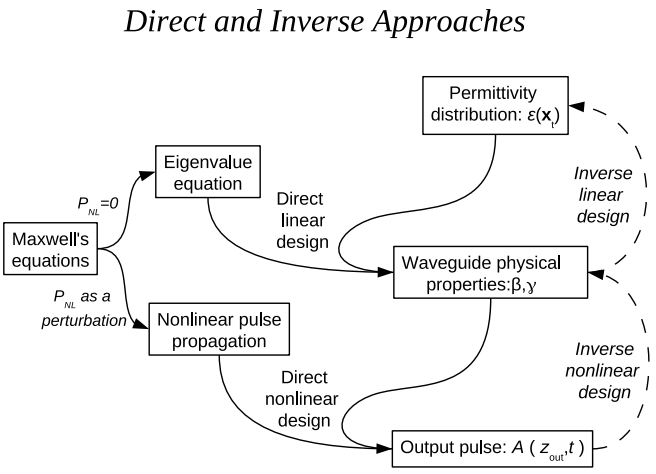

Figure 1.1: Comparison between standard procedures, namely, direct design strategies, and the inverse design. In the figure, β stands for the propagation constant, and γ is the nonlinear coefficient of the waveguide. Note that the waveguide is defined by means of the permittivity distribution, ε, within the eigenvalue equation, and through β and γ, that are defined as the waveguides physical properties, within the nonlinear pulse propagation equation. The dashed arrows indicates our objective.

the spectral broadening of a pulse. The answer to this question would provide the target features of our inverse linear design step. So, at this second step, we should address *what is the geometry that generate the properties that are the solution of the nonlinear step?* If we were able to respond successfully to both questions, we would find how to design a waveguide to obtain an output pulse with the desired properties. Therefore, the main objectives of this thesis are:

- The development of an analytical strategy to study nonlinear pulse propagation with arbitrary dispersion curves (Papers II and V).
- The implementation of a program to calculate alterations of the dispersion curve of high-index-contrast waveguides due to geometrical changes (Paper IV).

- The application of these tools to generate SC spectra in silicon waveguides (Papers I and V).

I will complete this introductory overview with three more technical chapters. The Chapter 2 will be devoted to basic notions around the main nonlinear processes studied in this work. These mechanisms will be studied through an approximate time-frequency analysis based on the instantaneous frequency. Although it constitutes a simplified picture of the pulse evolution, it results a very useful tool to obtain a significant physical insight around the intricate interplay between dispersion and nonlinearities. In Chapter 3, I will revisit the derivation of the GNLSE from first principles, avoiding standard (but unnecessary) approximations, hence paving the way for future work. In Chapter 4, I will raise some numerical issues regarding the numerical study of high-index-contrast waveguides that have been considered when tackling SOI waveguides. The appended papers are summarized in Chapter 5. Finally, the conclusions are presented in Chapter 6.

Chapter 2

Physical processes governing nonlinear pulse propagation

The study of light propagation in material media always requires molding the macroscopic response of the matter. In our case, this information is provided by the dielectric function or permittivity of the materials. For the purposes of this chapter, vectorial considerations will be omitted, so the permittivity will be directly related to the refractive index. From a macroscopic perspective, all the physical processes that affect light propagation appear as different functional dependences of the refractive index. Furthermore, losses can also be included by considering an imaginary part of the refractive index. It can be understood based on classical models of the polarizability, where losses are analyzed through a restoring force, that produces a complex refractive index [12]. This work is mainly focused on the frequency dependence of the refractive index, namely, the group-velocity dispersion (GVD), and the intensity dependence of its real part, namely, the Kerr effect or self-phase modulation (SPM), and its imaginary part, produced by the so-called two-photon absorption (TPA). In addition, this process generates free carriers that produce losses, namely, free-carrier absorption (FCA), and also alter the refractive index, namely, free-carrier dispersion (FCD). It means that we will only consider materials where third-order nonlinearities dominate. Second-order nonlinear materials are out of the scope of this work.

GVD and SPM are usually understood in standard textbooks by way of

their effects on the light signal [13,14]. Let us consider a light signal described in the time domain by $A(t) = |A(t)| \exp[i\varphi(t)]$, where $|A(t)|$ indicates the instantaneous amplitude and $\varphi(t)$ is the instantaneous phase. Analogously, this signal can be represented in the spectral domain by $\tilde{A}(\omega) = |\tilde{A}(\omega)| \exp[i\phi(\omega)]$, where $|\tilde{A}(\omega)|$ stands for the spectral amplitude and $\phi(\omega)$ corresponds to the spectral phase. Since the GVD only produces changes on ϕ, it translates into distortions on $|A|$, *e.g.*, temporal pulse broadening, and also on φ. Similarly, SPM modifies φ, keeping $|A|$ unaltered. Consequently, both $|\tilde{A}|$ and ϕ change, inducing spectral broadening. Although this description allows to take advantage of both processes, it does not explain these phenomena in physical terms. In addition, it cannot provide complete information about their interplay. The lack of time-frequency analysis providing analytical solutions to this problem becomes an insurmountable obstacle. However, significant physical insight can be obtained by considering the instantaneous frequency of the pulse. Roughly speaking, it constitutes the most basic time-frequency tool. Although it needs some assumptions to be applied and its relation with Fourier frequencies is not direct [15–17], it allows to acquire physical intuition about some features of the pulse propagation. Due to its importance in this work, its meaning will be drawn in the following lines.

From the Fourier theory, usual time signals can be understood as a coherent superposition of monochromatic waves, $A(t) = \sum_k a_k \exp(-i\omega_k t)$, where a_k are complex coefficients. In other words, the instantaneous power of a signal results from a sum of amplitudes of waves with different frequencies. Nevertheless, the main contribution to $A(t)$ at each temporal instant can come from *one* of these waves. In such a case, the frequency of that wave can thus be associated to the instant where it dominates. Consequently, a time distribution of frequencies can be constructed from a signal [18]. Following the above notation, the Fourier transform of a signal can be written in the following way:

$$\begin{aligned}\tilde{A}(\omega) = \int_{-\infty}^{\infty} A(t) e^{i\omega t} \mathrm{d}t &\approx \sum_k \int_{\tau_k}^{\tau_{k+1}} |A(\tau_k)| e^{i\varphi(\tau_k)} e^{i\partial_t\varphi(\tau_k)(t-\tau_k)} e^{i\omega t} \mathrm{d}t \\ &= \sum_k |A(\tau_k)| e^{i\varphi(\tau_k)} e^{-i\partial_t\varphi(\tau_k)\tau_k} \int_{\tau_k}^{\tau_{k+1}} e^{i(\partial_t\varphi(\tau_k)+\omega)t} \mathrm{d}t, \quad (2.1)\end{aligned}$$

where it is assumed that the temporal variations of the instantaneous power are slow compared to those of the instantaneous phase. Based on the stationary phase method [12], the temporal intervals, labelled by τ_k, where $-\partial_t\varphi(\tau_k) = \omega$ will mainly contribute to $\tilde{A}(\omega)$. Within these intervals, *i.e.*, locally, $A(t)$ behaves like a monochromatic wave with frequency $-\partial_t\varphi(\tau_k)$, that corresponds

to the chirp of the pulse. Although the chirp fails as an approximate picture of the temporal distribution of frequencies when the pulse experiences strong temporal changes, it remains valid where only nonlinearities act because they do not modify the temporal pulse profile.

It is now interesting to review SPM and GVD from the point of view of the instantaneous frequency. Firstly, the time distribution of frequencies can change along the propagation due to the different group velocity of these (quasi-monochromatic) waves. This effect does not inherently involve any interaction between the waves. Nonetheless, their interaction induced by *other* processes will be affected by this feature. In this way, temporal changes induced by the GVD can be interpreted in a more natural way. Secondly, based on its own definition, the growth of the chirp produced during the pulse propagation directly implies spectral broadening. So, SPM can be also partially described by using the instantaneous frequency of the pulse. Even the spectral oscillations related to SPM can be justified because each instantaneous frequency possesses two different temporal contributions coherently superposed when the spectrum is calculated [19].

As we will see in the next chapter, an intensity dependent refractive index is caused by a third-order susceptibility, χ^3. A fundamental interaction controlled by this susceptibility is the so-called four wave-mixing (FWM). It corresponds to $\omega_{p,1} + \omega_{p,2} \rightarrow \omega_s + \omega_i$, where $\omega_{p,1}$ and $\omega_{p,2}$ indicate the pump waves whose interaction produces a signal, ω_s, and idler, ω_i, waves. In these processes, $\omega_{p,1} + \omega_{p,2} = \omega_s + \omega_i$, that refers to the energy conservation. Note that this process also preserves the number of photons. If only one pump wave is actually acting, the process is called degenerate FWM, being non degenerate if two different pump waves interact. When this process is studied considering the electric field as a sum of four (strictly) monochromatic waves, concepts as phase matching or gain (related to the momentum conservation of the above process) of new generated monochromatic waves appear [14,20]. Nevertheless, these concepts do not appear when the pulse spectral broadening induced by SPM is studied. Clearly, the analysis of SPM in terms of multiple FWM would be cumbersome and probably less useful than the study of the pulse envelope evolution. However, it does not mean that SPM and, in general, nonlinear pulse propagation could be essentially different to FWM among several locally monochromatic waves moving at different velocities [21, 22].

After these general considerations, we restrict our attention to highly nonlinear systems under normal dispersion regime. It refers to a pulse propagation initially dominated by SPM where red-shifted frequencies (negative chirps) travel faster and blue-shifted frequencies (positive chirps) move slower than those frequencies around the carrier (nearly zero chirps). We consider $\gamma > 0$,

which corresponds to the self-focusing Kerr effect [14]. Due to the intensity-dependent refractive index, the chirp induced by SPM while it dominates goes as $-\gamma\partial_t P\, z$, where P is the instantaneous power of the pulse that propagates along the z-coordinate, see Fig. 2.1 (it can be easily checked from GNLSE, that is derived Chapter 2). Therefore, red-shifted frequencies are located at the leading pulse edge and blue-shifted frequencies at the trailing edge. Since the inverse of the (group) velocity of quasi-monochromatic waves is given by $\beta_1(\omega) = \mathrm{d}\beta/\mathrm{d}\omega$ [12], this regime takes place when $\beta_1(\omega > \omega_0) > \beta_1(\omega_0) > \beta_1(\omega < \omega_0)$. This fact implies $\beta_2 = \mathrm{d}\beta^2/\mathrm{d}\omega^2|_{\omega_0} > 0$ (consider that ω belongs to a neighborhood of ω_0).

Under normal dispersion conditions, a strong temporal overlapping among locally quasi-monochromatic waves (according to the instantaneous frequency definition) located at the pulse tails could be produced. If so, the nonlinear interactions of these waves will be reinforced, giving rise to new frequency generation, see Fig. 2.1. From a temporal picture, this phenomenon leads to strong oscillations at the pulse tails (where the interaction is produced), corresponding to the effect called optical wave-breaking (OWB) [23–25]. It constitutes a clear example where the interplay between nonlinearities and dispersion cannot be avoided. Some theoretical research was done regarding the distance where the process takes place [26] or input profiles avoiding such an effect [27]. Even assuming constant GVD, these works show the difficulties that arise when complete information about the pulse is sought. New interesting applications of OWB related to coherent SC generation [28, 29] and pulse compression [30] have been recently pointed out. Nevertheless, the available theoretical tools remain the same. Particularly, there is a lack of studies of OWB under nonconstant GVD. One of the main results of this dissertation is the derivation of analytical expressions to describe the spectral broadening induced by OWB under higher-order dispersion.

Most of the work around SC generation exploits soliton-related dynamics [6]. A soliton is a kind of pulse that propagates without being distorted (or that suffers periodic changes) due to a compensation between an anomalous GVD, *i.e.*, $\beta_2 < 0$, and SPM effects [13]. The spectral broadening arises, in different stages, from SPM reinforced by temporal compression, higher-order soliton fission [31] and dispersive waves emitted by solitons perturbed by higher-order dispersion [32–34] or affected by Raman induced soliton self-frequency shift [35]. Since it requires pumping at the anomalous dispersion regime, input noise can be amplified through the degenerate FWM process associated to the so-called modulation instability (MI). If this mechanism dominates, SC generation becomes highly sensitive to input pulse fluctuations and thus, unstable. Consequently, shorter pulses must be propagated in order to

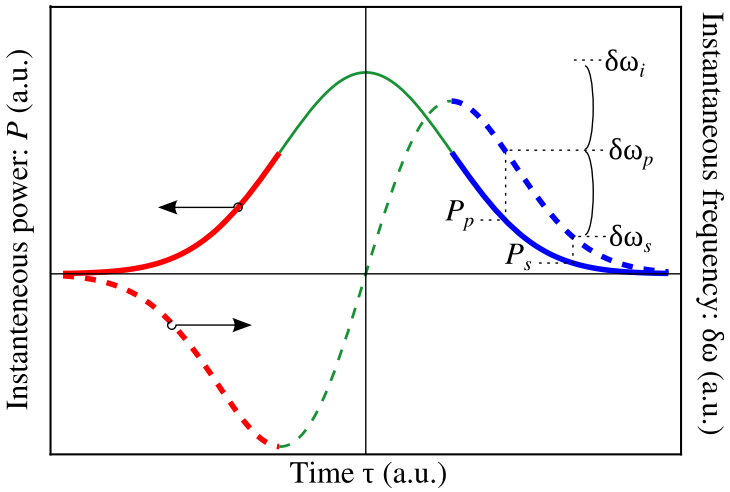

Figure 2.1: Instantaneous frequency, $\delta\omega$, and intensity profile, P, of a pulse affected only by SPM. Note that red-shifted frequencies (red curve) are located at the leading pulse edge ($\tau < 0$) and blue-shifted frequencies (blue curve) and the trailing edge ($\tau > 0$). Subindex p, s, and i indicate pump, signal and idler, respectively.

SPM-induced new frequencies overlap with those amplified by MI. In this way, the noise background has a minor impact [6]. With the aim of avoiding this undesirable effect without any additional bound, we choose to investigate SC generation pumping at the normal dispersion regime, where MI does not takes place [6, 13]. Clearly, enhancing the spectral broadening at this dispersion regime is actually the challenge here. Our goal is to make really efficient the new frequency production by OWB.

TPA is one of the main limiting factor for continuum generation in silicon waveguides [36, 37]. Similarly to SPM, this process manifests as an intensity dependence of the imaginary part of the refractive index (as it has been mentioned, it takes into account losses). This feature leads to a different impact of TPA along a pulse. This point will be studied in Paper I. Although it is a χ^3 process, the fundamental interaction differs from FWM because it is not a parametric process. In this case, electrons in the valence band absorb two photons that induce, assisted by phonons [38, 39], a transition to the conduction band. It generates free carriers that induce additional nonlinear losses,

namely, free-carrier absorption (FCA) and changes on the refractive index, namely, free-carriers dispersion (FCD) [36]. The effects of these processes on pulse propagation will be also studied in Paper I. Mechanisms of decay of these free-carriers will not be studied here. Both SPM and TPA are related to electronic response of media, taking place in a nearly instantaneous way [38]. Processes related to the nuclei response of media, such as Raman or Brillouin effects are out of the scope of this work. Brillouin scattering turns out negligible in silicon [38] and Raman response in silicon is about 3 ps [38], so it can be neglected at the short pulse regime (~ 0.1 ps) [40, 41].

All of the above interactions will be studied within the Maxwell's equations framework by means of GNSLE. At this point, we only need to indicate that the nonlinear polarization (including all the above processes) is actually weak enough to be considered as a perturbation. As other perturbative approaches, the information derived from the unperturbed problem will be a key element. In our case, it refers to some properties of the propagation constant, β, and the nonlinear coefficient, γ, which correspond to the previously referred waveguide physical properties (see Fig. 1.1). Indeed, these functions govern the nonlinear pulse behavior. Both functions have a material and a geometric contributions, being the last one particularly important for SOI waveguides.

We address this task through an inverse approach. So, in a first step, our aim will be determine β and γ leading to a specific nonlinear propagation to accomplish an application. Here we are interested on SC generation based on OWB in SOI waveguides. It corresponds to our inverse nonlinear design. Once these functions are found, our second goal will be to achieve the geometric parameters so that β and γ match the targets obtained in our inverse nonlinear design. It corresponds to our inverse linear design.

In spite of γ being a waveguide property (*i.e.*, it does not depend on the pulse intensity), it depends on the assumptions made in the derivation of the pulse propagation equation. Therefore, I consider a complete derivation of this equation is required here. It will be done in the next chapter, as well as the construction of the nonlinear polarization. Both mathematical developments will be developed with care, avoiding unnecessary initial approximations to point out their physical meaning.

Chapter 3

Nonlinear pulse propagation equation

Our goal in this thesis is to generate SC based on OWB. We use silicon waveguides because they allow to engineer the dispersion and offer high nonlinearities. Fine control of dispersion usually demands inhomogeneous cross-sections. In addition, they must be considered full vectorial systems due to its high index contrast (we will deal with this feature in the next chapter). For our purposes, it is useful to classify the pulse propagation methods according to the treatment of backward components and transverse effects. This work will keep within the unidirectional pulse propagation approximation due to the backward wave can be often neglected in nonlinear optical materials, even at intensities near the damage threshold [42]. Mathematically, if the nonlinear polarization is a perturbation, it is done by applying the so-called slowly-varying envelope approximation (SVEA) [43]. This requirement will be properly defined at the end of this section. Nevertheless, some new methods have been proposed to describe the effects related to the backward propagating wave. On the one hand, the second-order wave equation can be formally solved by means of a modal approach, to deal with transverse effects, and the Green function, to decompose the spectrum into its forward and backward components [44]. On the other hand, the electric and magnetic field can be combined to reformulate Maxwell's equations in terms of new variables representing energy flows in the forward and backward directions [45].

Transverse effects will be studied here through a modal method that leads to a $1 + 1$ dimensions equation. Other approaches based on $3 + 1$ dimen-

sions were derived for homogeneous media [46, 47] and therefore, will not be considered here. In addition, our starting point will be Maxwell's equations (not the second order-wave equation [48]). In this sense, our derivation will be close to other previous works where the *conjugated* form of the reciprocity theorem [49] was applied [50–53]. Although these works study unidirectional pulse propagation, the perturbative treatment of the nonlinear polarization and hence, the SVEA, is not explicitly shown [54]. Moreover, a similar derivation based on the *unconjugated* form of the reciprocity theorem could give rise to a different propagation equation if the longitudinal component of the nonlinear polarization were not neglected. These ambiguous facts are clarified following our approach.

Lastly, the nonlinear polarization will be constructed without any restriction about the bandwidth of the pulse, avoiding standard approximations regarding the coupling between negative and positive Fourier frequencies [55]. New phenomena has been recently observed [56] and interpreted based on these considerations [57]. Furthermore, I will also do some remarks about the dispersion of nonlinearities, which is also being a topic of recent research [58–60] and cannot be completely neglected for the waveguides that we will use in our work. I want to emphasize that the main aim of the following procedure is to clarify the range of applicability of the GNLSE and therefore, of the numerical results included in Papers II and V. Throughout the derivation, I will highlight all the hypothesis and their physical consequences. In addition, this development also allows to evaluate the effort that would be required to include new phenomena in the theory.

3.1 Pulse propagation equation for a generic nonlinear polarization

Let us consider Maxwell's equations in presence of a nonlinear polarization in a region with no charges and no currents [50, 52, 58]

$$\nabla \cdot (\varepsilon_0 \varepsilon \tilde{\mathbf{E}}) = -\nabla \cdot \tilde{\mathbf{P}}_{\mathrm{NL}}, \tag{3.1}$$

$$\nabla \cdot \tilde{\mathbf{H}} = 0, \tag{3.2}$$

$$\nabla \times \tilde{\mathbf{H}} = -i\omega\varepsilon_0 \varepsilon \tilde{\mathbf{E}} - i\omega \tilde{\mathbf{P}}_{\mathrm{NL}}, \tag{3.3}$$

$$\nabla \times \tilde{\mathbf{E}} = i\omega\mu_0 \tilde{\mathbf{H}}, \tag{3.4}$$

where $\tilde{\mathbf{E}} = \mathfrak{F}(\mathbf{E}) = \int_{-\infty}^{\infty} \mathbf{E} \exp(i\omega t) \mathrm{d}t$ is the Fourier transform of the electric field, $\mathbf{E}$, $\mathbf{H}$ stands for the magnetic field, $\varepsilon = \varepsilon(\mathbf{x}_t, \omega)$ is the dielectric tensor of an invariant system along the z-coordinate (note that it only depends

on the transverse coordinates, $\mathbf{x}_t$, and it does not include nonlinear effects, that are described by means of a nonlinear polarization, $\tilde{\mathbf{P}}_{\mathrm{NL}}$), ε_0 and μ_0 represent the permittivity and permeability of the vacuum, respectively. In a modal approach, the fields are described by means of an expansion of the corresponding waveguide modes. Consequently, the components of this linear superposition of modes do not depend on $\mathbf{x}_t$, or equivalently, they are a function of z and ω. Our study restricts this expansion to one mode, although the following procedure would enable to include multimode effects [48, 61]. Therefore, we assume single-mode propagation and introduce the next double ansatz $\tilde{\mathbf{E}} = \tilde{B}_e(z,\omega)\mathbf{e}(\mathbf{x}_t,\omega)\exp(i\beta z)$ and $\tilde{\mathbf{H}} = \tilde{B}_h(z,\omega)\mathbf{h}(\mathbf{x}_t,\omega)\exp(i\beta z)$. In this ansatz, $\mathbf{e}$ and $\mathbf{h}$ correspond to the electric and magnetic fields of a waveguide mode (we have included in Appendix A a complete derivation of the equations satisfied by these modes and some of their properties) normalized such that Eq. (A.21) is satisfied, *i.e.*, are solutions of Eqs. (3.3) and (3.4) when $\tilde{\mathbf{P}}_{\mathrm{NL}} = 0$. $\tilde{B}_{e,h}$ can still be considered the components of this monomode expansion. Note that the electric and magnetic field do not share the same envelope, which is the key difference with respect to [50–54]. Furthermore, we have not evaluated the mode at any carrier frequency [52]. Consequently, this ansatz does not imply other assumptions besides the single-mode condition. It is worth noticing that the single-mode condition already implies some restrictions on $\tilde{B}_{e,h}$ due to Eqs. (3.1) and (3.2). Particularly, $|\partial_z \tilde{B}_h| \ll |\beta \tilde{B}_h|$. We will return to this condition at the end of this section. If we introduce this ansatz into Eqs. (3.3) and (3.4), we derive the following two coupled equations

$$\begin{aligned}\nabla \times \tilde{\mathbf{H}} &= \tilde{B}_h \nabla \times \left(\mathbf{h}\, e^{i\beta z}\right) + e^{i\beta z}\hat{\mathbf{z}} \times \mathbf{h}\, \partial_z \tilde{B}_h \\ &= e^{i\beta z}\left(-i\omega\varepsilon_0\varepsilon\, \mathbf{e}\tilde{B}_h + \hat{\mathbf{z}} \times \mathbf{h}\, \partial_z \tilde{B}_h\right) = -e^{i\beta z} i\omega\varepsilon_0\varepsilon\, \mathbf{e}\tilde{B}_e - i\omega\tilde{\mathbf{P}}_{\mathrm{NL}}, \quad (3.5)\end{aligned}$$

$$\begin{aligned}\nabla \times \tilde{\mathbf{E}} &= \tilde{B}_e \nabla \times \left(\mathbf{e}\, e^{i\beta z}\right) + e^{i\beta z}\hat{\mathbf{z}} \times \mathbf{e}\, \partial_z \tilde{B}_e \\ &= e^{i\beta z}\left(i\omega\mu_0 \mathbf{h}\tilde{B}_e + \hat{\mathbf{z}} \times \mathbf{e}\, \partial_z \tilde{B}_e\right) = e^{i\beta z} i\omega\mu_0 \mathbf{h}\tilde{B}_h, \quad (3.6)\end{aligned}$$

where we have taken into account both $\mathbf{h}$ and $\mathbf{e}$ are the mode fields. The above equations can be rearranged as follows:

$$\begin{aligned}\hat{\mathbf{z}} \times \mathbf{h}\, \partial_z \tilde{B}_h + i\omega\varepsilon_0\varepsilon\, \mathbf{e}(\tilde{B}_e - \tilde{B}_h) &= -i\omega\tilde{\mathbf{P}}_{\mathrm{NL}} e^{-i\beta z}, \quad (3.7)\\ \hat{\mathbf{z}} \times \mathbf{e}\, \partial_z \tilde{B}_e + i\omega\mu_0 \mathbf{h}(\tilde{B}_e - \tilde{B}_h) &= 0. \quad (3.8)\end{aligned}$$

Now we scalar-multiply Eq. (3.7) by $\mathbf{e}^*$ and Eq. (3.8) by $\mathbf{h}^*$ and integrate them over $\mathcal{S}$, the two-dimensional domain where the fields are defined,

$$-\partial_z \tilde{B}_h \int_{\mathcal{S}} (\mathbf{e}^* \times \mathbf{h}) \cdot \hat{\mathbf{z}} \, \mathrm{d}S + i\omega(\tilde{B}_e - \tilde{B}_h)\varepsilon_0 \int_{\mathcal{S}} \mathbf{e}^* \cdot \varepsilon \mathbf{e} \, \mathrm{d}S = -i\omega \int_{\mathcal{S}} \mathbf{e}^* \cdot \tilde{\mathbf{P}}_{\mathrm{NL}} \, \mathrm{d}S \, e^{-i\beta z}, \tag{3.9}$$

$$\partial_z \tilde{B}_e \int_{\mathcal{S}} (\mathbf{e} \times \mathbf{h}^*) \cdot \hat{\mathbf{z}} \, \mathrm{d}S + i\omega(\tilde{B}_e - \tilde{B}_h)\mu_0 \int_{\mathcal{S}} \mathbf{h}^* \cdot \mathbf{h} \, \mathrm{d}S = 0. \tag{3.10}$$

where we have used the vectorial identity $\mathbf{a} \cdot (\mathbf{b} \times \mathbf{c}) = -\mathbf{b} \cdot (\mathbf{a} \times \mathbf{c})$. It is worthwhile to note $(\mathbf{e}^* \times \mathbf{h}) \cdot \hat{\mathbf{z}} = (\mathbf{e}_t^* \times \mathbf{h}_t) \cdot \hat{\mathbf{z}}$. Since it is always possible for nonabsorbing waveguides to choose the transverse components, $\mathbf{e}_t$ and $\mathbf{h}_t$ (that can be understood as three dimensional vectors with a zero longitudinal component), pure real and the longitudinal, e_z and h_z, pure imaginary [49], we can omit the complex conjugate on $\mathbf{e}_t^*$ and $\mathbf{h}_t^*$. In this way, we can take advantage of the biorthogonality relation expressed by Eq. (A.21) and set the coefficients of both $\partial_z \tilde{B}_h$ in Eq. (3.9) and $\partial_z \tilde{B}_e$ in Eq. (3.10) to 1. Clearly, this result would also be obtained if we had scalar-multiplied Eq. (3.7) by $\mathbf{e}$ and Eq. (3.8) by $\mathbf{h}$. Nevertheless, the nonlinear term (and therefore, the pulse propagation equation) could change if the longitudinal component of the nonlinear polarization would not be neglected. Note that this question would appear if the same envelope were considered for both the electric and magnetic mode fields. Keeping two different envelopes, this question does not arise. According to Eq. (A.24), it is convenient to scalar-multiply by the complex conjugates because it gives rise to the same coupling coefficients of the left-hand side of the above equations. Consequently, we can subtract both equation to obtain

$$\partial_z(\tilde{B}_h + \tilde{B}_e) = i\omega e^{-i\beta z} \int_{\mathcal{S}} \mathbf{e}^* \cdot \tilde{\mathbf{P}}_{\mathrm{NL}} \, \mathrm{d}S. \tag{3.11}$$

Some points around this equation must be emphasized. It appears in a natural way as the constraint imposed by Maxwell's equations on $\tilde{B}_h$ and $\tilde{B}_e$ under single-mode propagation assumption. If $\tilde{B}_h \approx \tilde{B}_e \equiv \tilde{B}$ is assumed, it is obtained the nonlinear pulse propagation equation [50]:

$$\partial_z \tilde{B} = \frac{i}{2} \omega e^{-i\beta z} \int_{\mathcal{S}} \mathbf{e}^* \cdot \tilde{\mathbf{P}}_{\mathrm{NL}} \mathrm{d}S. \tag{3.12}$$

On the one hand, we point out that the above approximation actually corresponds to the commonly used SVEA. If Eq. (3.4) is developed under the above

assumption,

$$\nabla_{\mathrm{t}} \times \mathbf{e} + \hat{z} \times \mathbf{e} \left(\beta \tilde{B} + \partial_z \tilde{B} \right) = i\omega\mu_0 \mathbf{h}, \tag{3.13}$$

which means that this ansatz describes a physical solution as long as $|\partial_z \tilde{B}| \ll |\beta \tilde{B}|$. It implies that the nonlinear polarization [which controls $\partial_z \tilde{B}$, see Eq. (3.12)] must be treated as a perturbation. It corresponds to the SVEA [38] and allows to neglect the backward wave [42, 43]. So, this approach suggests that SVEA could also be related to differences between the electric and magnetic envelopes. We remind that the single-mode propagates can also exist under this approximation, as we stated at the beginning of this section. It points out that several physical effects are related to SVEA. We leave the study of the impact of each effect for future research.

3.2 Third-order nonlinear polarization

The use of Eq. (3.12) to evaluate the propagation of a light pulse throughout a waveguide requires to develop $\tilde{\mathbf{P}}_{\mathrm{NL}}$ in terms of the field envelopes. Firstly, a generic third-order nonlinear polarization is written following the conventions of [20] (except for the irrelevant fact regarding the convention of the sign of the first frequency argument). The next expression

$$P_i^{(3)}(t) = \epsilon_0 \int_{-\infty}^{\infty} R_{ijkl}^{(3)}(\boldsymbol{\tau}) E_j(t-\tau_1) E_k(t-\tau_2) E_l(t-\tau_3)\, \mathrm{d}^3\boldsymbol{\tau}, \tag{3.14}$$

corresponding to a generic form of a third-order polarization (note it is assumed a local spatial response), where $\boldsymbol{\tau} = (\tau_1, \tau_2, \tau_3)$ and $\mathrm{d}^3\boldsymbol{\tau} = \mathrm{d}\tau_1 \mathrm{d}\tau_2 \mathrm{d}\tau_3$. The tensor $R_{ijkl}^{(3)}$ is called the response function of the medium. It must be real due to $\mathbf{E}(t)$ is a real-valued field. Moreover, it must also vanish when $\tau_i < 0$ to ensure the causality condition [20]. It can be rewritten in the frequency domain as

$$\begin{aligned} \tilde{P}_i^{(3)}(\omega) = {} & \epsilon_0 (2\pi)^{-2} \\ & \times \int_{-\infty}^{\infty} \chi_{ijkl}^{(3)}(\omega_\sigma; \boldsymbol{\omega}) \tilde{E}_j(\omega_1) \tilde{E}_k(\omega_2) \tilde{E}_l(\omega_3) \delta(\omega - \omega_\sigma)\, \mathrm{d}^3\boldsymbol{\omega}, \end{aligned} \tag{3.15}$$

where $\chi_{ijkl}^{(3)}(\omega_\sigma; \boldsymbol{\omega}) = \int_{-\infty}^{\infty} R_{ijkl}^{(3)}(\boldsymbol{\tau}) \exp(i\,\boldsymbol{\omega} \cdot \boldsymbol{\tau})\, \mathrm{d}^3\,\boldsymbol{\tau}$ is the third-order susceptibility, $\boldsymbol{\omega} = (\omega_1, \omega_2, \omega_3)$, $\mathrm{d}^3\boldsymbol{\omega} = \mathrm{d}\omega_1 \mathrm{d}\omega_2 \mathrm{d}\omega_3$, $\omega_\sigma = \omega_1 + \omega_2 + \omega_3$, *i.e.*, ω_σ labels the sum of the three (last) arguments of the third-order susceptibility, and $\int_{-\infty}^{\infty} \mathrm{d}t \exp(i\omega t) = 2\pi\delta(t)$ has been used.

With the aim of removing the redundant information contained in the negative Fourier frequencies of a real-valued signal, as the electric field, it is interesting to introduce at this point the so-called analytic signal, $\tilde{\mathcal{E}}_i$, for the electric field, following [54, 62]:

$$\tilde{\mathcal{E}}_i(\omega) = \begin{cases} 0 & \text{if } \omega < 0, \\ \tilde{E}_i(\omega) & \text{if } \omega = 0, \\ 2\tilde{E}_i(\omega) & \text{if } \omega > 0, \end{cases} \tag{3.16}$$

that implies $2\tilde{E}_i(\omega) = \tilde{\mathcal{E}}_i(\omega) + \tilde{\mathcal{E}}_i^{\,*}(-\omega)$. In addition, $\tilde{\mathcal{E}}_i(\omega)$ can be interpreted as a physical wave with a physical frequency suggesting, in this way, the fundamental processes behind the different terms of the third-order polarization.

Attending to the intrinsic permutation symmetry, $\chi^{(3)}_{ijkl}(\omega_\sigma;\boldsymbol{\omega})$ is invariant under the interchange of pairs (m,ω_n), being $m = j,k,l$ and $n = 1,2,3$, the reality condition, $[\chi^{(3)}_{ijkl}(\omega_\sigma;\boldsymbol{\omega})]^* = \chi^{(3)}_{ijkl}(\omega_\sigma;-\boldsymbol{\omega})$ [20], and $\delta(\omega) = \delta(-\omega)$, Eq. (3.15) can be rewritten after some algebra as

$$\tilde{\mathbf{P}}^{(3)}(\omega) = \frac{1}{2}\left[\tilde{\mathbf{P}}_{\mathrm{TSFG}}(\omega) + \tilde{\mathbf{P}}_{\mathrm{FWM}}(\omega) + \tilde{\mathbf{P}}^*_{\mathrm{TSFG}}(-\omega) + \tilde{\mathbf{P}}^*_{\mathrm{FWM}}(-\omega)\right]. \tag{3.17}$$

Here the following functions have been introduced,

$$\tilde{P}_{\mathrm{TSFG},i}(\omega) = \epsilon_0(2\pi)^{-2}2^{-2} \times \int_{-\infty}^{\infty} \chi^{(3)}_{ijkl}(\omega_\sigma;\omega_1,\omega_2,\omega_3)\tilde{\mathcal{E}}_j(\omega_1)\tilde{\mathcal{E}}_l(\omega_2)\tilde{\mathcal{E}}_k(\omega_3)\delta(\omega-\omega_\sigma)\,\mathrm{d}^3\boldsymbol{\omega}, \tag{3.18}$$

$$\tilde{P}_{\mathrm{FWM},i}(\omega) = \epsilon_0(2\pi)^{-2}2^{-2}3 \times \int_{-\infty}^{\infty} \chi^{(3)}_{ijkl}(\omega_\sigma;\omega_1,-\omega_2,\omega_3)\tilde{\mathcal{E}}_j(\omega_1)\tilde{\mathcal{E}}^*_k(\omega_2)\tilde{\mathcal{E}}_l(\omega_3)\delta(\omega-\omega_\sigma)\,\mathrm{d}^3\boldsymbol{\omega}. \tag{3.19}$$

Now I want to emphasize two points around these functions. On the one hand, there is no contribution of the electric field for negative negative frequencies due to $\tilde{\mathcal{E}}_i(\omega < 0) = 0$. On the other hand, it is worth to emphasize that the analytic signal of $\tilde{\mathbf{P}}^{(3)}(\omega)$ is *not* $\tilde{\mathbf{P}}_{\mathrm{TSFG}}(\omega) + \tilde{\mathbf{P}}_{\mathrm{FWM}}(\omega)$ because $\tilde{\mathbf{P}}^*_{\mathrm{FWM}}(-\omega)$ can be nonzero when $\omega > 0$. This fact suggests that $\tilde{\mathbf{P}}^*_{\mathrm{FWM}}(-\omega)$ does not contain the same information of $\tilde{\mathbf{P}}_{\mathrm{FWM}}(\omega)$, unlike $\tilde{\mathbf{P}}_{\mathrm{TSFG}}(\omega)$ and $\tilde{\mathbf{P}}^*_{\mathrm{TSFG}}(-\omega)$.

Based on energy conservation (shown explicitly in the above equations), each of those polarizations terms could describe the following physical processes:

$$\tilde{\mathbf{P}}_{\mathrm{TSFG}}(\omega) : \omega_1 + \omega_2 + \omega_3 \rightarrow \omega, \tag{3.20}$$

$$\tilde{\mathbf{P}}_{\mathrm{FWM}}(\omega) : \omega_1 + \omega_3 \rightarrow \omega_2 + \omega, \tag{3.21}$$

$$\tilde{\mathbf{P}}^{*}_{\mathrm{FWM}}(-\omega) : \omega_2 \rightarrow \omega_1 + \omega_3 + \omega. \tag{3.22}$$

In this work we will only focus on $\tilde{\mathbf{P}}_{\mathrm{FWM}}(\omega)$, which actually describes the four wave mixing process [14, 20]. However, I want to point out that $\tilde{\mathbf{P}}_{\mathrm{TSFG}}(\omega)$ seems to be related to the *third order sum-frequency generation* (TSFG) [63] and hence, in such a case it would include the *third harmonic generation* (THG) process for the degenerate case $\omega_1 = \omega_2 = \omega_3$ [13]. Moreover, the above scheme would indicate that $\tilde{\mathbf{P}}^{*}_{\mathrm{FWM}}(-\omega)$ does not represent any four wave mixing process. It could be related to the recently observed *negative resonant radiation* according to [56, 57]. However, both processes are out of the scope of this thesis and will be addressed in future work.

3.3 Generalized nonlinear Schrödinger equation

In this section, Eqs. (3.12) and (3.19) will be developed in order to derive a suitable propagation equation. Based on the previous reasoning, $\tilde{\mathcal{E}}(\mathbf{x}, \omega) = 2\tilde{B}(z, \omega)\mathbf{e}(\mathbf{x}_t, \omega)\exp(i\beta(\omega)z)$ and Eq. (3.12) can now be written as

$$\begin{aligned} e^{i\beta(\omega)z}\partial_z \tilde{B}(z,\omega) = i(2\pi)^{-2} \int_{-\infty}^{\infty} \delta(\omega - \omega_\sigma)\, \gamma(\omega, \boldsymbol{\omega}) \\ \times \tilde{B}(z,\omega_1) e^{i\beta(\omega_1)z} \tilde{B}^{*}(z,\omega_2) e^{-i\beta(\omega_2)z} \tilde{B}(z,\omega_3) e^{i\beta(\omega_3)z} \mathrm{d}^3\boldsymbol{\omega} \end{aligned} \tag{3.23}$$

where $\omega > 0$, $\omega_\sigma = \omega_1 - \omega_2 + \omega_3$ and it is defined

$$\gamma(\omega, \boldsymbol{\omega}) = \frac{3}{8}\omega\epsilon_0 \int_S \chi^{(3)}_{ijkl}(\omega; \omega_1, -\omega_2, \omega_3) e^{*}_i(\omega) e_j(\omega_1) e^{*}_k(\omega_2) e_l(\omega_3)\, \mathrm{d}S. \tag{3.24}$$

As it will be apparent at the end of this section, it is now convenient to define a new envelope $\tilde{A}(z, \omega) = \tilde{B}(z, \omega)\exp[i\beta(\omega)z]\exp[-i(\beta_0 + \beta_1(\omega - \omega_0)z]$. It is worth to emphasize that, at this point, β_0, β_1, and ω_0 can be considered free parameters without any particular physical meaning. By means of this

transformation, Eq. (3.23) can be recast as

$$\partial_z \tilde{A}(z,\omega) = i\left[\beta(\omega) - \beta_0 - \beta_1(\omega-\omega_0)\right]\tilde{A}(z,\omega) \\ +i(2\pi)^{-2}\int_{-\infty}^{\infty}\gamma(\omega,\omega_1,\omega_2,\omega-\omega_1+\omega_2)\tilde{A}(z,\omega_1)\tilde{A}^*(z,\omega_2)\tilde{A}(z,\omega-\omega_1+\omega_2)\mathrm{d}\omega_1\mathrm{d}\omega_2. \tag{3.25}$$

From a numerical point of view, solving this equation would become not affordable due to the sampling required by γ. However, we will check in the summary of Paper V that even in cases where the mode that supports the propagation is quite dispersive, the approximation $\gamma(\omega,\omega_1,\omega_2,\omega-\omega_1+\omega_2) \approx \gamma(\omega,\omega,\omega,\omega) \equiv \gamma(\omega)$ could work reasonably well. A discussion about physical situations where this approximation can be argued is found in [58]. Some authors have even studied new nonlinear effects related to the full frequency dependence of the nonlinear coefficient [59, 60]. These multidispersion effects will not be considered here. It is easy to check the huge numerical benefit provided by this assumption:

$$\begin{aligned}(2\pi)^{-2}&\int_{-\infty}^{\infty}\mathrm{d}\omega_1\mathrm{d}\omega_2\tilde{A}(\omega_1)\tilde{A}^*(\omega_2)\tilde{A}(\omega-\omega_1+\omega_2) \\ &= (2\pi)^{-2}\int_{-\infty}^{\infty}\mathrm{d}\omega_2\left[\int_{-\infty}^{\infty}\mathrm{d}\omega_1\tilde{A}(\omega_1)\tilde{A}(\omega+\omega_2-\omega_1)\right]\tilde{A}^*(\omega_2) \\ &= (2\pi)^{-1}\int_{-\infty}^{\infty}\mathrm{d}t\left[\int_{-\infty}^{\infty}\mathrm{d}\omega_2 A(\omega_2)e^{-i\omega_2 t}\right]^* A^2(t)e^{i\omega t} = \mathfrak{F}\left[|A(t)|^2A(t)\right].\end{aligned} \tag{3.26}$$

Finally, the so-called generalized nonlinear Schrödinger equation is obtained in its usual form [13]

$$\partial_z\tilde{A}(z,\omega-\omega_0) = i\beta_p(\omega)\tilde{A}(z,\omega-\omega_0) + i\gamma(\omega)\mathfrak{F}\left[|A(t)|^2A(t)\right]. \tag{3.27}$$

For numerical convenience, ω_0 is identified with the carrier frequency of the input pulse and both the envelope and $\mathfrak{F}$ are centred at ω_0. Furthermore, it is common to define $\beta_p(\omega) = \beta(\omega) - \beta_0 - \beta_1(\omega-\omega_0) = \sum_{k=2}\beta_k(\omega-\omega_0)^k/k!$, where $\beta_k = \mathrm{d}^k\beta/\mathrm{d}\omega^k|_{\omega_0}$, and β has been developed in Taylor series around ω_0. I consider it is worth mentioning how must the solution of Eq. (3.27) be interpreted. On the one side, the electric field spectrum for positive frequencies is given by

$$\tilde{\mathbf{E}}(\mathbf{x},\omega-\omega_0) = \tilde{A}(z,\omega-\omega_0)e^{i(\beta_0+\beta_1(\omega-\omega_0)z)}\mathbf{e}(\mathbf{x}_t,\omega-\omega_0). \tag{3.28}$$

Note that $|\tilde{A}(z,\omega-\omega_0)|^2$ only provides the spectrum of the electric field if the mode dispersion can be neglected. On the other side, the temporal picture of the output pulse is provided by

$$\mathbf{E}(\mathbf{x},\tau) = (2\pi)^{-1}\int_{-\infty}^{\infty}\tilde{A}(z,\omega-\omega_0)e^{i\beta_0 z}e^{-i(\omega-\omega_0)\tau}\mathbf{e}(\mathrm{x}_t,\omega-\omega_0)\,\mathrm{d}\omega, \quad (3.29)$$

where $\tau = t-\beta_1 z$ is a temporal coordinate whose origin at each z-plane is defined by the arrival time of a signal moving at the group velocity of the pulse, $1/\beta_1$ [13]. The introduction of the new envelope $\tilde{A}(z,\omega)$ is, in this way, justified also for numerical purposes. Therefore, the information provided by

$$\left|\int_{-\infty}^{\infty}\mathrm{d}\omega\tilde{A}(z,\omega-\omega_0)e^{-i(\omega-\omega_0)\tau}\right|^2 \quad (3.30)$$

is only directly related to experimental measurements when the mode is nearly constant along the spectrum.

3.4 Conservation laws

In this section, the theoretical tool that supports our inverse nonlinear design will be derived. This results corresponds to a conservation law of the GNLSE. Several pulse invariants was already pointed out in the seminal work by Zakharov and Shabat [2]. In that work, the authors apply the inverse scattering method to find the stationary solutions for the nonlinear Schrödinger equation (NLSE), *i.e.*, for the Eq. (3.27) but keeping β_2 and γ constant. For these purposes, a description of GVD in the time domain is required. Consequently, the conservation laws shown in that work are also expressed in the time domain. The effects of higher-order dispersive effects on these conserved quantities have also been studied in the time domain [31, 64]. These conservation laws are naturally interpreted from a Hamiltonian formulation of the GNLSE and have been applied to study the stability of solitons in presence of higher-order dispersion [65, 66]. Nevertheless, we do not follow this approach. We will take advantage of these invariants in a similar way to [67, 68]. In these works, A. Picozzi and co-workers propose a thermodynamic formulation of SC generation. These authors generalized the conservation law proposed by Zakharov and Shabat and analyze the effect of higher-order dispersion by means of averaged quantities of the pulse that experiences such a spectral broadening.

Our inverse nonlinear design also propose to study some properties of the SC generation without a complete knowledge of the pulse profile. We will

exploit the averaged quantities involved in the generalized version of the above conservation law to quantify the stress of the nonlinear and dispersive effects at each propagation distance. This approach will be useful in Papers II and V to study some consequences of OWB.

Let us consider the propagation equation for the spectrum. According to Eq. (3.27),

$$\partial_z|\tilde{A}|^2 = 2\Re(\tilde{A}^*\partial_z\tilde{A}) = \gamma(\omega)2\Re\left(i\tilde{A}^*\mathfrak{F}(|A|^2A)\right). \tag{3.31}$$

Now, by integrating over ω, it is derived

$$\begin{aligned}\partial_z\int_{-\infty}^{\infty}\mathrm{d}\omega\,\gamma^{-1}(\omega)|\tilde{A}(z,\omega)|^2 &= 2\Re\left(i\int_{-\infty}^{\infty}\mathrm{d}\omega\tilde{A}^*\int_{-\infty}^{\infty}\mathrm{d}t|A|^2Ae^{i\omega t}\right)\\ = 2\Re\left(i\int_{-\infty}^{+\infty}\mathrm{d}t\left(\int_{-\infty}^{\infty}\mathrm{d}\omega\tilde{A}e^{-i\omega t}\right)^*|A|^2A\right) &= 2\Re\left(i2\pi\int_{-\infty}^{\infty}\mathrm{d}t|A|^4\right) = 0.\end{aligned} \tag{3.32}$$

This conserved quantity was already shown in [60, 67]. If Eq. (3.31) is multiplied by $\beta_p(\omega)$, which is assumed to be real, and taking into account Eq. (3.27):

$$\begin{aligned}\partial_z\beta_p(\omega)|\tilde{A}|^2 &= 2\Re\left(i\beta_p(\omega)\tilde{A}^*\gamma(\omega)\mathfrak{F}(|A|^2A)\right)\\ &= 2\Re\left(\left[-\partial_z\tilde{A}^* + \{i\gamma(\omega)\mathfrak{F}(|A|^2A)\}^*\right]\left[\gamma(\omega)\mathfrak{F}(|A|^2A)\right]\right)\\ &= -2\Re\left(\partial_z\tilde{A}^*\gamma(\omega)\mathfrak{F}(|A|^2A)\right).\end{aligned} \tag{3.33}$$

Similarly to the first pulse invariant, the following conservation law is derived

$$\partial_z\left(\int_{-\infty}^{\infty}\mathrm{d}\omega\,\beta_p(\omega)\gamma^{-1}(\omega)|\tilde{A}(z,\omega)|^2 + \frac{2\pi}{2}\int_{-\infty}^{\infty}\mathrm{d}t\,|A(z,t)|^4\right) = 0, \tag{3.34}$$

where $\gamma(\omega)$ is assumed to be real. This conserved quantity was already included in [67] for a $\gamma(\omega) = \gamma_0 + \gamma_1(\omega - \omega_0)$, where $\gamma_k = \mathrm{d}^k\gamma(\omega)/\mathrm{d}\omega^k|_{\omega_0}$. Finally, I can define the next z-dependent functions

$$\mathcal{L}_{\mathrm{D}}^{-1}(z) = \frac{\int_{-\infty}^{\infty}\mathrm{d}\omega\,\beta_p(\omega)\gamma^{-1}(\omega)|\tilde{A}(z,\omega)|^2}{\int_{-\infty}^{\infty}\mathrm{d}\omega\,\gamma^{-1}(\omega)|\tilde{A}(z,\omega)|^2}, \tag{3.35}$$

$$\mathcal{L}_{\mathrm{NL}}^{-1}(z) = \frac{2\pi\int_{-\infty}^{\infty}\mathrm{d}t\,|A(z,t)|^4}{2\int_{-\infty}^{\infty}\mathrm{d}\omega\,\gamma^{-1}(\omega)|\tilde{A}(z,\omega)|^2}, \tag{3.36}$$

to express the above constant of motion in a more suggesting way

$$\mathcal{L}_{\mathrm{D}}^{-1}(z) + \mathcal{L}_{\mathrm{NL}}^{-1}(z) = \mathcal{L}_{\mathrm{D}}^{-1}(0) + \mathcal{L}_{\mathrm{NL}}^{-1}(0). \tag{3.37}$$

This conservation law, written in this form, will be the key tool in our inverse nonlinear design since it allows to analyze the pulse evolution from a simplified picture keeping the main physical effects at work. Its application appear in Papers II and V.

Chapter 4

Silicon-on-insulator waveguides simulations

Despite SOI is the platform where we will perform our SC generation calculations, we will not focus on the plethora of applications based on these materials [69,70]. Here we present our preliminary analysis to evaluate the numerical accuracy of the simulations of SOI waveguides provided by our homemade software. It is an iterative Fourier algorithm that provides all the components of the electromagnetic field of the waveguide mode and the corresponding propagation constant solving Eq. (A.13) [84]. Simulations of these waveguides are demanding, compared to step-index or even photonic crystal fibers, due to their high index contrast. The information included in this chapter completes that included in Paper IV. Therefore, this chapter belongs to the inverse linear design part.

4.1 Numerical issues

Let us consider a silicon cylinder surrounded by silica, see inset of Fig. 4.1(a). Their modes satisfy an ordinary differential equation in its radial coordinate, due to its rotational invariance, that can be analytically solved [12, 13]. The fundamental mode inside the core is found to be $J_0(\rho/\rho_{\text{core}})$, where J_0 is the Bessel function of order 0, and $\rho_{\text{core}} \propto \lambda/(n_{\text{core}}^2 - n_{\text{eff}}^2)^{1/2}$ [13]. In the cladding, the fundamental mode is given by $K_0(\rho/\rho_{\text{clad}})$, where K_0 is the modified Bessel function of order 0, and $\rho_{\text{clad}} \propto \lambda/(n_{\text{eff}}^2 - n_{\text{clad}}^2)^{1/2}$ [13]. The decay of the mode amplitude along the radial coordinate is then controlled by ρ_{core} and ρ_{clad}.

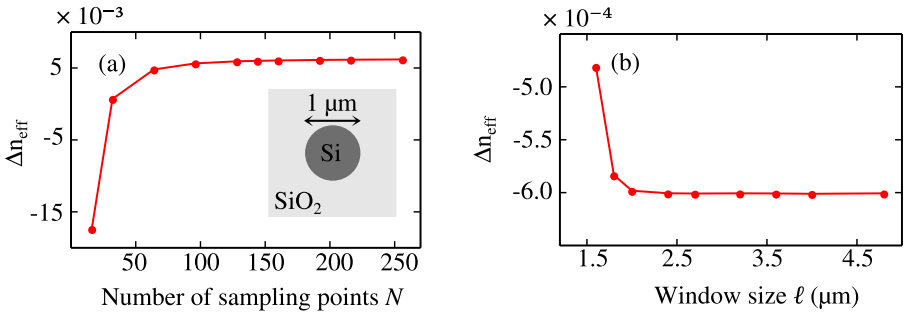

Figure 4.1: (a) Convergence process of the difference between the effective index numerically computed and the analytical value, Δn_{eff}. The spatial window size is fixed, $\ell = 1.2\,\mu$m, to find the resolution required for the cross-section shown in the inset. Convergence is reached at $N = 96$. (b) Analogous process keeping $\delta = 12.5\,\mu$m to evaluate what ℓ is needed. Convergence is reached at $\ell = 2\,\mu$m ($N = 160$).

Since $n_{\text{clad}} < n_{\text{eff}} < n_{\text{core}}$ and $n_{\text{Si}} - n_{\text{SiO}_2} \approx 2$ is the index contrast, while in standard single-mode step-index fibers is around 0.003 [13], this decay is much steeper in SOI waveguides. Accordingly, these waveguides usually require a higher resolution and therefore, more computational resources and time.

We show in Fig. 4.1 one example of a preliminary study to obtain the resolution, δ, and spatial window size, ℓ, to properly calculate the eigenvalues (the propagation constants) and eigenvectors (modes fields) corresponding to a waveguide. We directly plot the differences between the effective index and its analytical value $n_{\text{eff}} = 3.19237$ for $\lambda = 1.9\,\mu$m. Note that the absolute error is less than 10^{-3} for $\delta \leq 12.5\,$nm and $\ell \geq 2\,\mu m$. Since the waveguide dispersion will play an important role in our work, we can use the case of the cylinder to estimate the error of the dispersion that is numerically calculated. We conclude from Fig. 4.2 that the numerical accuracy achievable in our effective index calculations produces an absolute error around 10^{-3} on the dispersion values. This must be kept in mind for the results shown Papers IV and V, relative to SOI waveguides.

The high index contrast of SOI waveguides also increases the weight of the geometrical contribution to the waveguide dispersion [71]. It allows to engineer the dispersion by means of the waveguide cross-section design. However, several geometrical degrees of freedom are often required. It enhances the complexity of both the design and the fabrication techniques. In this thesis, we will

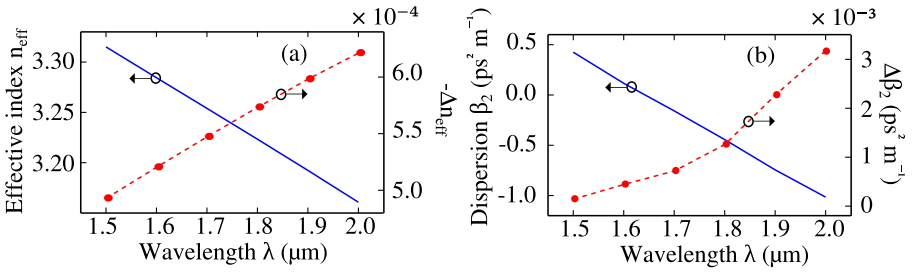

Figure 4.2: (a) Analytically calculated effective index (solid curve) and its difference with respect to the numerical value, $-\Delta n_{\text{eff}}$ (dashed curve). (b) Analogous to (a) but considering the dispersion β_2.

exploit the properties of a silicon strip waveguide on a silica substrate with air as the cover, with a silica slot inserted in the silicon channel, see Fig. 4.3(a). This kind of cross-section was firstly proposed by Zhang *et al.* [9]. Here we will only address the numerical effects arisen when cross-sections with parallel interfaces are analyzed. We will see what effects are produced by these rectangular structures and how do they generate undesired numerical artefacts. This fact is particularly important for the cross-section used in this work.

In the above strip-slot waveguide the quasi-transverse magnetic (TM) fundamental mode is essentially polarized in the vertical direction, *i.e.*, it is normal to the slot interfaces. As the wavelength increases, the strip mode also enlarges. Nevertheless, the boundary condition of the normal electric field component imposes that it must be $n_{\text{Si}}^2/n_{\text{SiO}_2}^2$ times higher just above the lower slot interface (inside the silica layer) than just below (inside the silicon layer) [72, 73]. It induces a strong confinement of the electric field inside the slot at longer wavelengths [9], see Fig 4.3(b). In other words, as the wavelength increases, a transition between a strip and slot mode is produced [9]. Among other effects, this property makes the numerical sampling around the lower slot interface critical. If the structure is parallel to the grid, the effective index shows a high sensitivity to the position of the closest row of sampling points to the interface. It difficults even more the numerical calculation of derivatives with respect to the geometrical parameters of the effective index and dispersion. This point is significant in Paper IV to check the accuracy of our method to compute the gradient of the propagation constant. Certainly, it corresponds to a numerical artefact that is detrimental to the convergence, see Fig. 4.3(c). We solved this trouble by slightly rotating the cross-section an angle around δ/w, where w is the width of the waveguide, see Fig. 4.3(a), to

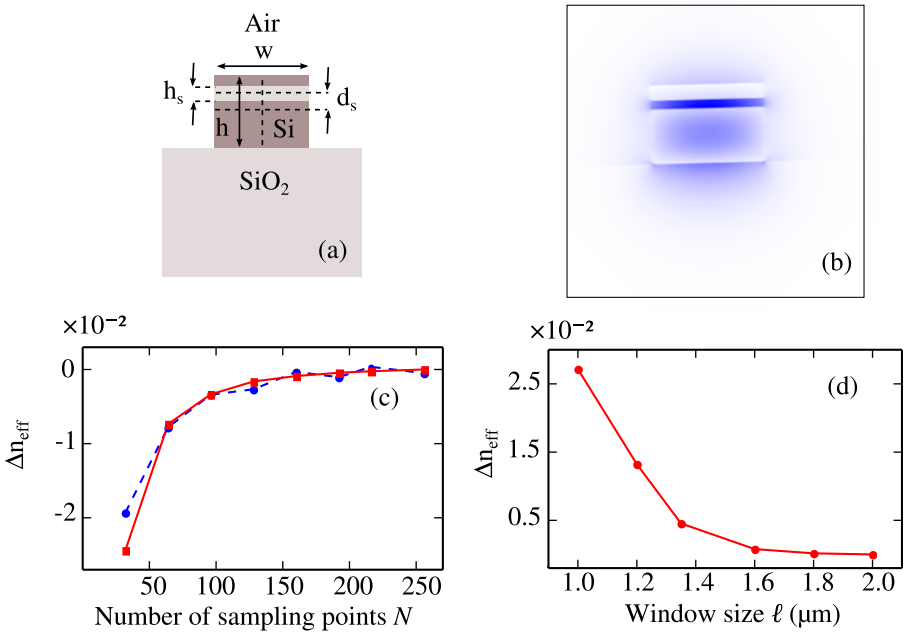

Figure 4.3: (a) Cross-section of the waveguide. Here we consider $w = 650\,\text{nm}$, $h = 460\,\text{nm}$, $h_s = 50\,\text{nm}$ and $d_s = 115\,\text{nm}$. (b) Component of the electric field vertically polarized. (c) Comparison between the convergence, at a $\ell = 1\,\mu\text{m}$, of a cross-section parallel to the sampling grid (dashed curve) and the corresponding to a slightly rotated (1.5 °) structure (solid curve). (d) Convergence of the rotated cross-section at $\delta = 6.25\,\text{nm}$. For (b–d), $\lambda = 1.9\,\mu\text{m}$.

ensure a more representative sampling of the transition between media that makes the convergence smoother, see Fig. 4.3(c). It is worthwhile to indicate that we attend to the effective medium theory to take into account the transition of the refractive index around interfaces [78, 79]. Based on our analysis of the cylindrical waveguide, an accuracy below than 10^{-3} is achieved when $N = 160$, corresponding to $\delta = 6.25\,\text{nm}$, are considered. Finally, this accuracy is kept when $\ell = 1.8\,\mu\text{m}$ is used, thus $N = 288$ are required to numerically describe this cross-section. The procedure presented here explains the reasons of the numerical parameters, N and ℓ, considered in Paper IV and V.

4.2 Explicit expression for the nonlinear coefficient

Since measurements of the material dispersion of nonlinearity with respect to multiple frequencies lack, the third-order susceptibility corresponding to FWM is often expressed as

$$\chi^{(3)}_{ijkl}(\omega;\omega_1,-\omega_2,\omega_3) \equiv \chi(\omega)\Theta_{ijkl} = \frac{4}{3}\epsilon_0 c n^2(\omega)\left(n_2(\omega) + i\frac{c}{\omega}\frac{\beta_{\mathrm{TPA}}(\omega)}{2}\right)\Theta_{ijkl}, \tag{4.1}$$

where n_2 is the Kerr index, β_{TPA} is the TPA coefficient and dispersive and vectorial effects have been factorized. Both parameters can be experimentally measured [74–76]. For silicon, according to [38],

$$\Theta_{ijkl} = \frac{\rho}{3}(\delta_{ij}\delta_{kl} + \delta_{ik}\delta_{jl} + \delta_{il}\delta_{jk}) + (1-\rho)\delta_{ijkl}, \tag{4.2}$$

where $\rho \approx 1.27$, δ_{ij} and δ_{ijkl} correspond to the Kronecker delta for two or four indices. The first term is isotropic and therefore, it does not depend on the coordinate system. Nevertheless, the second term is anisotropic and has been written assuming a coordinate system parallel to the crystallographic axes of silicon. This term will not considered in this work, as in [52]. For silica, $\rho = 1$. For the sake of completeness, an explicit expression for Eq. (3.24) will be derived here for any inhomogeneous cross-section composed by materials with isotropic nonlinear responses. If the integrand of Eq. (3.24) is developed for a homogeneous region assuming that the electric and magnetic fields with real transverse components $\mathbf{e}_t$ and $\mathbf{h}_t$, and pure imaginary longitudinal components e_z an h_z [49], it leads to

$$\begin{aligned}
\chi^{(3)}_{ijkl}e_i^* e_j e_k^* e_l &= \chi(\omega)\frac{\rho}{3}\left(2e_i^* e_i e_k^* e_k + (e_i e_i)^* e_j e_j\right) \\
&= \chi(\omega)\frac{\rho}{3}\left(2(\mathbf{e}_t\cdot\mathbf{e}_t + |e_z|^2)^2 + (\mathbf{e}_t\cdot\mathbf{e}_t - |e_z|^2)^2\right) \\
&= \chi^{(3)}(\omega)\rho\left((\mathbf{e}_t\cdot\mathbf{e}_t)^2 + \frac{2}{3}\mathbf{e}_t\cdot\mathbf{e}_t|e_z|^2 + |e_z|^4\right),
\end{aligned} \tag{4.3}$$

which was derived in [77]. Finally, if Eq. (3.24) is rewritten including explicitly the fields normalization, it is obtained

$$\gamma(\omega) = \sum_k \left[\frac{\omega n_2^{(k)}(\omega)}{c} + i\frac{\beta_{\mathrm{TPA}}^{(k)}(\omega)}{2} \right] \times \left[\frac{\rho^{(k)}[n^{(k)}(\omega)]^2 \varepsilon_0 \int_{\mathcal{S}_k} \left[(\mathbf{e}_t \cdot \mathbf{e}_t)^2 + \frac{2}{3}\mathbf{e}_t \cdot \mathbf{e}_t |e_z|^2 + |e_z|^4 \right] \mathrm{d}S}{2\mu_0 (\int_{\mathcal{S}} (\mathbf{e}_t \times \mathbf{h}_t) \cdot \hat{\mathbf{z}}\, \mathrm{d}S)^2} \right], \quad (4.4)$$

where the subindex k denotes each homogeneous material of the cross-section. It is useful to write the above equation here although it does not include any novelty. It explicitly shows how to compute the nonlinear coefficient from the experimental data, namely n_2 and β_{TPA}, and the mode fields provided by any software.

I complete this section presenting in Fig. 4.4 the numerical fits from experimental measurements of the Kerr index, n_2, and the TPA coefficient, β_{TPA} of silicon. All fits correspond to a Cauchy model of the form $\sum_{k=0}^{2} a_k/\lambda^{2k}$, which parameters appear in Table 4.1. Silicon will be described in our simulations in Paper V by the mean values of those provided by these fits. Note that the measurements of [75, 76] are significantly different (it justifies that there is no need to include minor contributions like the silicon anisotropy in the present study). Both the numerical analysis of the previous section and the data provided here contain the procedure required to compute the waveguide physical properties. We stated in the introduction that these functions actually represent the waveguide when a pulse propagation is studied through the GNLSE. Therefore, it completes the numerical studies shown in Papers IV and V to support the conclusions presented in this thesis.

Table 4.1: Cauchy coefficients in units of Fig. 4.4 and λ expressed in μm.

Magnitude (units)	a_0(units)	a_1 (units μm^2)	a_2 (units μm^4)
n_2(m^{2}W^{-1}) [75]	-9.31422×10^{-19}	1.78924×10^{-17}	-2.25824×10^{-17}
β_{TPA}(m W^{-1}) [75]	-8.03605×10^{-12}	5.07515×10^{-11}	-4.63796×10^{-11}
n_2(m^{2}W^{-1}) [76]	1.83568×10^{-17}	-3.49209×10^{-17}	2.02215×10^{-17}
β_{TPA}(m W^{-1}) [76]	-9.18175×10^{-12}	6.22685×10^{-11}	-3.11114×10^{-11}

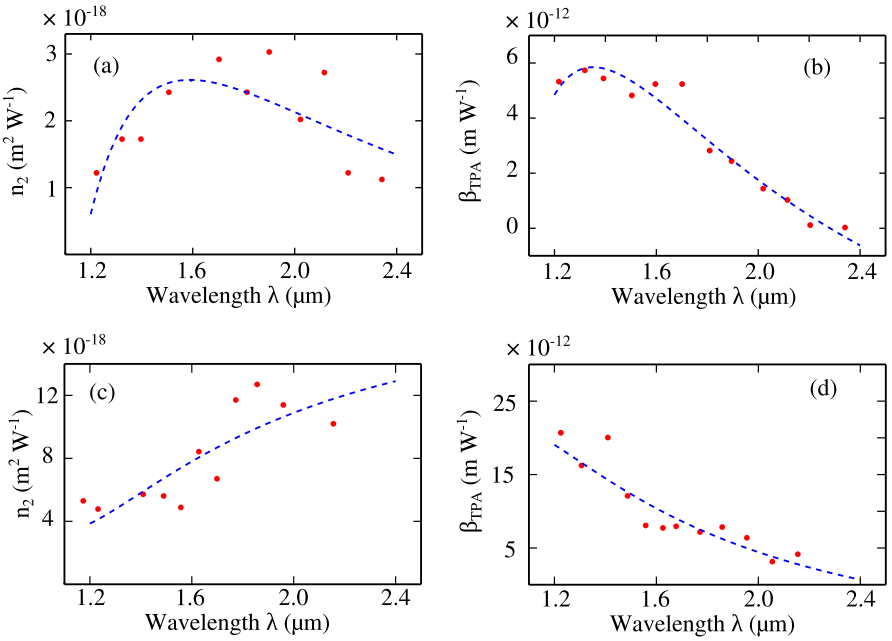

Figure 4.4: Kerr index (a) and TPA coefficient (b) measurements from [75] and the corresponding Cauchy fits (see Table 4.1). Analogously in (c) and (d) from data presented in [76].

Chapter 5

Summary of Papers

The following summary contains the main conclusions of this thesis as well as some unpublished results involving different points that were not addressed when the papers were published. They appear in chronological order of publication, but their content must be organized as follows. Papers II and IV present the most important theoretical and numerical findings of this thesis. They enable our inverse design approach. Paper I studies how to reduce the impact of nonlinear losses on the spectral broadening, particularly in silicon waveguides. Paper V corresponds to an application of the results of Papers II, IV and I to obtain a coherent mid-infrared near octave spanning SC generation in silicon waveguides pumping at telecom wavelengths. It corresponds to an example of our inverse design procedure. Finally, Paper III describes the coherence properties of Kerr combs in microring resonators by means of a numerical study.

Paper I

In spite of the strong optical confinement and the large nonlinearity of silicon waveguides, the semiconductor nature of this platform also produces some detrimental effects on continuum light generation. Particularly, nonlinear pulse propagation is notably affected by TPA at telecom wavelengths. Free carriers arisen from this process also induce additional nonlinear losses, namely, free carrier absorption (FCA). Unlike linear losses, these processes depend on the intensity and consequently do not evenly affect all the light pulse. It suggests that nonlinear losses should be sensitive to the input pulse shape and so,

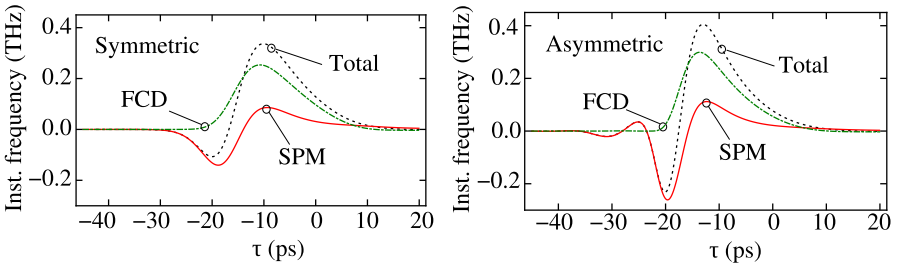

Figure 5.1: Comparison of the different contributions to the instantaneous frequency for both the unmodulated and modulated pulses with 1kW peak power.

their pernicious impact on spectral broadening could be reduced by means of suitable pulse profiles.

Our goal in this work was to study the spectral broadening of asymmetric input pulses produced by adding a cubic spectral phase $\eta(\omega - \omega_0)^3$, where η quantifies the so-called skewness, to Gaussian pulses. Our interest focused on the interplay between SPM and free carrier dispersion (FCD), that produces new frequencies, and TPA and FCA, that inhibit such an effect. So, we decided to consider ps-long pulses that propagate along 1 cm-long silicon waveguide to safely neglect GVD [36]. For high (although realistic [37]) powers, where the generation of blue-shifted frequencies are mainly governed by FCD, we numerically observed an improvement up to 40% on the bandwidth, for both longer and shorter wavelengths when a pulse with a proper positive skewness propagates. This asymmetry gives rise to a steeper leading edge of the pulse. It produces an increased minimum chirp induced by SPM that allows us to understand the additional broadening towards longer wavelengths. Moreover, the generation of new frequencies concentrates for such pulses at earlier time stages. Because the carriers accumulate at the trailing edge of the pulse, the impact of FCA is also reduced and so, the broadening towards shorter wavelengths enhances. Fig. 5.1 shows a calculation of the SPM and FCD contributions of the instantaneous frequency, for both symmetric and the optimum skewed pulse, that corroborates our reasoning.

Although this work focused on FCA, I complete it here by means of an analytical study of TPA when positive skewed pulses propagate based on Eqs. (3) and (4) of Paper I when FCA and linear losses are neglected. Fig. 5.2(a) illus-

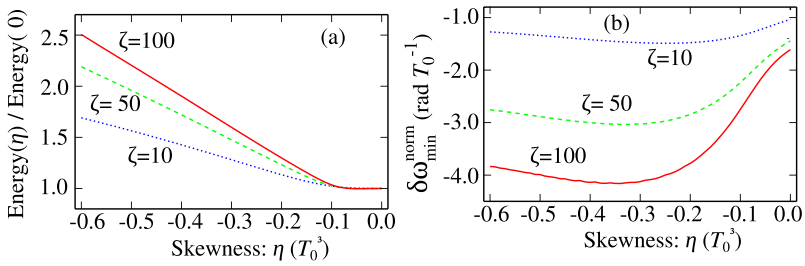

Figure 5.2: Normalized energy (a) and normalized minimum chirp, $\delta\omega_{\rm min}^{\rm norm} = (\gamma_0^{\rm re}/\gamma_0^{\rm im})\delta\omega_{\rm min}$ (b) at different normalized propagation distances, $\zeta = \gamma_0^{\rm im} P_0 z$, being $\gamma_0^{\rm im}$ ($\gamma_0^{\rm re}$) the imaginary (real) part of γ_0 and P_0 the peak power of the input pulse, as a function of the skewness of a Gaussian input pulse in units of T_0^3, where T_0 denotes the temporal width of the input pulse. The lack of symmetry in the input pulse profile increases the energy and the minimum chirp of the output pulse compared to the symmetric case ($\eta = 0$).

trates how the impact of TPA on asymmetric profiles is reduced. In addition, Fig. 5.2(b) shows that the spectral broadening (towards red-shifted frequencies) can be optimized through a proper skewness. I will take advantage of these calculations in Paper V.

As we mentioned in the introduction, our overall goals were related to SC generation in silicon waveguides. Particularly, we worked on the normal dispersion regime, where a strong spectral broadening by SPM was required [80]. Despite the improvement on the spectral broadening based on pulse shaping, it was not enough to generate SC based exclusively on SPM in silicon waveguides. Although OWB solves this challenge, as I will demonstrate in Paper V, asymmetric pulses play an important role to obtain SC based on this scheme in presence of TPA.

Paper II

Our goal in this paper was twofold. One the one hand, a conservation law for pulse propagation governed by a nonlinear-Schrödinger-type equation, including an arbitrary GVD curve, was presented. We want to state here that this property had already been shown in [67]. This law can even be modified to include the dispersion of the nonlinear coefficient, as it was demonstrated in

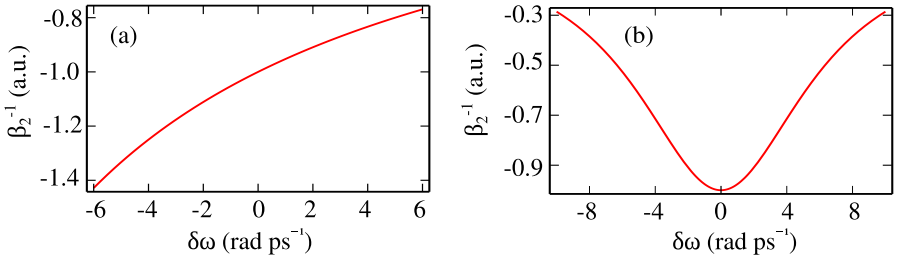

Figure 5.3: Minus the inverse of the GVD for a) a linear GVD profile (*i.e.*, considering third-order dispersion), and b) a parabolic GVD profile (*i.e.*, considering fourth-order dispersion).

the introduction of this thesis. On the other hand, some features of the pulse evolution were studied without needing a detailed description of the pulse. To this end, I proposed two new functions that quantify the weight of SPM and GVD at each z-distance. For highly nonlinear systems in all-normal dispersion regime, this conservation law implies that $\int_{-\infty}^{+\infty} \beta_p(\omega)|A(z,\omega-\omega_0)|^2$ approaches to a constant that depends on the input pulse. This fact points out a strong correlation between the output pulse spectrum and the dispersive properties of the waveguide. It suggested interesting applications related to spectral shaping of pulses based on dispersion engineering.

This result was indeed derived from a mathematical analysis of the GNLSE. I numerically confirmed that the pulse spectrum acquires the GVD curve shape and OWB also took place along the propagation. With the aim of understanding the connection between these two phenomena and so, improve our control over them, I proposed an analytical approach of the pulse propagation under conditions that allow OWB. According to this simplified model, I could study the spectral changes produced by OWB based on the degenerate FWM processes between waves previously generated by SPM. It led to assert that the power flow from central frequencies to higher and lower ones is strongly controlled by $-1/\beta_2(\omega)$. In Fig. 5.3 we plot $-1/\beta_2$ as a function of $\delta\omega_p = \omega_p - \omega_0$ for both a linear dispersion profile, *i.e.*, $\beta_2(\omega_p) = \beta_2(\omega_0)[1 + m\,\delta\omega_p]$, and a parabolic dispersion profile, *i.e.*, $\beta_2(\omega_p) = \beta_2(\omega_0)[1 + 1/2\,a\,\delta\omega_p^2]$. We use in the plots $m = (10/200)$ ps and $a = (1/20)$ ps^2, which corresponds to the values used in our numerical simulations shown in the paper. These plots indicate that the power flow around the central frequency ($\delta\omega_p = 0$), $\delta P_p(z)$, is quasi-linear for a linear dispersion profile, and concave for a parabolic dispersion profile. This qualitative claim is in agreement with our numerical results and

justified that the dispersion-to-spectrum mapping is produced by OWB.

Although this paper focuses on spectral shaping applications, it allowed us to provide a new approach to study the OWB process. It is in the origin of our inverse nonlinear design step that will be applied in Paper V.

Paper III

Recently, comb generation in ring microresonators in a silicon nitride platform was experimentally demonstrated [81]. Two physically different ways have been also identified to produce them after pumping one of the microresonator resonances. On the one hand, if the adjacent resonances are firstly filled by degenerate FWM, then other lines will appear by nondegenerate FWM involving the lines initially generated. This is the so-called type I comb formation and it was also experimentally demonstrated to keep good coherence [82]. On the other hand, nonadjacent resonances can be initially formed by degenerate FWM. Furthermore, they can also generate new lines by themselves also through degenerate FWM. Certainly, other lines will be produced by nondegenerate FWM between all these frequencies in such a way that noise fluctuations have a great impact over the comb coherence [82]. It corresponds to the so-called type II comb formation. The generation of these Kerr combs can be simulated by means of a nonlinear-Schrödinger-type equation including a driving term and an additional periodic boundary condition to take into account that only a discrete set of frequencies can contribute to the field. We used this approach to study the coherence properties of Kerr combs. The type of formation can be chosen taking advantage of analytical expressions of the MI gain. We numerically solved the above equation and confirmed the loss of coherence only for type II combs. In addition, we also checked pulse formation by properly ramping the detuning between the pump frequency and the closest resonance line [83].

Despite this work mainly focuses on coherence, we underline that the dynamics of microring resonator is studied through a nonlinear Schödinger equation. It allows to apply the analytical and numerical tools presented in this thesis for such a systems. For example, the enhancement of coherence properties or the pulse stabilization could be addressed following our inverse procedure, presented Papers II, IV and V.

Paper IV

This paper contains the two main results around our inverse linear design, including details to implement the corresponding numerical algorithm. It is, in this sense, self-contained. Firstly, I explicitly derived a close expression to compute the gradient of the propagation constant of a guiding structure by using the fields of the corresponding mode. Its full-vectorial nature was considered. It means that Maxwell's equations do not only provide the propagation constant of a system with translational symmetry, but also its derivatives with respect to all the geometrical parameters. Among other details, we highlight two of them. On the one side, here we consider smooth transitions of the dielectric tensor across the interfaces. In this way, we do not describe the cross-section of the waveguide by means of step functions. The effective index theory [79] provides us analytical forms to simulate the changes experienced by the dielectric tensor in the neighbourhood of the interfaces. On the other side, I computed those derivatives by means of the field components which do not suffer sharp transitions at each interfaces, according to the boundary conditions of the electromagnetic field.

We implemented these issues to calculate, in a few minutes, the gradient from the mode fields (that can be computed by *any* software). In a second step, and following previous works by our group [11], we took advantage of the above result to perform a linear optimization of high-index-contrast waveguides. Particularly, we concentrated on the dispersion curve. We defined several profiles to be recovered through a suitable design of a slotted strip waveguide on the SOI platform. We successfully applied this optimization procedure and obtain all targets in less than ten iterations. In addition, our algorithm allows us to add constraints on the parameters involved in the optimization, which could be of interest for future work related to the design of the nonlinear coefficient.

Paper V

This work illustrates the application of our inverse design procedure, based on Papers II and IV, for SC generation in silicon waveguides. To avoid the coherence degradation, the input pulse is pumped at the normal dispersion regime. Based on an analysis developed in terms of our generalized nonlinear and dispersive length functions, I derived the third-order dispersion required to optimize the spectral broadening owing to OWB. The effective nonlinearity of the waveguide was enhanced by using a skewed input pulse, allowing

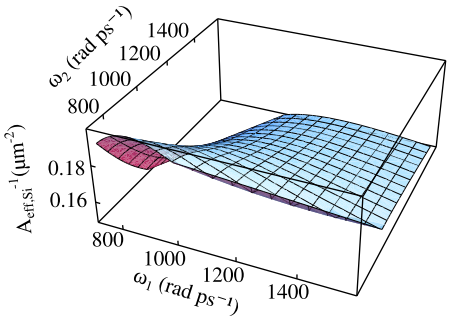

Figure 5.4: Inverse effective area as a function of two angular frequencies for ω corresponding to $\lambda = 1900\,\text{nm}$.

OWB to occur. Moreover, nonlinear mixing related to OWB takes place at the anomalous dispersion regime due to the third-order dispersion and consequently, generation of new frequencies is produced under good phase matching conditions. This step would correspond to our inverse nonlinear design.

During our inverse linear design step, I numerically found a realistic slotted strip waveguide on a SOI platform based on the original design provided by Zhang et al. [10], analogously to Paper IV, with a dispersion profile close to the target. Note that, in this case, the target curve is not flattened due to the presence of a third-order dispersion. Finally, the propagation of a short pulse throughout this realistic waveguide was simulated and it was obtained a near octave spanning SC generation, from telecom wavelengths, where the input pulse was pumped, to mid-infrared, keeping good level of coherence along the spectrum.

For the sake of completeness, I include here an additional calculation about one of the assumptions of the GNLSE. I checked whether the dispersion of the nonlinear coefficient can be reduced to only one frequency, as it is explained in the introduction. Since the Kerr index for silicon is two order of magnitude higher than silica (see Fig. 4.4), the main contribution to the nonlinear coefficient comes from silicon region. So, the nonlinear coefficient can be ap-

proximated in the following way

$$\begin{aligned}\gamma(\omega,\omega_1,\omega_2,\omega_3) \approx &\left[\frac{\omega n_2^{\mathrm{Si}}(\omega)}{c} + i\frac{\beta_{\mathrm{TPA}}^{\mathrm{Si}}(\omega)}{2}\right] \\ &\times \frac{\rho_{\mathrm{Si}} n_{\mathrm{Si}}^2(\omega)\varepsilon_0}{6\mu_0}\int_{\mathcal{S}_{\mathrm{Si}}} [e_i^*(\omega)e_i(\omega_1)e_k^*(\omega_2)e_k(\omega_3) \\ &+ e_i^*(\omega)e_i^*(\omega_2)e_j(\omega_1)e_j(\omega_3) + e_i^*(\omega)e_i(\omega_3)e_j(\omega_1)e_j^*(\omega_2)]\,\mathrm{d}S \\ &\equiv \left[\frac{\omega n_2^{\mathrm{Si}}(\omega)}{c} + i\frac{\beta_{\mathrm{TPA}}^{\mathrm{Si}}(\omega)}{2}\right] \times \frac{\rho_{\mathrm{Si}} n_{\mathrm{Si}}^2(\omega)}{A_{\mathrm{eff,Si}}(\omega,\omega_1,\omega_2,\omega_3)}, \quad (5.1)\end{aligned}$$

where $\omega_3 = \omega - \omega_1 + \omega_2$ and the effective area, A_{eff}, has been included since only one material is considered for our purposes here.

I plot in Fig. 5.4 the inverse of the effective area for the slotted strip waveguide obtained through our inverse dispersion engineering in this paper. It allows to evaluate the variations owing to the multiple dispersion effect, in a similar way to [60]. Since it is nearly constant, we expect this approximation works well even in this case, where the dispersion of the mode can not be entirely neglected. I analyzed in more detail the description of this effects in Chapter 2.

Chapter 6

Conclusions

As any other macroscopic electromagnetic phenomenon, SC generation in waveguides can be analyzed by directly solving Maxwell's equations. Nevertheless, the nonlinear Schrödinger equation has been proved to be useful to describe a plethora of nonlinear phenomena. This model allows to save computational resources and makes easier to identify the key mechanisms involved in each regime. Therefore, even its simplest version is fully justified, although extended versions of this equation are required to achieve accurate descriptions. Despite this fact, dealing with this equation is still challenging since it contains local terms in both the temporal (nonlinearities) and frequency (group velocity dispersion) domains. Consequently, SC in realistic waveguides is often studied by means of pure numerical approaches to that equation. The design of waveguides for nonlinear applications becomes arduous due to the lack of analytical tools to find suitable cross-sections or select the region of the space of the equation parameters.

This thesis has addressed these issues in a twofold manner. In a pulse propagation equation, waveguides are described through two frequency-dependent functions, namely, the propagation constant, β and the nonlinear coefficient, γ. Consequently, the nonlinear regime does not take place in a specific waveguide but a system defined by these functions. Based on this fact, we initially considered the design of β and γ and the nonlinear pulse propagation as disconnected problems. In this way, we developed tools to obtain the region of values of the parameters β and γ leading to some specific nonlinear behavior. In addition, we also implemented a software to find in a systematic and efficient way cross-sections that show nearly these properties. We call these steps inverse nonlinear and linear design.

Our inverse nonlinear design is based on a conservation law of the above equation. Attending to this property, pulse propagation in highly nonlinear systems at the normal dispersion regime can be analyzed in two-steps. In spite of the pulse profile is not described in detail, this approach provides suitable values of the third-order dispersion that lead to strong spectral broadening in such a conditions. I emphasize it corresponds to a truly inverse design. Indeed, given a specific waveguide with normal dispersion at some wavelength and a zero dispersion wavelength, we could determine the input pulse profile and propagation length where a supercontinuum generation would be observed. It turns out interesting in order to experimentally demonstrate this phenomenon. In future work, I expect this approach to be helpful in the study of other dynamical regimes (e.g., solitonic propagation) and the experimental measurement of higher-order dispersion.

Geometry possesses a significant impact on the dispersion of micrometric waveguides, since their dimensions are comparable to light wavelengths. The tight confinement of the mode fields in high-index-contrast waveguides makes this impact even stronger. Consequently, SOI waveguides allow to be engineered to obtain specific dispersion curves. In this work, we adapted a design strategy successfully applied by our group in photonic crystal fibers, to high-index-contrast waveguides. It required to derive a closed expression of the derivatives of the propagation constant with respect the available geometric parameters of the cross-section. In addition, the boundary conditions of fields were carefully taken into account to improve the accuracy of our calculations. This tool notably reduces the time needed to design the dispersion profile of waveguides. In this way, we can look more efficiently for realistic waveguides where phenomena, previously theoretically studied, can take place.

Finally, the realization of this thesis has been one of the most exciting experiences that I lived until now. It provided me some knowledge about how does light behave in waveguides. Well, in accordance to the title of my thesis, I could say that these years provided me useful tools to find waveguides where light behaves as we need... at least in some cases. Although the uncertainty of future is high, I only expect to enjoy the next years as much as these ones.

Appendix A

Electromagnetism in translation-invariant systems

In this appendix the eigenvalues equation corresponding to the starting point of Paper IV are derived. Moreover, the biorthogonality relation between the waveguide modes, that is the key property enabling our inverse linear design (see [11, 84, 85]), is also revisited. Therefore, this appendix addresses the unperturbed (or linear) problem (see Fig. 1.1), *i.e*, it does not involve the nonlinear polarization. On the other side, this property is also useful to derive the GNSLE due to nonlinearities are considered in a perturbative approach (see Chapter 2).

We begin with Maxwell's equations in a system with a homogeneous and isotropic permeability and where free charges and the electric current are absent. In the frequency domain, Maxwell's equations are given, in MKS units, by

$$\begin{aligned} \nabla \cdot (\varepsilon_0 \varepsilon \tilde{\mathbf{E}}) &= 0, && \text{(A.1)} \\ \nabla \cdot \tilde{\mathbf{H}} &= 0, && \text{(A.2)} \\ \nabla \times \tilde{\mathbf{E}} &= i\omega\mu_0 \tilde{\mathbf{H}}, && \text{(A.3)} \\ \nabla \times \tilde{\mathbf{H}} &= -i\omega\varepsilon_0 \varepsilon \tilde{\mathbf{E}}, && \text{(A.4)} \end{aligned}$$

where $\tilde{\mathbf{E}} = \mathfrak{F}(\mathbf{E}) = \int_{-\infty}^{\infty} \mathbf{E} \exp(i\omega t) \mathrm{d}t$ is the Fourier transform of the electric field, $\mathbf{E}$, $\mathbf{H}$ stands for the magnetic field, $\varepsilon = \varepsilon(\mathbf{x}_\mathrm{t}, \omega)$ is the dielectric tensor

of an invariant system along the z-coordinate (note that it only depends on the transverse coordinates, $\mathbf{x}_t$, and it does not include nonlinear effects), ε_0 and μ_0 represent the permittivity and permeability of the vacuum, respectively [12,49]. Our aim here is to derive eigenvalue equations for the transverse components of the magnetic and electric fields corresponding to the modes of translation-invariant systems along the z-direction characterized by the following dielectric tensor

$$\varepsilon = \begin{pmatrix} \varepsilon_{tt} & 0 \\ 0 & \varepsilon_{zz} \end{pmatrix}, \tag{A.5}$$

where ε_{tt} is a submatrix 2×2 that contains the transverse components of the dielectric tensor and ε_{zz} indicates the scalar related to its longitudinal component. This permittivity describes usual nonhomogeneous cross-sections. Particularly, it accounts for SOI waveguides even when the anisotropy induced by the interfaces is considered [79]. Moreover, we will check that this matrix leads to an eigenvalue equation for the transverse components of the magnetic and electric fields. Since Maxwell's equation are linear and the system considered is invariant along the z-coordinate, the following solutions with a separated z-dependence, the so-called modes, exist [12],

$$\tilde{\mathbf{H}} = \tilde{\mathbf{h}}(\mathbf{x}_t, \omega) e^{i\beta(\omega)z} = [\mathbf{h}_t(\mathbf{x}_t, \omega) + \hat{\mathbf{z}}\, h_z(\mathbf{x}_t, \omega)]\, e^{i\beta(\omega)z} \tag{A.6}$$

$$\tilde{\mathbf{E}} = \tilde{\mathbf{e}}(\mathbf{x}_t, \omega) e^{i\beta(\omega)z} = [\mathbf{e}_t(\mathbf{x}_t, \omega) + \hat{\mathbf{z}}\, e_z(\mathbf{x}_t, \omega)]\, e^{i\beta(\omega)z}, \tag{A.7}$$

where the subindex t stands the transverse components of the fields. At this point, it must be interpreted as a three dimensional vector with a zero longitudinal component. In order to derive the equation satisfied by the transverse components, let us decouple Eqs. (A.3) and (A.4),

$$\nabla \times \left(\varepsilon^{-1} \nabla \times \tilde{\mathbf{H}}\right) = \frac{\omega^2}{c^2} \tilde{\mathbf{H}}, \tag{A.8}$$

$$\nabla \times \nabla \times \tilde{\mathbf{E}} = \frac{\omega^2}{c^2} \varepsilon \tilde{\mathbf{E}}. \tag{A.9}$$

Note that these equations do not assume any restriction on ε, thus keeping vectorial effects [86]. Now, Eq. (A.8) can be developed using Eq. (A.6),

$$\begin{aligned} \nabla \times \tilde{\mathbf{H}} &= (\nabla_t + \hat{\mathbf{z}}\partial_z) \times e^{i\beta z} (\mathbf{h}_t + \hat{\mathbf{z}}\, h_z) \\ &= e^{i\beta z} (\nabla_t \times \mathbf{h}_t + \hat{\mathbf{z}} \times \mathbf{h}_t i\beta + \nabla_t \times \hat{\mathbf{z}}\, h_z) \\ &= e^{i\beta z} (\hat{\mathbf{z}} \nabla_t^T \eta \mathbf{h}_t - \eta \mathbf{h}_t i\beta + \eta \nabla_t h_z). \end{aligned} \tag{A.10}$$

where the complete antisymmetric tensor in two dimensions

$$\eta = \begin{pmatrix} 0 & 1 \\ -1 & 0 \end{pmatrix}, \tag{A.11}$$

the gradient with respect to the transverse coordinates, ∇_t, and its transpose, ∇_t^T have been introduced. This equation is not only useful by itself but it provides how does the rotational act onto an arbitrary vector whose z-dependence is $\exp(i\beta z)$. According to this result and after some algebra, it is derived

$$\begin{aligned}\nabla \times \left(\varepsilon^{-1}\nabla \times \tilde{\mathbf{H}}\right) &= e^{i\beta z}\hat{\mathbf{z}}\nabla_t^T\eta\left(-\varepsilon_{tt}^{-1}\eta\mathbf{h}_t i\beta + \varepsilon_{tt}^{-1}\eta\nabla_t h_z\right) \\ &- e^{i\beta z}i\beta\eta\left(-\varepsilon_{tt}^{-1}\eta\mathbf{h}_t i\beta + \varepsilon_{tt}^{-1}\eta\nabla_t h_z\right) + e^{i\beta z}\eta\nabla_t\left(\varepsilon_{zz}^{-1}\nabla_t^T\eta\mathbf{h}_t\right) \\ &= \frac{\omega^2}{c^2}e^{i\beta z}\left(\mathbf{h}_t + \hat{\mathbf{z}}\,h_z\right), \end{aligned} \tag{A.12}$$

Now, Eq. (A.1) implies $\nabla_t^T\varepsilon_{tt}\mathbf{e}_t + \varepsilon_{zz}i\beta e_z = 0$, and the full vectorial eigenvalue equation for the transverse components is obtained of the magnetic field:

$$L\mathbf{h}_t = \left[\nabla_t\nabla_t^T + \eta\varepsilon_{tt}\eta^T\left(\frac{\omega^2}{c^2} - \eta\nabla_t\varepsilon_{zz}^{-1}\nabla_t^T\eta\right)\right]\mathbf{h}_t = \beta^2\mathbf{h}_t, \tag{A.13}$$

firstly appeared in [84]. At this point, we look for the adjoint operator $L^\dagger$, namely $\langle F|LG\rangle = \langle L^\dagger F|G\rangle$, where $F : \mathcal{S} \subset \mathbb{R}^2 \to \mathbb{C}^3$ and $\langle\circ|\circ\rangle$ denotes the usual inner product of square-integrable functions. Attending to the following vectorial identity $\nabla\cdot(a\mathbf{F}) \equiv \nabla^T(a\mathbf{F}) = (\nabla a)\cdot\mathbf{F} + a\nabla^T\mathbf{F}$ and the Gauss theorem, we compute the adjoints of each term of L:

$$\int_{\mathcal{S}} F^*\cdot\nabla_t(\nabla_t^T G)\mathrm{d}S = -\int_{\mathcal{S}}(\nabla_t^T F)^*(\nabla_t^T G)\mathrm{d}S = \int_{\mathcal{S}}(\nabla_t\nabla_t^T F)^*\cdot G, \tag{A.14}$$

$$\begin{aligned}\int_{\mathcal{S}} F^*\cdot\eta\varepsilon_{tt}\eta^T G\mathrm{d}S &= \int_{\mathcal{S}} F_i^*\eta_{ij}(\varepsilon_{tt}\eta^T G)_j\mathrm{d}S \\ &= \int_{\mathcal{S}}(\eta_{ji}^T F_i)^*(\varepsilon_{tt}\eta^T G)_j\mathrm{d}S = \int_{\mathcal{S}}(\eta\varepsilon_{tt}^\dagger\eta^T F)^*\cdot G\mathrm{d}S, \end{aligned} \tag{A.15}$$

where $\epsilon_{tt}^\dagger$ indicates the transpose and complex conjugated of ϵ_{tt}, and

$$\int_{\mathcal{S}} F^*\cdot\eta\varepsilon_{tt}\eta^T\eta\nabla_t\frac{1}{\varepsilon_{zz}}\nabla_t^T\eta G\mathrm{d}S = \int_{\mathcal{S}}(\eta^T\nabla_t\frac{1}{\varepsilon_{zz}^*}\nabla_t^T\eta^T\eta\varepsilon_{tt}^\dagger\eta^T F)^*\cdot G. \tag{A.16}$$

Since the inner product is a linear is each argument separately, the adjoint of L is given by

$$L^\dagger = \nabla_t \nabla_t^T + \eta \varepsilon_{tt}^\dagger \eta^T \frac{\omega^2}{c^2} + \eta \nabla_t \frac{1}{\varepsilon_{zz}^*} \nabla_t^T \varepsilon_{tt}^\dagger \eta^T. \tag{A.17}$$

With this result in mind, and analogously to the above procedure, Eq. (A.9) can be rewritten as follows

$$\begin{aligned} \nabla \times \nabla \times \tilde{\mathbf{E}} &= \nabla \times e^{i\beta z} \left(-\eta \mathbf{e}_t i\beta + \eta \nabla_t e_z + \hat{\mathbf{z}} \nabla_t^T \eta \mathbf{e}_t \right) \\ &= \left(\beta^2 \mathbf{e}_t + i\beta \nabla_t e_z + \eta \nabla_t \nabla_t^T \eta \mathbf{e}_t + \hat{\mathbf{z}} i\beta \nabla_t^T \mathbf{e}_t - \hat{\mathbf{z}} \nabla_t^T \nabla_t e_z \right) e^{i\beta z} \\ &= \frac{\omega^2}{c^2} (\varepsilon_{tt} \mathbf{e}_t + \varepsilon_{zz} e_z \hat{\mathbf{z}}) e^{i\beta z}. \end{aligned} \tag{A.18}$$

Considering again Eq. (A.1), the eigenvalue equation for the transverse electric field is derived:

$$\left[-\eta \nabla_t \nabla_t^T \eta + \frac{\omega^2}{c^2} \varepsilon_{tt} \mathbf{e}_t + \nabla_t \frac{1}{\varepsilon_{zz}} \nabla_t^T \varepsilon_{tt} \right] \mathbf{e}_t = \beta^2 \mathbf{e}_t \tag{A.19}$$

If ε is a symmetric tensor, it is straightforward to conclude

$$L^\dagger \eta \mathbf{e}_t^* = (\beta^2)^* \eta \mathbf{e}_t^*, \tag{A.20}$$

and therefore, $\tilde{\mathbf{h}}_t = \eta \mathbf{e}_t^*$, where $\tilde{\mathbf{h}}_t$ is the so-called dual field of $\mathbf{h}_t$. This fact implies a biorthonormality relation between the eigenvectors of L and $L^\dagger$, when they are properly normalized [85],

$$\langle \tilde{\mathbf{h}}_t^{(i)} | \mathbf{h}_t^{(j)} \rangle = \int_{\mathcal{S}} (\mathbf{e}_t^{(i)} \times \mathbf{h}_t^{(j)}) \cdot \hat{\mathbf{z}} \, \mathrm{d}S = \delta_{ij}. \tag{A.21}$$

We emphasize Eqs, (A.13) and (A.19) do not require a symmetric ε. However, the biorthogonality between $\mathbf{h}_t$ and $\eta \mathbf{e}_t^*$ is satisfied under this assumption. This result will be key to develop our inverse linear design tools.

In addition, the nonlinear pulse propagation equation will also take advantage of the following property:

$$\begin{aligned} \mu_0 \int_{\mathcal{V}} \tilde{\mathbf{H}}^* \cdot \tilde{\mathbf{H}} \, \mathrm{d}V &= \mu_0 \int_{\mathcal{V}} \tilde{\mathbf{H}}^* \cdot \frac{1}{i\omega\mu_0} \nabla \times \tilde{\mathbf{E}} \, \mathrm{d}V \\ &= \int_{\mathcal{V}} \frac{1}{i\omega} (\nabla \times \tilde{\mathbf{H}}^*) \cdot \tilde{\mathbf{E}} \, \mathrm{d}V = \int_{\mathcal{V}} \frac{1}{i\omega} (-i\omega\varepsilon_0 \varepsilon \tilde{\mathbf{E}})^* \cdot \tilde{\mathbf{E}} \, \mathrm{d}V \\ &= \int_{\mathcal{V}} (\varepsilon_0 \varepsilon \tilde{\mathbf{E}})^* \cdot \tilde{\mathbf{E}} \, \mathrm{d}V = \varepsilon_0 \int_{\mathcal{V}} \tilde{\mathbf{E}}^* \cdot \varepsilon \tilde{\mathbf{E}} \, \mathrm{d}V, \end{aligned} \tag{A.22}$$

where we have used Eqs. (A.3) and (A.4) and we have assumed $\varepsilon = \varepsilon^{\dagger}$. Note that this last condition is equivalent to $\varepsilon = \varepsilon^{T}$, if lossless media are considered as we will assume to derive the nonlinear propagation equation. It indicates that the electric and magnetic field stores the same amount of energy [86]. Furthermore, if we consider Eq. (A.6) and (A.7) and introduce them on Eq. (A.22), it is obtained

$$\int_{-\infty}^{+\infty} e^{i\beta z} \left[\int_{\mathcal{S}} (\mu_0 \mathbf{h}^* \cdot \mathbf{h} - \varepsilon_0 \mathbf{e}^* \cdot \varepsilon \mathbf{e}) \, \mathrm{d}S \right] \mathrm{d}z = 0, \tag{A.23}$$

which implies

$$\mu_0 \int_{\mathcal{S}} \mathbf{h}^* \cdot \mathbf{h} \, \mathrm{d}S = \varepsilon_0 \int_{\mathcal{S}} \mathbf{e}^* \cdot \varepsilon \mathbf{e} \, \mathrm{d}S. \tag{A.24}$$

We want to emphasize the most important results derived in this appendix. Eq. (A.13) is the starting point of Paper IV. Equation (A.21) allows to obtain the main result of Paper IV, *i.e.*, a close expression for the derivatives with respect any geometrical parameters of β. In addition, we attend to this equation together with Eq. (A.24) to derive the GNLSE in Chapter 2.

Appendix B

List of acronyms

SOI : Silicon-on-insulator

GNLSE : Generalized nonlinear Schrödinger equation

SC : Supercontinuum

GVD : Group-velocity dispersion

SPM : Self-phase modulation

TPA : Two-photon absorption

FWM : Four-wave mixing

OWB : Optical wave-breaking

MI : Modulation instability

SVEA : Slowly-varying envelope approximation

TSFG : Third order sum-frequency generation

THG : Third harmonic generation

TM : Transverse magnetic

FCA : Free carrier absorption

FCD : Free carrier dispersion

References

[1] B. Jalali, "Can silicon change photonics?" Phys. Stat. Sol.(a) **205**, 213–224 (2008).

[2] V. E. Zakharov and A. B. Shabat,"Exact theory of two-dimensional self-focusing and one-dimensional self-modulation of waves in nonlinear media", Soviet Physics JETP **34**, 62–70 (1972).

[3] M. Conforti and S. Trillo, "Dispersive wave emission from wave breaking", Opt. Lett. **38**, 3815–3818 (2013).

[4] D. V. Skryabin and A. V. Yulin, "Theory of generation of new frequencies by mixing of solitons and dispersive waves in optical fibers", Phys. Rev. E **72**, 016619 (2005).

[5] D. V. Skryabin and A. V. Gorbach, "Colloquium: Looking at a soliton through the prism of optical supercontinuum", Rev. Mod. Phys. **82**, 1287–1299 (2010).

[6] J. M. Dudley, G. Genty, and S. Coen, "Supercontinuum generation in photonic crystal fiber", Rev. Mod. Phys. **78**, 1135–1184 (2006).

[7] A. C. Turner, C. Manolatou, B. S. Schmidt, M. Lipson, M. A. Foster, J. E. Sharping, and A. L. Gaeta, "Tailored anomalous group-velocity dispersion in silicon channel waveguides", Opt. Express **14**, 4357–4362 (2006).

[8] S. Mas, J. Caraquitena, J. V. Galán, P. Sanchis, and J. Martí, "Tailoring the dispersion behavior of silicon nanophotonic slot waveguides", Opt. Express **18**, 20839–20844 (2010).

[9] L. Zhang, Y. Yue, R. G. Beausoleil, and A. E. Willner, "Flattened dispersion in silicon slot waveguides", Opt. Express **18**, 20529–20534 (2010).

[10] L. Zhang, Q. Lin, Y. Yue, Y. Yan, R. G. Beausoleil, and A. E. Willner, "Silicon waveguide with four zero-dispersion wavelengths and its application in on-chip octave-spanning supercontinuum generation", Opt. Express **20**, 1685–1690 (2012).

[11] E. Silvestre, T. Pinheiro-Ortega, P. Andrés, J. J. Miret, and A. Coves, "Differential toolbox to shape dispersion behavior in photonic crystal fibers", Opt. Lett. **31**, 1190–1192 (2006).

[12] J. D. Jackson, *Classical Electrodynamics*, (John Wiley & Sons, 3rd Ed., 1998).

[13] G. P. Agrawal, *Nonlinear Fiber Optics* (Academic Press, 4th Ed., 2007).

[14] R. W. Boyd, *Nonlinear Optics* (Academic Press, 3rd Ed., 2007).

[15] L. Mandel, "Interpretation of instantaneous frequencies", Am. J. Phys. **42**, 840–846 (1974).

[16] B. Boashash, "Estimating and Interpreting The Instantaneous Frequency of a Signal-Part 1: Fundamentals", Proceeding of the IEEE **80**, 520–538 (1992).

[17] P. J. Loughlin and B. Tacer, "Comments on the interpretation of the instantaneous frequency", IEEE Signal Processing Lett. *4*, 123–125 (1997).

[18] L. Cohen, *Time-Frequency Analysis* (Prentice Hall, 1995).

[19] F. Shimizu,"Frequency broadening in liquid by a short light pulse", Phys. Rev. Lett. **19**, 1097–1100 (1967).

[20] P. N. Butcher and D. Cotter, *The elements of nonlinear optics* (Cambridge University Press, 1990).

[21] J. Botineau and R. H. Stolen, "Effect of polarization on spectral broadening in optical fibers", J. Opt. Soc. Am. **72**, 1592–1596 (1982).

[22] M. Erkintalo, Y. Q. Xu, S. G. Murdoch, J. M. Dudley, and G. Genty, "Cascaded Phase Matching and Nonlinear Symmetry Breaking in Fiber Frequency Combs", Phys. Rev. Lett. **109**, 223904 (2012).

[23] W. J. Tomlinson, R. H. Stolen, and A. M. Johnson,"Optical wavebreaking in nonlinear optical fibers", Opt. Lett. **10**, 457-459 (1985).

[24] J. E. Rothenberg and D. Grischkowsky, "Observation of the formation of an optical intensity shock and wave breaking in the nonlinear propagation of Pulses in optical fibers", Phys. Rev. Lett. **62**, 531–534 (1989).

[25] J. E. Rothenberg, "Femtosecond optical shocks and wave breaking in fiber propagation", J. Opt. Soc. Am. B **6**, 2392–2401 (1989).

[26] D. Anderson, M. Desaix, M. Lisak, and M. L. Quiroga-Teixeiro, "Wave breaking in nonlinear-optical fibers", J. Opt. Soc. Am. B **9**, 1358–1361 (1992).

[27] D. Anderson, M. Desaix, M. Karlsson, M. Lisak, and M. L. Quiroga-Teixeiro, "Wave-breaking-free pulses in nonlinear-optical fibers", J. Opt. Soc. Am. B **10**, 1185–1190 (1993).

[28] C. Finot, B. Kibler, L. Provost, and S. Wabnitz, "Beneficial impact of wave-breaking for coherent continuum formation in normally dispersive nonlinear fibers", J. Opt. Soc. Am. B **25**, 1938–1948 (2008).

[29] A. M. Heidt, A. Hartung, G. W. Bosman, P. Krok, E. G. Rohwer, H. Schwoerer, and H. Bartelt,"Coherent octave spanning near-infrared and visible supercontinuum generation in all-normal dispersion photonic crystal fibers", Opt. Express **19**, 3775–3787 (2011).

[30] Y. Liu, H. Tu, and S. A. Boppart, "Wave-breaking-extended fiber supercontinuum generation for high compression ratio transform-limited pulse compression", Opt. Lett. **37**, 2172-2174 (2012).

[31] Y. Kodama and A. Hasegawa, "Nonlinear pulse propagation in a monomode dielectric guide", J. Quantum Electron. **23**, 510–524 (1987).

[32] P. K. A. Wai, C. R. Menyuk, Y. C. Lee, and H. H. Chen, "Nonlinear pulse propagation in the neighborhood of the zero-dispersion wavelength of monomode optical fibers", Opt. Lett. **11**, 464–466 (1986).

[33] P. K. A. Wai, H. H. Chen, and Y. C. Lee, "Radiation by solitons at the zero group-dispersion wavelength of single-mode optical fibers", Phys. Rev. A **41**, 426–439 (1991).

[34] N. Akhmediev and M. Karlsson, "Cherenkov radiation emitted by solitons in optical fibers", Phys. Rev. A **51**, 2602–20607 (1995).

[35] J. P. Gordon, "Theory of the soliton self-frequency shift", Opt. Lett. **11** 662–664 (1986).

[36] L. Yin and G. P. Agrawal, "Impact of two-photon absorption on self-phase modulation in silicon waveguides", Opt. Lett. **32**, 2031–2033 (2007).

[37] P. Koonath, D. R. Solli, and B. Jalali, "Limiting nature of continuum generation in silicon", Appl. Phys. Lett. **93**, 091114 (2008).

[38] Q. Lin, O. J. Painter, and G. P. Agrawal, "Nonlinear optical phenomena in silicon waveguides: Modeling and applications", Opt. Express **15**, 16604–16644 (2007).

[39] B. Jalali, "Nonlinear optics in the mid-infrared", Nature Photon. **4**, 506–508 (2010).

[40] R. Claps, D. Dimitropoulos, V. Raghunathan, Y. Han, and B. Jalali, "Observation of stimulated Raman amplification in silicon waveguides", Opt. Express **11**, 1731–1739 (2003).

[41] L. Yin, Q. Lin, and G. P. Agrawal, "Soliton fission and supercontinuum generation in silicon waveguides", Opt. Lett. **32**, 391–393 (2007).

[42] P. Kinsler, "Limits of the unidirectional pulse propagation approximation", J. Opt. Soc. Am. B **24**, 2363–2368 (2007).

[43] Y. R. Shen, *The principles of nonlinear optics* (John Wiley & Sons, 3rd Ed., 1984).

[44] A. Ferrando, M. Zacarés, P. F. de Córdoba, D. Binosi, and Á. Montero, "Forward-backward equations for nonlinear propagation in axially invariant optica systems", Phys. Rev. E **71**, 016601 (2005).

[45] P. Kinsler, S. B. P. Radnor, and G. H. C. New, "Theory of directional pulse propagation", Phys. Rev. A **72**, 063807 (2005).

[46] T. Brabec and F. Krausz, "Nonlinear optical pulse propagation in the single-cycle regime", Phys. Rev. Lett. **78**, 3282–3285 (1997).

[47] M. Kolesik, J. V. Moloney, and M. Mlejnek, "Unidirectional optical pulse propagation equation", Phys. Rev. Lett **89**, 283902 (2002).

[48] B. A. Daniel and G. P. Agrawal, "Vectorial nonlinear propagation in silicon nanowire waveguides: polarization effects", J. Opt. Soc. Am. B **27**, 956–965 (2010).

[49] A. W. Snyder and J. D. Love, *Optical Waveguide Theory* (Chapman & Hall, London, 1983).

[50] M. Kolesik, E. M. Wright, and J. V. Moloney, "Simulation of femtosecond pulse propagation in sub-micron diameter tapered fibers", Appl. Phys. B **79**, 293-300 (2004).

[51] M. Kolesik and J. V. Moloney, "Nonlinear optical pulse propagation simulation: From Maxwell's to unidirectional equations", **70**, 036604 (2004).

[52] S. Afshar V. and T. M. Monro, "A full vectorial model for pulse propagation in emerging waveguides with subwavelength structures. Part I: Kerr nonlinearity", Opt Express **17**, 2298–2318 (2009).

[53] R. M. Osgood, Jr., N. C. Panoiu, J. I. Dadap, X. Liu, X. Chen, I-W. Hsieh, E. Dulkeith, W. M. J. Green, and Y. A. Vlasov, "Engineering nonlinearities in nanoscale optical systems: physics and applications in dispersion-engineered silicon nanophotonic wires", Adv. Opt. Photon. **1**, 162–235 (2009).

[54] P. L. François, "Nonlinear propagation of ultrashort pulses in optical fibers: total field formulation in the frequency domain", J. Opt. Soc. Am. B **8**, 276–293 (1991).

[55] K. J. Blow and D. Wood, "Theoretical description of transient stimulated Raman scattering in optical fibers", J. Quantum Electron. **25**, 2665–2673 (1989).

[56] E. Rubino, J. McLenaghan, S. C. Kehr, F. Belgiorno, D. Townsend, S. Rohr, C. E. Kuklewicz, U. Leonhardt, F. Konig, and D. Faccio, "Negative-frequency resonant radiation", Phys. Rev. Lett. **108**, 253901 (2012).

[57] M. Conforti, A. Marini, D. Faccio, and F. Biancalana, "Negative frequencies get real: a missing puzzle piece in nonlinear optics", *arXiv*:1305.5264 (2013).

[58] J. Lægsgaard, "Mode profile dispersion in the generalized nonlinear Schrödinger equation", Opt. Express **15** 16110–16123 (2007).

[59] T. X. Tran and F. Biancalana, "An accurate envelope equation for light propagation in photonic nanowires: new nonlinear effects", Opt. Express **17**, 17934–17949 (2009).

[60] X. Zhao, A. V. Gorbach, and D. V. Skryabin, "Dispersion of nonlinearity in subwavelength waveguides: derivation of pulse propagation equation and frequency conversion effects", J. Opt. Soc. Am. B **30**, 812–820 (2013).

[61] F. Poletti and P. Horak, "Description of ultrashort pulse propagation in multimode optical fibers", J. Opt. Soc. Am. B **25**, 1645–1654 (2008).

[62] C. Pask and A. Vatarescu, "Spectral approach to pulse propagation in a dispersive nonlinear medium", J. Opt. Soc. Am. B **3**, 1018–1024 (1986).

[63] D. Farnesi, A. Barucci, C. Righini, S. Berneschi, S. Soria, and G. Nunzi Conti, "Optical frequency conversion in silica-whispering-gallery-mode microspherical resonators", Phys. Rev. Lett. **112**, 093901 (2014).

[64] J. Kim, Q-H. Park, H. J. Shin, "Conservation laws in higher-order nonlinear Schrodinger equations", Phys. Rev. E **58**, 6746–6751 (1998).

[65] V. E. Zakharov, E. A. Kuznetsov, "Optical solitons and quasisolitons", J. Exp. Theor. Phys. **86**, 1035–1046 (1998).

[66] V. I. Karpman, A. G. Shagalov, "Stability of solitons described by nonlinear Schrödinger-type equations with higher-order dispersion", Physica D **144** 194–210 (2000).

[67] B. Barviau, B. Kibler, and A. Picozzi, "Wave-turbulence approach of supercontinuum generation: Influence of self-steepening and higher-order dispersion", Phys. Rev. A **79**, 063840 (2009).

[68] C. Michel, P. Suret, S. Randoux, H. R. Jauslin, and A. Picozzi, "Influence of third-order dispersion on the propagation of incoherent light in optical fibers", Opt. Lett. **35**, 2367–2369 (2010).

[69] M. Lipson, "Guiding, modulating, and emitting light on silicon–Challengges and opportunities", J. Lightw. Technol. **23**, 4222–4238 (2005).

[70] B. Jalali and S. Fathpour, "Silicon photonics", J. Lightw. Technol. **24**, 4600–4615 (2006).

[71] A. Ferrando, E. Silvestre, P. Andrés, J. J. Miret, and M. V. Andrés, "Designing the properties of dispersion-flattened photonic crystal fibers", Opt. Express **9**, 687–697 (2001).

[72] V. R. Almeida, Q. Xu, C. A. Barrios, and M. Lipson, "Guiding and confining light in void nanostructure", Opt. Lett. **29**, 1209–1211 (2004).

[73] Q. Xu, V. R. Almeida, R. R. Panepucci, and M. Lipson, "Experimental demonstration of guiding and confining light in nanometer-size low-refractive-index material", Opt. Lett **29**, 1626–1628 (2004).

[74] M. Dinu, F. Quochi, and H. Garcia, "Third-order nonlinearities in silicon at telecom wavelengths", Appl. Phys. Lett. **82**, 2954–2956 (2003).

[75] Q. Lin, J. Zhang, G. Piredda, R. W. Boyd, P. M. Fauchet, and G. P. Agrawal, "Dispersion of silicon nonlinearities in the near infrared region", Appl. Phys. Lett. **91**, 021111 (2007).

[76] A. D. Bristow, N. Rotenberg, and H. M. van Driel, "Two-photon absorption and Kerr coefficients of silicon for 850– 2200 nm", Appl. Phys. Lett. **90**, 191104 (2007).

[77] V. P. Tzolov, M. Fontaine, N. Godbout and S. Lacroix, "Nonlinear self-phase-modulation effects: a vectorial first-order perturbation approach", Opt. Lett. **20**, 456–458 (1995).

[78] S. G. Johnson and J. D. Joannopoulos, "Block-iterative frequency-domain methods for Maxwell's equations in a planewave basis", Opt. Express **8**, 173–190 (2001).

[79] D. E. Aspnes, "Local-field effects and effective-medium theory: a microscopic perspective", Am. J. Phys. **50**, 704–709 (1982).

[80] J. J. Miret, E. Silvestre, and P. Andrés, "Octave-spanning ultraflat supercontinuum with soft-glass photonic crystal fibers", Opt. Express **17**, 9197–9203 (2009).

[81] J. S. Levy, A. Gondarenko, M. A. Foster, A. C. Turner-Foster, A. L. Gaeta, and M. Lipson, "CMOS-compatible multiwavelength oscillator for on-chip optical interconnects", Nature Photon. **4**, 37–40 (2010).

[82] F. Ferdous, H. X Miao, D. E. Leaird, K. Srinivasan, J. Wang, L. Chen, L. T. Varghese, and A. M. Weiner, "Spectral line-by-line pulse shaping of on-chip microresonator frequency combs", Nature Photon. **5**, 770–776 (2011).

[83] S. Coen and M. Erkintalo, "Universal scaling laws of Kerr frequency combs", Opt. Lett. **38**, 1790–1792 (2013).

[84] E. Silvestre, T. Pinheiro-Ortega, P. Andrés, J. J. Miret, and A. Ortigosa-Blanch, "Analytical evaluation of chromatic dispersion in photonic crystal fibers", Opt. Lett. **30**, 453–455 (2005).

[85] E. Silvestre, M. V. Andrés, and P. Andrés, "Biorthonormal-basis method for the vector description of optical-fiber modes", J. Lightwave Technol. **16**, 923–928 (1998).

[86] J. D. Joannopoulos, S. G. Johnson, J. N. Winn, and R. D. Meade, *Photonic crystals. Molding the flow of light*, 2nd Ed., (Princeton University Press, 2008).

Papers I–V

Paper I

Spectral broadening enhancement in silicon waveguides through pulse shaping

D. Castelló-Lurbe, E. Silvestre, P. Andrés,
and V. Torres-Company

in *Optics Letters*, Vol. 37, No. 13, pp. 2757–2759, July 2012.

Spectral broadening enhancement in silicon waveguides through pulse shaping

David Castelló-Lurbe,[1,*] Enrique Silvestre,[1] Pedro Andrés,[1] and Víctor Torres-Company[2,3]

[1]*Departament d'Òptica, Universitat de València, 46100 Burjassot, Spain*

[2]*School of Electrical and Computer Engineering, Purdue University, West Lafayette, Indiana 47907, USA*

[3]*Departament de Física, Universitat Jaume I, 12071 Castelló, Spain*

**Corresponding author: david.castello-lurbe@uv.es*

Received February 6, 2012; revised May 2, 2012; accepted May 4, 2012;
posted May 11, 2012 (Doc. ID 162636); published June 29, 2012

Spectral broadening in silicon waveguides is usually inhibited at telecom wavelengths due to some adverse effects related to semiconductor dynamics, namely, two-photon and free-carrier absorption (FCA). In this Letter, our numerical simulations show that it is possible to achieve a significant enhancement in spectral broadening when we properly preshape the input pulse to reduce the impact of FCA on spectral broadening. Our analysis suggests that the use of input pulses with the correct skewness and power level is crucial for this achievement. © 2012 Optical Society of America

OCIS codes: 130.4310, 190.4360, 190.4390.

Nowadays, continuous advances in nanophotonics technologies have spurred on interest in the study of silicon-based optical materials [1]. Strong confinement of light in nanoengineered silicon-on-insulator (SOI) waveguides results in a huge effective nonlinearity and the ability for dispersion engineering (see, e.g., [2,3]). These achievements have opened up the possibility of performing previously demonstrated signal processing functionalities (mainly based in nonlinear kilometric fibers) at chip scale with relatively low optical power [4]. These Si-based components offer the benefits of low cost (complementary metal-oxide-semiconductor–compatible large-scale-fabrication processes) and low power consumption.

However, at the relevant wavelength region around 1.5 μm, Kerr-based spectral broadening or self-phase modulation (SPM) is accompanied by an orchestra of different nonlinear phenomena arising from the semiconductor carrier dynamics [5–7]. Specifically we mention the absorption and dispersion of free carriers produced by two-photon absorption (TPA), which are not present in conventional silica-based devices. The net effect results in a depletion of the achievable spectral broadening for a Gaussian input pulse in comparison with the case when only SPM is acting [8–10].

Additionally, the phenomenon under study is extremely sensitive to the input pulse characteristics due to the inherent nonlinear nature of the spectral broadening. In fact, up to some extent, pulse shaping techniques have demonstrated to be effective in controlling the nonlinear broadening in photonic crystal fibers [11,12] and other nonlinear materials [13–15], using both single-pass [15] and self-learning adaptive configurations [11–14]. Besides, these techniques offer valuable insight in understanding the pulse dynamics through propagation [11,16]. In this Letter, we show that the proper manipulation of the pulse phase enhances spectral broadening even in the presence of TPA and free-carrier absorption (FCA).

Let us remind the reader that the dynamics of an optical pulse propagating in an SOI nanowaveguide can be described in mathematical terms by [9]

$$\partial_z A + i\frac{\beta_2}{2}\partial_t^2 A = i\gamma_0(1+ir)|A|^2A - \frac{\sigma}{2}(1+i\mu)N_cA - \frac{\alpha_l}{2}A, \tag{1}$$

$$N_c(z,t) = \frac{\beta_{\mathrm{TPA}}}{2h\nu_0 A_{\mathrm{eff}}^2}\int_{-\infty}^{t} e^{\frac{-t-t'}{\tau_c}}|A(z,t')|^4\mathrm{d}t', \tag{2}$$

where A is the electric-field envelope, ν_0 represents the carrier frequency, β_2 stands for the group velocity dispersion (GVD) parameter, n_2 is the Kerr coefficient, A_{eff} is the effective area of the waveguide, γ_0 denotes the nonlinear coefficient of the waveguide defined as $\gamma_0 = n_2 2\pi\nu_0/cA_{\mathrm{eff}}$, σ is the FCA coefficient, α_l the linear loss coefficient, N_c corresponds to the carrier density, β_{TPA} is the TPA coefficient, τ_c represents the carrier lifetime, and the dimensionless parameters $r = \beta_{\mathrm{TPA}}c/4\pi n_2\nu_0$ and μ account for the relative weight of TPA and free-carrier dispersion (FCD), respectively. As in previously published results [9], we consider $\lambda_0 = 1.55$ μm, α_l corresponding to 1 dB/cm, $n_2 \approx 6\times10^{-18}$ m^2/W, $\beta_{\mathrm{TPA}} = 5\times10^{-12}$ m/W, $\sigma = 1.45\times10^{-21}$ m^2, $r = 0.1$, $\mu = 7.5$, and $\tau_c = 1$ ns. Likewise, in our numerical simulations we choose $A_{\mathrm{eff}} \approx 1$ μm^2. Because we focus our attention on the interplay between SPM and carrier effects, we consider quite long pulses for which the GVD term in Eq. (1) shall be neglected in the following.

In order to analyze in a qualitative way the spectral broadening, it is very useful to study the instantaneous frequency of the propagated complex field. With this aim, let us explicitly consider the phase of the complex field envelope, $A = |A|\exp(i\phi)$. By defining the effective z-dependent loss coefficient and length, $\alpha_{\mathrm{eff}} = \alpha_l + \sigma N_c$ and $z_{\mathrm{eff}} = \int_0^z \exp(-\int_0^{z'}\alpha_{\mathrm{eff}}\mathrm{d}z'')\mathrm{d}z'$, respectively, the following key equations are derived in an analogous way to Eq. (60) in [6]:

$$\partial_z(-\partial_t\phi) = -\gamma_0\partial_t|A|^2 + \frac{\sigma\mu}{2}\left(\frac{\beta_{\mathrm{TPA}}}{2h\nu_0A_{\mathrm{eff}}^2}|A|^4 - \frac{N_c}{\tau_c}\right), \tag{3}$$

0146-9592/12/132757-03$15.00/0

$$|A|^2 = \frac{\exp\left(-\int_0^z \alpha_{\text{eff}} dz'\right) A_0^2}{1 + 2\gamma_0 r z_{\text{eff}} A_0^2}, \tag{4}$$

where $A_0 = |A(0,t)|$.

Despite their complexity, it is possible to get some valuable physical insight from the above equations. From Eq. (3), we note that the evolution of the instantaneous frequency is governed by two processes. The first term of the right-hand side corresponds to SPM, whereas the second one takes into account FCD. For low repetition-rate pulses and if the input pulse width $T_0 \ll \tau_c$, the subterm proportional to $-N_c/\tau_c$ can be neglected [9], and hence the FCD term can be considered always positive. Accordingly, FCD only produces blueshifted components; by contrast SPM can give rise to both blueshifted and redshifted ones [9,10]. Finally, similarly to [6], we define the threshold power $P_{\text{th}} = 8\gamma_0 h\nu_0 A_{\text{eff}}^2/T_0\sigma\mu\beta_{\text{TPA}}$, beyond which the FCD contribution exceeds that of SPM.

Having in mind the above facts, we realize that an asymmetric input pulse induces two concomitant effects. On one hand, the longer wavelength production due to SPM is improved by means of a skew input pulse with positive sign due to the enhanced slope on the leading edge of the pulse. On the other hand, if the peak power $P_0 \gg P_{\text{th}}$, the shorter wavelengths are generated earlier in time, near to the peak power. According to Eq. (2), the production of free carriers is a cumulative effect, and hence, as one can see in Eq. (4), FCA highly affects the trailing edge of the pulse. So, losses induced by FCA could be partially compensated by generating blueshifted frequencies so fast that the free carriers did not have time to accumulate. Moreover, a positive skewness of the pulse profile would strengthen this beneficial effect. Thus, both longer and shorter wavelength enhancement could be feasible using positive skew pulses.

To prove the above ideas, we solve the previous equations considering two kinds of skew input pulses produced by adding a certain spectral phase to a Gaussian pulse (hence preserving its bandwidth and energy). Both cases could be experimentally implemented in a feasible way by means of a pulse shaper with good spectral resolution. First we consider a spectral phase of the form $\eta(\omega - \omega_0)^3$, where η denotes the strength of the skewness. The negative η sign guarantees the right skewness of the temporal pulse profile.

We have solved numerically Eqs. (1) and (2) and computed the achieved spectral width at −20 dB for different values of the η parameter. In this calculation, we consider $T_0 = 10$ ps and a 1 cm long silicon waveguide. The results are shown in Fig. 1 and support our explanation. The maximum broadening is achieved at $\eta = -125$ ps^3 for 100 W and $\eta = -124$ ps^3 for 1 kW (peak powers are referred to the unmodulated Gaussian pulse in both cases, unshaped and shaped). Only the SPM effect is working at 10 W, and, therefore, no significant improvement of the spectral broadening is observed. Note that, in our numerical example, P_{th} is about 50 W. When we increase the input power up to 100 W [see Fig. 2(a)], the SPM production of low frequencies is intensified by the pulse asymmetry. In addition, the upper part of the spectrum remains unaffected. Here the FCA changes induced

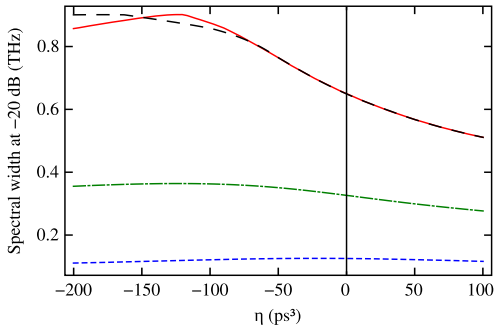

Fig. 1. (Color online) Spectral output width at −20 dB as a function of the strength η of the cubic-phase modulation for three input peak powers: 10 W (short-dashed curve), 100 W (dotted–dashed curve), and 1 kW (solid curve). The long-dashed curve corresponds to the input spectral phase provided by the Gerchberg–Saxton (GS) algorithm (see details in the text).

by pulse shaping do not provide an enhancement of higher frequencies because of the reduction on blueshifted components produced by SPM due to the smooth tail of the asymmetric pulse. At higher (but realistic; see [10]) powers, a notable enhancement appears at both sides of the spectrum since FCA plays a less significant role thanks to the pulse shape. The expected output spectrum is depicted in Fig. 2(b). In this case, it is even up to 40% broader with respect to the unshaped case (measured at the −20 dB level).

Finally, we stress the connection between reducing FCA and spectral broadening by computing N_c at the instant when the maximum of the output pulse occurs; see Fig. 3(a). It is worth noting that the spectral width reduction shown by the curve corresponding to $P_0 = 1$ kW in

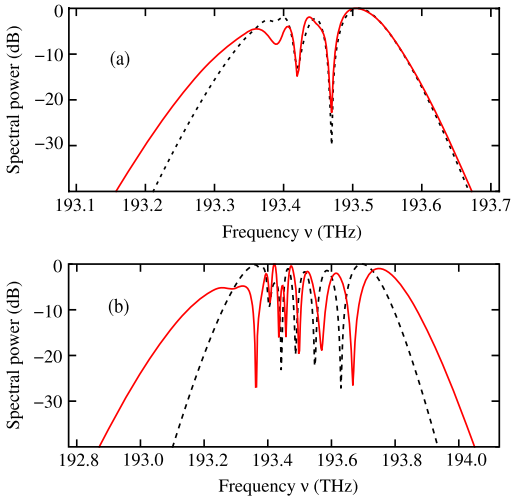

Fig. 2. (Color online) Comparison of the output power spectrum between the unmodulated Gaussian input pulse (dashed curve) and the spectrally chirped version (solid curve) for (a) $P_0 = 100$ W, $\eta = -125$ ps^3 and (b) $P_0 = 1$ kW, $\eta = -124$ ps^3.

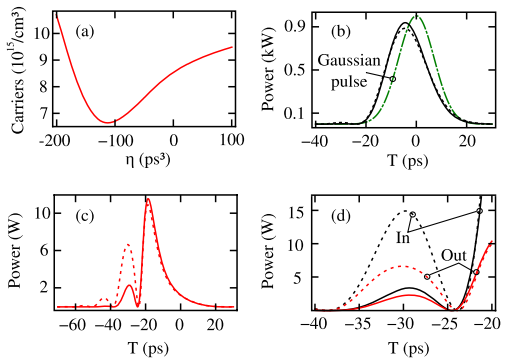

Fig. 3. (Color online) (a) Density of carriers at the maximum of the output pulse in terms of η; (b) input pulses; (c) output pulses. In both plots (b) and (c), dashed curves correspond to pulses resulting from the cubic-phase modulation and solid curves refer to pulses resulting from the GS algorithm. In all cases, $\eta = -200$ ps^3 and $P_0 = 1$ kW. (d) Secondary lobes of the modulated pulses of (b) and (c).

Fig. 1 is consistent with the increase of N_c for lower values of η. Moreover, we link this feature with the oscillatory structure that appears near the leading edge of the input pulse due to the cubic spectral phase used to obtain skew input pulses in these cases; see Figs. 3(b)–3(d). These secondary lobes generate additional carriers that enhance FCA where the production of new frequencies is concentrated.

Note that, for greater values of positive skewness, the pulse shows bigger ripples before the main lobe. In order to confirm this assumption, with the aid of the GS algorithm [17], we search for spectral phases that preserve the shape of the main lobe of the pulses shaped through a cubic spectral phase. Accordingly, for the different values of the η parameter considered previously, we take $\eta(\omega - \omega_0)^3$ as our seed phase (this choice accelerates the convergence of the algorithm) and set our target as the main lobe of the corresponding η-skew pulse (i.e., the above referred oscillations of the preshaped pulses are eliminated to construct the targets). Every GS solution is labeled with the η value of the corresponding seed phase. According to Figs. 3(c) and 3(d), the GS technique provides a reduction of the satellite lobes but not their total suppression. The resulting spectral behavior shown in Fig. 1 confirms the pernicious effect of the secondary lobes when input pulses present sufficient skewness.

In summary, we have shown that the skewness introduced on a Gaussian input pulse of high enough peak power leads to an spectral broadening enhancement on SOI waveguides. The key point is to enhance longer wavelength production due to SPM by increasing the leading slope edge which simultaneously decreases FCA effects on shorter wavelength production. Although in this work we do not take into account dispersive phenomena, our physical interpretation suggests that the current achievements can also be extended to this case.

This work was financially supported by the Plan Nacional Investigación, Desarrollo e Innovación (I+D +I) under the research project TEC2008-05490, by Ministerio de Ciencia e Innovación (Spain), and by the Generalitat Valenciana under the grant PROMETEO 2009-077. One of the authors, D. C.-L., gratefully acknowledges funding from the Generalitat Valenciana (VALi+d predoctoral contract). V. T.-C. gratefully acknowledges funding from a Marie Curie International Outgoing Fellowship (project PIOF-2009-234996).

References

1. B. Jalali and S. Fathpour, J. Lightwave Technol. **24**, 4600 (2006).
2. A. C. Turner-Foster, M. A. Foster, R. Salem, A. L. Gaeta, and M. Lipson, Opt. Express **18**, 1904 (2010).
3. L. Zhang, Y. Yue, R. G. Beausoleil, and A. E. Willner, Opt. Express **19**, 8102 (2011).
4. J. Leuthold, C. Koos, and W. Freude, Nat. Photon. **4**, 535 (2010).
5. Ö. Boyraz, P. Koonath, V. Raghunathan, and B. Jalali, Opt. Express **12**, 4094 (2004).
6. Q. Lin, O. J. Painter, and G. P. Agrawal, Opt. Express **15**, 16604 (2007).
7. R. M. Osgood, Jr., N. C. Panoiu, J. I. Dadap, X. Liu, X. Chen, I.-W Hsieh, E. Dulkeith, W. M. Green, and Y. A. Vlasov, Adv. Opt. Photon. **1**, 162 (2009).
8. E. Dulkeith, Y. A. Vlasov, X. Cheng, N. C. Panoiu, and R. M. Osgood, Jr., Opt. Express **14**, 5524 (2006).
9. L. Yin and G. P. Agrawal, Opt. Lett. **32**, 2031 (2007).
10. P. Koonath, D. R. Solli, and B. Jalali, Appl. Phys. Lett. **93**, 091114 (2008).
11. S. Xu, D. H. Reitze, and R. S. Windeler, Opt. Express **12**, 4731 (2004).
12. D. Lorenc, D. Velic, A. N. Markevitch, and R. J. Levis, Opt. Commun. **276**, 288 (2007).
13. F. G. Omenetto, A. J. Taylor, M. D. Moores, and D. H. Reitze, Opt. Lett. **26**, 938 (2001).
14. D. Schumacher, Opt. Lett. **27**, 451 (2002).
15. X. Yang, D. J. Richardson, and P. Petropoulos, in *CLEO/Europe and EQEC 2011 Conference Digest*, OSA Technical Digest (CD) (Optical Society of America, 2011), CI2_1.
16. C. Ament, P. Polynkin, and J. V. Moloney, Phys. Rev. Lett. **107**, 243901 (2011).
17. A. Rundquist, A. Efimov, and D. H. Reitze, J. Opt. Soc. Am. B **19**, 2468 (2002).

Paper II

Dispersion-to-spectrum mapping in nonlinear fibers based on optical wave-breaking

D. Castelló-Lurbe, P. Andrés, and E. Silvestre

in *Optics Express*, Vol. 21, No. 23, pp. 28550–28558, November 2013.

Dispersion-to-spectrum mapping in nonlinear fibers based on optical wave-breaking

David Castelló-Lurbe,* Pedro Andrés, and Enrique Silvestre

Departament d'Òptica, Universitat de València, 46100 Burjassot, Spain

*david.castello-lurbe@uv.es

Abstract: In this work we recognize new strategies involving optical wave-breaking for controlling the output pulse spectrum in nonlinear fibers. To this end, first we obtain a constant of motion for nonlinear pulse propagation in waveguides derived from the generalized nonlinear Schrödinger equation. In a second phase, using the above conservation law we theoretically analyze how to transfer in a simple manner the group-velocity-dispersion curve of the waveguide to the output spectral profile of pulsed light. Finally, the computation of several output spectra corroborates our proposition.

OCIS codes: (190.4370) Nonlinear optics: fibers; (190.4380) Nonlinear optics: four-wave mixing; (190.5530) Pulse propagation and temporal solitons; (060.4005) Microstructured fibers; (320.7110) Ultrafast nonlinear optics.

References and links

1. W. J. Tomlinson, R. H. Stolen, and A. M. Johnson, "Optical wave-breaking in nonlinear optical fibers," Opt. Lett. **10**, 457–459 (1985).
2. D. Anderson, M. Desaix, M. Lisak, and M. L. Quiroga-Teixeiro, "Wave breaking in nonlinear-optical fibers," J. Opt. Soc. Am. B **9**, 1358–1361 (1992).
3. G. P. Agrawal, *Nonlinear Fiber Optics*, 4th ed. (Academic, 2007).
4. D. Anderson, M. Desaix, M. Karlsson, M. Lisak, and M. L. Quiroga-Teixeiro, "Wave-breaking-free pulses in nonlinear-optical fibers," J. Opt. Soc. Am. B **10**, 1185–1190 (1993).
5. C. Finot, B. Kibler, L. Provost, and S. Wabnitz, "Beneficial impact of wave-breaking for coherent continuum formation in normally dispersive nonlinear fibers," J. Opt. Soc. Am. B **25**, 1938–1948 (2008).
6. A. M. Heidt, A. Hartung, G. W. Bosman, P. Krok, E. G. Rohwer, H. Schwoerer, and H. Bartelt, "Coherent octave spanning near-infrared and visible supercontinuum generation in all-normal dispersion photonic crystal fibers," Opt. Express **19**, 3775–3787 (2011).
7. Y. Liu, H. Tu, and S. A. Boppart, "Wave-breaking-extended fiber supercontinuum generation for high compression ratio transform-limited pulse compression," Opt. Lett. **37**, 2172–2174 (2012).
8. J. E. Rothenberg, "Femtosecond optical shocks and wave breaking in fiber propagation," J. Opt. Soc. Am. B **6**, 2392–2401 (1989).
9. V. E. Zakharov and A. B. Shabat, "Exact theory of two-dimensional self-focusing and one-dimensional self-modulation of waves in nonlinear media," Sov. Phys. JETP **34**, 62–70 (1972).
10. F. Shimizu, "Frequency broadening in liquid by a short light pulse," Phys. Rev. Lett. **19**, 1097–1100 (1967).
11. A. V. Gorbach, D. V. Skryabin, J. M. Stone, and J. C. Knight, "Four-wave mixing of solitons with radiation and quasi-nondispersive wave packets at the short-wavelength edge of a supercontinuum," Opt. Express **14**, 9854–9863 (2006).
12. L. Cohen, *Time-Frequency Analysis* (Prentice Hall, 1995).
13. R. M. Corless, G. H. Gonnet, D. E. G. Hare, D. J. Jeffrey, and D. E. Knuth, "On the Lambert W function," Adv. Comput. Math. **5**, 329–359 (1996).
14. J. Hansryd, P. A. Andrekson, M. Westlund, J. Li, and P.-O. Hedekvist, "Fiber based optical parametric amplifiers and their applications," IEEE J. Sel. Top. Quantum Electron. **8**, 506–520 (2002).

#193686 - $15.00 USD Received 10 Jul 2013; revised 2 Nov 2013; accepted 5 Nov 2013; published 13 Nov 2013

15. T. Hori, J. Takayanagi, N. Nishizawa, and T. Goto, "Flatly broadened, wideband and low noise supercontinuum generation in highly nonlinear hybrid fiber," Opt. Express **12**, 317–324 (2004).
16. J. J. Miret, E. Silvestre, and P. Andrés, "Octave-spanning ultraflat supercontinuum with soft-glass photonic crystal fibers," Opt. Express **17**, 9197–9203 (2009).

1. Introduction

Optical wave-breaking (OWB) is an effect produced by the interplay between nonlinear processes (chiefly self-phase modulation, SPM) and the chromatic dispersion of optical fibers [1]. The nonmonotonic chirp induced by SPM gives rise to the overlapping between different frequencies in the pulse tails at the normal dispersion regime [2]. This situation leads to nonlinear frequency mixing through χ^3 susceptibility. Indeed OWB can be understood in the spectral domain as a four-wave mixing (FWM) process that produces two spectral sidelobes [3]. At the same time, the interference of such frequencies results in some temporal ripples near the pulse edges.

OWB has been traditionally avoided in practice due to its inherent strong temporal fluctuations [4]. However, in the last years some works have pointed out divers benefits of this process regarding spectral broadening [5, 6] and pulse compression [7]. Particularly, we emphasize OWB as a mechanism for improving smoothness and coherence of supercontinuum spectra [6]. OWB has long been studied both experimentally and numerically [1, 8]. Nevertheless, solely the propagation distance at which the process takes place has been analytically described [2, 5], being other properties only qualitatively understood [3, 5].

In this paper, we address the study of the interaction between SPM and dispersion from a novel analytical approach based on a constant of motion conserved throughout nonlinear propagation of pulses in optical fibers. This procedure allows us to take advantage of some unexploited features related to OWB. Ultimately, we numerically identify certain situations in which we are able to transfer the group-velocity-dispersion (GVD) profile of highly nonlinear fibers to the output pulse spectrum. In principle, our derivation holds for the nonlinear propagation of pulses longer than the picosecond. However, we also discuss in heuristic terms why we expect that the physical processes behind our analysis be at least partially preserved for shorter pulses. So, we will numerically check the validity of our results spreading our simulations up to the case of femtosecond pulses.

2. Nonlinear propagation in optical fibers: a constant of motion

Spectral control of pulsed light in nonlinear fibers requires a good understanding of the interplay between dispersive and nonlinear phenomena. To this end, we tackle systems with an arbitrary dispersion profile in which SPM is the most relevant nonlinear effect. These phenomena govern ps-pulse propagation, being such evolution described by the generalized nonlinear Schrödinger equation (GNLSE) [3],

$$\frac{\partial}{\partial z}A = i\sum_{k=2}^{\infty} i^k \frac{\beta_k}{k!}\frac{\partial^k}{\partial t^k}A + i\gamma_0|A|^2A, \tag{1}$$

where A is the complex envelope of the electric field, $\beta_k = \partial^k\beta(\omega)/\partial\omega^k|_{\omega=\omega_0}$, being $\beta(\omega)$ the propagation constant of the mode supported by the waveguide and ω_0 the carrier frequency, and γ_0 represents the waveguide nonlinear coefficient. Within this framework, and without any additional assumption, in the appendix A we deduce a conservation law that generalizes a previous expression derived by Zakharov and Shabat [9],

$$\frac{d}{dz}\left(\frac{\int_{-\infty}^{\infty}\gamma_0|A(z,t)|^4\mathrm{d}t}{2\int_{-\infty}^{\infty}|A(z,t)|^2\mathrm{d}t} + \frac{\int_{-\infty}^{\infty}\beta_p(\omega)|\tilde{A}(z,\omega-\omega_0)|^2\mathrm{d}\omega}{\int_{-\infty}^{+\infty}|\tilde{A}(z,\omega-\omega_0)|^2\mathrm{d}\omega}\right) = 0, \tag{2}$$

#193686 - $15.00 USD Received 10 Jul 2013; revised 2 Nov 2013; accepted 5 Nov 2013; published 13 Nov 2013

where $\beta_p(\omega) = \beta(\omega) - \beta_0 - \beta_1(\omega - \omega_0)$ and $\tilde{A}$ is the Fourier transform of A.

In order to get physical insight into Eq. (2), on the one hand, it is worth mentioning that the nonlinear coefficient γ_0 appearing at the first fraction in the conservation law parameterizes SPM in Eq. (1). In fact, the level of significance of this nonlinear process is conventionally evaluated (assuming a nearly constant peak power of the pulse, P_0, throughout the propagation) by means of the parameter $L_{NL}^{-1} = \gamma_0 P_0$. The first fraction in Eq. (2), having also dimensions of inverse length, can be understood as a function that generalizes the classical quantity L_{NL}^{-1},

$$\mathscr{L}_{NL}^{-1}(z) = \frac{\int_{-\infty}^{\infty} \gamma_0 |A(z,t)|^4 \mathrm{d}t}{2\int_{-\infty}^{\infty} |A(z,t)|^2 \mathrm{d}t}, \tag{3}$$

and accounts for the relevance of SPM at any distance z during the propagation. At this point it is convenient to remind that the spectral broadening induced by SPM is related to the variations of the temporal intensity of the pulse [10]. Although the classical parameter L_{NL}^{-1} does not assess this pulse-profile variation, we observe that $\mathscr{L}_{NL}^{-1}(z)$ does, decreasing as the temporal pulse intensity becomes flatter and flatter.

On the other hand, if we develop $\beta_p(\omega)$ in Taylor series around ω_0, the second fraction in Eq. (2) can be rewritten as $\sum_{k=2}^{\infty} \beta_k \mu_k(z)/k!$, where μ_k is the normalized kth moment of the pulse spectrum at the baseband. This expression includes the β_k coefficients, which account for the dispersive effects in Eq. (1). For a fiber far from the zero-dispersion wavelength and assuming a smooth pulse profile during the propagation, the quantity $L_D^{-1} = \beta_2/T_0^2$ (T_0 denotes the temporal width of the input pulse) traditionally estimates the impact of dispersion. Therefore, we also define the function

$$\mathscr{L}_D^{-1}(z) = \frac{\int_{-\infty}^{\infty} \beta_p(\omega) |\tilde{A}(z,\omega-\omega_0)|^2 \mathrm{d}\omega}{\int_{-\infty}^{+\infty} |\tilde{A}(z,\omega-\omega_0)|^2 \mathrm{d}\omega}, \tag{4}$$

that generalizes the standard amount L_D^{-1}, and quantifies the action of the whole dispersive processes at the propagation distance z.

Our physical reasoning becomes particularly meaningful when Eq. (2) is rewritten as

$$\mathscr{L}_{NL}^{-1}(z) + \mathscr{L}_D^{-1}(z) = \mathscr{L}_{NL}^{-1}(0) + \mathscr{L}_D^{-1}(0) = C, \tag{5}$$

where the constant C can be calculated only taking into account the initial conditions. From this point of view, nonlinear pulse propagation can be understood as a competition between the activities of SPM and dispersion.

The above equation is going to be the key tool of our spectral control procedure in section 3. To this end, next we discuss some preliminary implications of the above conservation law under certain conditions. We emphasize that our first goal is to achieve a smooth and broad output spectrum. However, it is well-known that the spectral broadening induced by SPM is accompanied by severe spectral oscillations [10]. For this reason, $\mathscr{L}_{NL}^{-1}$ should become smaller as the pulse propagates in order to obtain a smooth output spectrum. At the same time, this requirement results in $\mathscr{L}_D^{-1}$ increases with z according to Eq. (5). Assuming that $\beta_2\mu_2/2$ is the dominant contribution in $\mathscr{L}_D^{-1}$, the above condition (i.e., $\partial_z \mathscr{L}_D^{-1} > 0$) implies $\beta_2 > 0$ since the pulse spectrum broadens through propagation along the fiber (i.e., $\partial_z \mu_2 > 0$). Therefore, as is well known, it is crucial to pump at the normal dispersion regime to achieve a smooth output spectrum in conventional fibers [5]. The above dynamics is illustrated in Fig. 1. The conditions that give rise to this evolution, namely, high nonlinearity and normal dispersion regime, become apparent in this figure through the inequalities $\mathscr{L}_{NL}^{-1}(0) \gg \mathscr{L}_D^{-1}(0)$ and $\mathscr{L}_D^{-1}(z) > 0$, respectively. It is interesting to note that, although $\mathscr{L}_{NL}^{-1}$ is the main contribution to the constant of motion at the beginning, $\mathscr{L}_D^{-1}$ dominates after a long enough z distance (say, z_{out}, the output

#193686 - $15.00 USD Received 10 Jul 2013; revised 2 Nov 2013; accepted 5 Nov 2013; published 13 Nov 2013

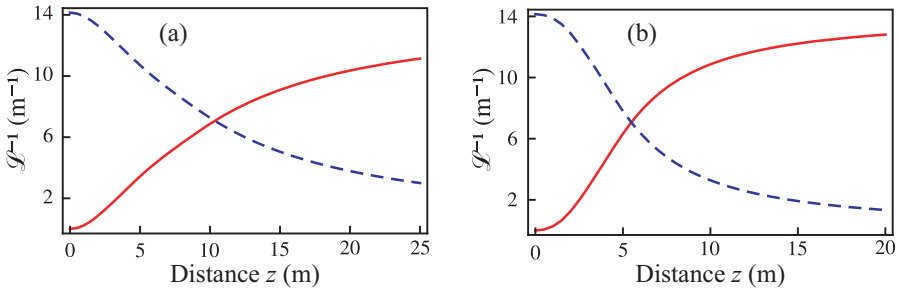

Fig. 1. Plot of the evolution of the functions $\mathscr{L}_{NL}^{-1}$ (dashed curve) and $\mathscr{L}_{D}^{-1}$ (solid curve) for a 5 ps Gaussian input pulse centered at 1550 nm ($\omega_0 = 1215\,\mathrm{rad\,ps^{-1}}$) and 100 W peak power, which propagates throughout two fibers with $\gamma_0 = 400\ \mathrm{W^{-1}km^{-1}}$ and dispersion behavior defined by: (a) $\beta_2 = 20\,\mathrm{ps^2km^{-1}}$ and $\beta_k = 0$ for $k > 2$, i.e., flat GVD profile; and (b) $\beta_2 = 20\,\mathrm{ps^2km^{-1}}$, $\beta_3 = 0$, $\beta_4 = 1\,\mathrm{ps^4km^{-1}}$, and $\beta_k = 0$ for $k > 4$, i.e., parabolic GVD profile.

distance). So, based in Eq. (5), in a first-order approximation we can write

$$\mathscr{L}_{D}^{-1}(z_{\mathrm{out}}) \approx \mathscr{L}_{NL}^{-1}(0) \approx C. \tag{6}$$

This behavior, characterized by high nonlinearity and normal dispersion, leads to a stage in which $\mathscr{L}_{D}^{-1} > \mathscr{L}_{NL}^{-1}$. In such a situation, spectral broadening cannot be mainly produced by SPM. However, as is well known, pulses that propagate at normal dispersion regime experience OWB [2]. To check that the spectral broadening in this scenario is produced by OWB, we approximately compute the distance z_c for which the new nonlinear and dispersive functions of z intersect each other. In this case we write $2\mathscr{L}_{D}^{-1}(z_c) = 2\left(\sum_{k=2}^{\infty}\beta_k\mu_k(z_c)/k!\right) = C$. As SPM is the dominant effect at the first phase of propagation, in order to calculate z_c we estimate μ_k at this distance using the SPM-induced chirp with an equivalent peak pulse power of $P_0/\sqrt{2}$ since $2\mathscr{L}_{NL}^{-1}(z_c) \approx \mathscr{L}_{NL}^{-1}(0)$ and, according to Eq. (3), the square of the power widening needs to be taken into account. If we consider a flat GVD curve, i.e., $\beta_k = 0$ for $k > 2$, and a Gaussian input pulse, we obtain $z_c \approx 1.61\sqrt{L_D L_{NL}} = 1.61\sqrt{T_0^2/\beta_2\gamma_0 P_0}$. For the case corresponding to Fig. 1(a) we get $z_c \approx 9.0$ m, which is in close agreement with the abscissa of the intersection point of the curves in this figure. In addition, the above distance is greater than the OWB distance derived in [2], $1.06\sqrt{L_D L_{NL}}$, that takes into account the point at which OWB just begins. Our conclusion is clear. We can consider z_c as the OWB distance at which OWB is the dominant nonlinear process at the second stage of the pulse propagation. Unlike the procedure for calculating the OWB distance in [2], that is restricted to certain simple cases, our interpretation allows the evaluation of z_c for both any dispersion curve and any input pulse profile. In this way, following our criterion, the OWB distance of the system corresponding to Fig. 1(b), with a non constant dispersion, turns to be $z_c = 5.5$ m.

3. Dispersion-to-spectrum mapping: direct spectral shaping through dispersion engineering

Now, if we write Eq. (6) in its integral form,

$$\int_{-\infty}^{+\infty}(\omega-\omega_0)^2\left(\frac{1}{2!}\beta_2+\frac{1}{3!}\beta_3(\omega-\omega_0)+\frac{1}{4!}\beta_4(\omega-\omega_0)^2+\ldots\right)\left|\tilde{A}(z_{\mathrm{out}},\omega-\omega_0)\right|^2\mathrm{d}\omega$$
$$\approx \frac{1}{2}\int_{-\infty}^{\infty}\gamma_0\left|A(0,t)\right|^4\mathrm{d}t, \tag{7}$$

#193686 - $15.00 USD Received 10 Jul 2013; revised 2 Nov 2013; accepted 5 Nov 2013; published 13 Nov 2013

it can be noticed that, once γ_0 and the input pulse profile are fixed, the left-hand side in Eq. (7) must go to the same value regardless of the function $\beta_p(\omega)$. It is apparent that the shape of the output pulse spectrum is strongly correlated with the waveguide dispersion during the second stage of pulse propagation ($z > z_c$), when dispersion dominates dynamics and OWB is working. With the aim of explaining this correlation, we study the spectral transfer of energy occuring during pulse propagation, focusing our attention on the power flow from red-shifted (blue-shifted) SPM-generated frequencies towards lower (higher) ones.

As we said before, OWB can be interpreted as a degenerate FWM between frequencies in the pulse tails. However, even beyond z_c we cannot ignore the nonlinear processes involving instantaneous frequencies in the central region of the pulse. In other words, the pulse evolves in the spectral domain through a set of intrapulse FWM processes [11] that involves frequencies located at both the central part and the outer tails. We use this spectral picture to study the power spreading. In order to define the waves that are nonlinearly mixed, it is convenient to write the complex envelope of the field around a generic time t_k as

$$A(t) = |A(t_k)|\, e^{i\varphi(t_k)} e^{i\left(\partial\varphi(t)/\partial t|_{t=t_k}\right)(t-t_k)}, \tag{8}$$

where we consider both a linear approximation of the phase φ and a slow variation of the envelope modulus $|A|$ compared with the phase. Equation (8) defines locally monochromatic waves with angular frequency $\delta\omega = \omega - \omega_0 = -\partial_t\varphi|_{t_k}$, power $|A(t_k)|^2$, and phase $\varphi(t_k)$. The above statement is on the basis of the physical meaning of the instantaneous frequency [12].

Next, we analyze the nonlinear pulse propagation as a process divided in the two sequential steps advanced in section 2. At the first stage, $z < z_c$, we consider that only SPM rules the pulse evolution. In this way, we can use the SPM-induced chirp to define the frequency of locally monocromatic waves at z_c. Note that the instantaneous power and frequency of every monochromatic wave can be worked out at z_c. In particular, for a Gaussian input pulse the power associated at a certain instantaneous frequency is given by

$$P(\delta\omega, z_c) = \frac{P_0}{\sqrt{2}} \exp\left[\frac{1}{2}\mathscr{W}_l\left(-\frac{1}{e}\frac{\delta\omega^2}{{\delta\omega_{max}}^2}\right)\right], \tag{9}$$

where $\mathscr{W}_l$ is the Lambert function of order l [13] ($l = -1$ for the tails and $l = 0$ for the central region of the pulse), and $\delta\omega_{\max} = \gamma_0 P_0 z_c / T_0\sqrt{e}$ is the maximum chirp achieved by the pulse at z_c [see Fig. 2].

At the second phase, $z > z_c$, each locally monochromatic wave that is present at z_c acts as the pump in multiple degenerate FWM processes with the nearby waves such that $2\omega_p = \omega_s + \omega_i$, where the subscripts p, s and i refer to pump, signal, and idler, respectively. Note that the above frequency mixing occurs at both the central part and the tails of the pulse. This panorama is graphically sketched in Fig. 2. In order to simplify the analysis, we only take into acount processes for which the pump power is much greater than the signal and idler powers ($P_p \gg P_s, P_i$) and $P_i(z_c) = 0$. In any such case, the production of idler photons for any input pulse shape is given by [14]

$$P_i(z) = P_s(z_c)\gamma_0^2 P_p^2(z_c)\frac{\sin^2(|g|z)}{|g|^2}, \tag{10}$$

where $|g|^2 = \Delta\beta\left[\Delta\beta/4 + \gamma_0 P_p(z_c)\right]$ is the squared modulus of the gain of a generic elementary process and $\Delta\beta = \beta(\omega_s) + \beta(\omega_i) - 2\beta(\omega_p)$ is the low power propagation mismatch. We point out that the boundary values of the pump frequencies are given by the frequencies at which the pulse chirp reaches its minimum or maximum at z_c, as one can see in Fig. 2.

Equation (10) presents a strong oscillatory behavior with z. This fact is due to the high value that the gain shows around z_c, $|g| \approx L_{NL}^{-1}$. If we average Eq. (10) along z, we obtain the trend for

#193686 - $15.00 USD Received 10 Jul 2013; revised 2 Nov 2013; accepted 5 Nov 2013; published 13 Nov 2013

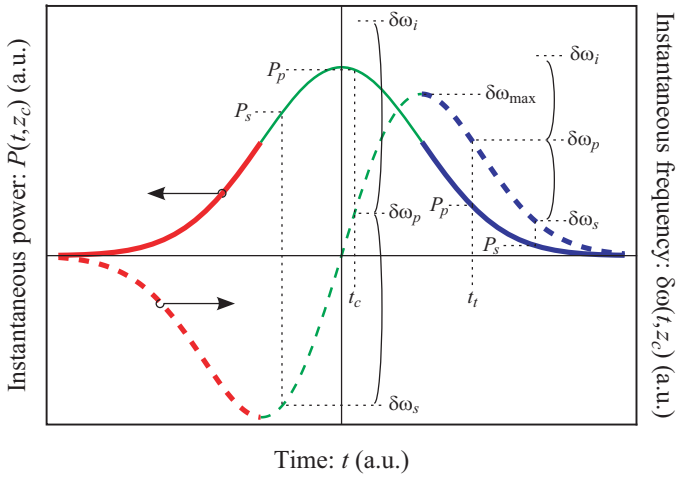

Fig. 2. Sketch for the interpretation of the FWM processes considered here. We assume that the schematic plots of the instantaneous frequency and instantaneous power correspond to the distance z_c. Thick lines denote instantaneous frequencies and their corresponding instantaneous power at the pulse tails (blue and red regions). For two cases (in the central region, t_c, and in the trailing edge, t_t), we represent an arbitrary pump wave, $\delta\omega_p$, interacting with a signal wave, $\delta\omega_s$, and producing a certain idler wave, $\delta\omega_i$.

the power corresponding to the production of idler frequencies, i.e.,

$$\langle P_i(z)\rangle \approx \frac{1}{2|g|^2} P_s(z_c)\gamma_0^2 P_p^2(z_c). \tag{11}$$

Finally the total flow from a pump frequency to the rest can be estimated by integrating for all the possible values of ω_s satisfying the above power requirements (i.e., $P_p \gg P_s, P_i$),

$$\delta P_p(z) \approx -2\int \langle P_i(z)\rangle \, \mathrm{d}\omega_s \approx -\int \frac{P_s(z_c)\gamma_0 P_p(z_c)}{\Delta\beta\left[1+\frac{\Delta\beta}{4\gamma_0 P_p(z_c)}\right]}\mathrm{d}\omega_s. \tag{12}$$

The above expression seems to diverge when $\omega_s \approx \omega_p$ since $\Delta\beta \approx 0$. However the description of those frequencies are, in fact, out of the model depicted by Eq. (10). In addition, it is easy to check, bearing in mind [14], that the net flow between two neighboring frequencies goes to zero as both frequencies approach each other. Going one step further, and according to [3], we write $\Delta\beta \approx (\omega_s - \omega_p)^2\beta_2(\omega_p)$, in the lowest-order approximation. In this way, the integrand of the right-hand side in Eq. (12), excluding $\beta_2(\omega_p)$ and $P_p(z_c)$, shows a small variation on ω_s and ω_p since it is far away from the poles. Actually, Eq. (9) can be used to verify this issue when we deal with a Gaussian input pulse. So, the above statements indicate that the power spreading rate roughly goes as the inverse of the group-velocity dispersion. This fact can be expressed in mathematical terms as

$$\delta P_p(z) \propto -P_p(z_c)/\beta_2(\omega_p). \tag{13}$$

This conclusion is in agreement with the fact that supercontinuum spectrum becomes nearly flat when $\beta_2(\omega)$ is constant [15, 16]. Note that in this case the modulus of the power flow, $|\delta P_p(z)|$, is higher in the regions in which P_p is greater. So, the power leakage shifts the spectrum power from the high values to the low ones. In this way, if z_{out} is large enough, the rapid and nearly-regular oscillations of the spectrum at the OWB distance [3] are mitigated and the output power spectrum, $S(\omega, z_{\text{out}})$, becomes uniform.

#193686 - $15.00 USD Received 10 Jul 2013; revised 2 Nov 2013; accepted 5 Nov 2013; published 13 Nov 2013

When $\beta_2(\omega)$ is not constant, the above process still operates locally, in such a way that oscillations are also damped. However, the spectral power spreading is stronger when $1/\beta_2$ is larger. So, now $S(\omega, z_{\text{out}})$ should adopt the $(1/\beta_2)$-profile around the carrier frequency. At this point it is important to recognize that the variation of $-1/\beta_2(\omega)$ around the central frequency of the pulse ($\delta\omega_p = 0$) approximately agrees with that of the function $\beta_2(\omega_p)$ itself, except by a negative additive constant. This plausible conclusion is, in addition, consistent to Eq. (7) and can be mathematically expressed as

$$S(\omega, z_{\text{out}}) \sim \mathscr{M}(\omega, z_{\text{out}})\beta_2(\omega) + \mathscr{N}(\omega, z_{\text{out}}), \tag{14}$$

where $\mathscr{M}$ and $\mathscr{N}$ are in principle nearly flattened functions of ω and consequently they only account for the fine detail of the spectral shape. Despite of the approximations considered in the derivation of Eq. (14), it retains enough information about the physical processes governing the nonlinear pulse propagation and predicts a clear spectral trend within the regime where it is derived (namely, high nonlinearity and normal dispersion), as it is verified numerically in the next section.

4. Numerical results

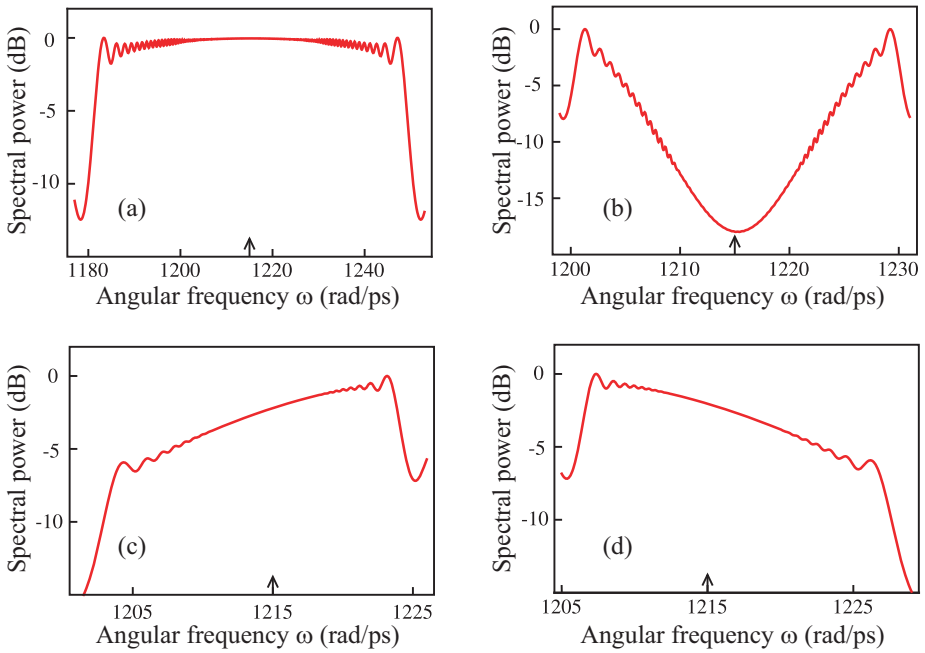

Fig. 3. Normalized output spectrum in dB for: (a) constant dispersion profile; (b) parabolic one; and linear dispersion variation with (c) $\beta_3 > 0$ and (d) $\beta_3 < 0$. See input pulse details and dispersion fiber values in the text. The small arrow corresponds to the location of the carrier frequency.

Let us consider a highly nonlinear fiber characterized by $\gamma_0 = 400\,\text{W}^{-1}\text{km}^{-1}$, and a 5 ps Gaussian input pulse with $P_0 = 100\,\text{W}$, centered at 1550 nm ($\omega_0 = 1215\,\text{rad ps}^{-1}$). Our calculations include four different normal GVD-profiles. The first two cases, illustrated in Figs. 3(a) and 3(b), are that described in the caption of Fig. 1. The fiber length is $z_{\text{out}} = 25\,\text{m}$ in Fig. 3(a)

#193686 - $15.00 USD Received 10 Jul 2013; revised 2 Nov 2013; accepted 5 Nov 2013; published 13 Nov 2013

and $z_{out} = 20\,\mathrm{m}$ in Fig. 3(b). The third and fourth situations correspond to linear dispersion profiles with $\beta_2 = 200\,\mathrm{ps}^2\mathrm{km}^{-1}$ and $\beta_3 = \pm 10\,\mathrm{ps}^3\mathrm{km}^{-1}$, respectively, and $z_{out} = 10\,\mathrm{m}$. We evaluate the input pulse propagation throughout the above four fibers solving Eq. (1) by means of a Runge-Kutta-type algorithm. From Fig. 3 the conclusion is evident. Around the central ω_0-region, the output spectrum embraces the shape of the fiber $\beta_2(\omega)$-profile, in good agreement with Eq. (14). The effective spectral bandwidth covers around 90 nm in Fig. 3(a) and about 30 nm in the rest of cases. The dispersion-to-spectrum mapping is clearly achieved. It is worth noticing that the logarithmic representation of spectra mantains grosso modo the behavior described by Eq. (14) since logarithm is a soft and monotonic function.

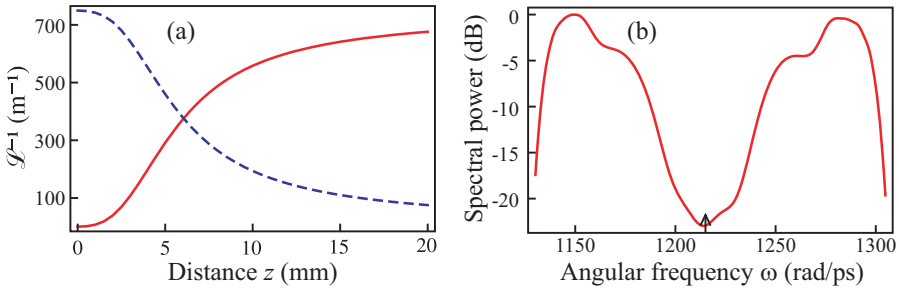

Fig. 4. (a) Plot of the evolution of the functions $\mathscr{L}_{NL}^{-1}$ (dashed curve) and $\mathscr{L}_{D}^{-1}$ (solid curve) for a FWHM 250 fs Gaussian input pulse and parabolic $\beta_2(\omega)$-fiber profile; and (b) normalized output spectrum in dB. The rest of input pulse details and dispersion fiber values are discussed in the text. The small arrow corresponds to the location of the carrier frequency.

In order to enlarge the useful spectral bandwidth, it is worth noting at this point that we achieve the above mapping by describing OWB as a combination of multiple degenerate FWM processes, provided that $\mathscr{L}_{D}^{-1}$ increases and $\mathscr{L}_{NL}^{-1}$ decreases in a smooth and monotonic way even though the sum of both quantities be not strictly constant. Based on this fact, we expect that the above mapping be at least partially preserved for femtosecond pulses. So, now we consider a 250 fs Gaussian input pulse with 5.3 kW peak power and a fiber such that $z_{out} = 20\,\mathrm{mm}$. The rest of fiber and pulse parameters are the same as in Fig. 3(b). In this case we have included higher order effects as self-steepening and intrapulse Raman scattering in the GNLSE for the computation of the nonlinear propagation of such a pulse. The evolution of the functions $\mathscr{L}_{D}^{-1}$ and $\mathscr{L}_{NL}^{-1}$ for this situation is shown in Fig. 4(a). The resulting output parabolic spectral power shown in Fig. 4(b) confirms that we are able to achieve to a great extend the dispersion-to-spectrum mapping with ultrashort pulses. Now the useful spectral interval length is about 190 nm.

5. Conclusions

We emphasize that the new functions $\mathscr{L}_{NL}^{-1}$ and $\mathscr{L}_{D}^{-1}$ are a useful generalization of the classical parameters L_{NL}^{-1} and L_{D}^{-1} described in [3]. Going one step further, it is really notable that under certain quite usual conditions the addition of both mathematical quantities results in a constant of motion for nonlinear pulse propagation in waveguides. It is worth mentioning that their definition in terms of integrals of the pulse magnitudes leads to study the interplay between dispersion and SPM without detailed information about the pulse itself.

In the second part of the work, the above conservation law at the normal dispersion regime has been successfully applied to exploit some OWB features. Particularly, it allows to study

#193686 - $15.00 USD Received 10 Jul 2013; revised 2 Nov 2013; accepted 5 Nov 2013; published 13 Nov 2013

the OWB-induced power flow that broadens the pulse spectrum and maps the GVD shape of the fiber, $\beta_2(\omega)$, to the power spectrum profile of the output pulse, $S(\omega)$, around the carrier frequency. This result has been computationally checked even under conditions that overpass the initial input pulse requirements. We point out that this mapping permits in a very simple way to manipulate the emerging spectrum by dispersion engineering of any nonlinear waveguide in which pulse propagation is described by means of a GNLSE-type equation.

Appendix: Derivation of the conservation law

Let us write Eq. (1) in the spectral domain,

$$\frac{\partial}{\partial z}\tilde{A}(z,\omega-\omega_0) = i\beta_p(\omega)\tilde{A}(z,\omega-\omega_0) + i\gamma_0\mathscr{F}\left(|A(z,t)|^2A(z,t)\right), \tag{15}$$

where $\mathscr{F}(\circ) = \int_{-\infty}^{+\infty} \mathrm{d}t\, e^{i(\omega-\omega_0)t}\circ$. The propagation equation for the power spectrum is directly derived from the above equation,

$$\frac{\partial}{\partial z}|\tilde{A}|^2 = 2\Re\left[\tilde{A}^* i\gamma_0\mathscr{F}\left(|A|^2A\right)\right], \tag{16}$$

where $\Re$ stands for the real part of a complex expression. Multiplying by $\beta_p(\omega)$ both sides of Eq. (16) and taking into account Eq. (15), we obtain

$$\frac{\partial}{\partial z}\left(\beta_p(\omega)|\tilde{A}|^2\right) = -2\Re\left[\gamma_0\mathscr{F}\left(|A|^2A\right)\frac{\partial}{\partial z}\tilde{A}^*\right]. \tag{17}$$

At this point, if we consider $\tilde{A}^*(\omega) = \mathscr{F}\left(A^*(-t)\right)$ and apply the convolution theorem of Fourier theory, we achieve

$$\frac{\partial}{\partial z}\left(\beta_p(\omega)|\tilde{A}|^2\right) = -2\Re\left[\gamma_0\mathscr{F}\left(\int_{-\infty}^{\infty}|A(\tau)|^2A(\tau)\frac{\partial}{\partial z}A^*(t+\tau)\mathrm{d}\tau\right)\right]. \tag{18}$$

Now, integrating over ω and taking into account $\int_{-\infty}^{+\infty} e^{i(\omega-\omega_0)t}\mathrm{d}\omega = 2\pi\delta(t)$ to simplify the right-hand side, where δ is the Dirac delta function, we derive

$$\frac{\partial}{\partial z}\left(\int_{-\infty}^{\infty}\frac{1}{2\pi}\beta_p(\omega)|\tilde{A}|^2\mathrm{d}\omega + \int_{-\infty}^{\infty}\frac{\gamma_0}{2}|A|^4\mathrm{d}t\right) = 0. \tag{19}$$

Finally, Eq. (2) is obtained considering the conservation energy of these systems. Note that in the particular case $\beta_p(\omega) = (\omega-\omega_0)^2\beta_2$, we recover one of the conservation laws derived in [9].

Acknowledgments

This work was financially supported by the Plan Nacional I+D+I under the research project TEC2008-05490, Ministerio de Ciencia e Innovación (Spain), and by the Generalitat Valenciana under the grant PROMETEO 2009-077. One of the authors, D. C.-L., gratefully acknowledges funding from the Generalitat Valenciana (VALi+d predoctoral contract). P. A. and E. S. acknowledge fruitful discussions with J. J. Miret at the Universidad de Alicante, Spain.

#193686 - $15.00 USD Received 10 Jul 2013; revised 2 Nov 2013; accepted 5 Nov 2013; published 13 Nov 2013

Paper III

Comparative analysis of spectral coherence in microresonator frequency combs

V. Torres-Company, D. Castelló-Lurbe, and E. Silvestre

in *Optics Express*, Vol. 22, No. 4, pp. 4678–4691, February 2014.

Comparative analysis of spectral coherence in microresonator frequency combs

Victor Torres-Company,[1] **David Castelló-Lurbe,**[2] **and Enrique Silvestre**[2,*]

[1]*Department of Microtechnology and Nanoscience, Chalmers University of Technology, SE-41296 Gothenburg, Sweden*
[2]*Departament d'Òptica, Universitat de València, 46100 Burjassot, Spain*
[*]*enrique.silvestre@uv.es*

Abstract: Microresonator combs exploit parametric oscillation and nonlinear mixing in an ultrahigh-Q cavity. This new comb generator offers unique potential for chip integration and access to high repetition rates. However, time-domain studies reveal an intricate spectral coherence behavior in this type of platform. In particular, coherent, partially coherent or incoherent combs have been observed using the same microresonator under different pumping conditions. In this work, we provide a numerical analysis of the coherence dynamics that supports the above experimental findings and verify particular design rules to achieve spectrally coherent microresonator combs. A particular emphasis is placed in understanding the differences between so-called Type I and Type II combs.

OCIS codes: (320.7110) Ultrafast nonlinear optics; (030.1640) Coherence; (130.3990) Micro-optical devices.

References and links

1. D. J. Jones, S. A. Diddams, J. K. Ranka, A. Stentz, R. S. Windeler, J. L. Hall, and S. T. Cundiff, "Carrier-envelope phase control of femtosecond mode-locked lasers and direct optical frequency synthesis," Science **288**, 635–639 (2000).
2. S. A. Diddams, D. J. Jones, J. Ye, S. T. Cundiff, J. L. Hall, J. K. Ranka, R. S. Windeler, R. Holzwarth, T. Udem, and T. W. Hänsch, "Direct link between microwave and optical frequencies with a 300 THz femtosecond laser comb," Phys. Rev. Lett. **84**, 5102–5105 (2000).
3. T. W. Hänsch, "Nobel Lecture: Passion for precision," Rev. Mod. Phys. **78**, 1297–1309 (2006).
4. N. R. Newbury, "Searching for applications with a fine-tooth comb," Nature Photon. **5**, 186–188 (2011).
5. V. Torres-Company and A. M. Weiner, "Optical frequency comb technology for ultra-broadband radio-frequency photonics," Laser and Photon. Rev. (in press, 2013). DOI 10.1002/lpor201300126.
6. T. J. Kippenberg, R. Holzwarth, and S. A. Diddams, "Microresonator-based optical frequency combs," Science **332**, 555–559 (2011).
7. P. Del'Haye, A. Schliesser, O. Arcizet, T. Wilken, R. Holzwarth, and T. J. Kippenberg, "Optical frequency comb generation from a monolithic microresonator," Nature **450**, 1214–1217 (2007).
8. A. A. Savchenkov, A. B. Matsko, V. S. Ilchenko, I. Solomatine, D. Seidel, and L. Maleki, "Tunable optical frequency comb with a crystalline whispering gallery mode resonator," Phys. Rev. Lett. **101**, 093902 (2008).
9. W. Liang, A. A. Savchenkov, A. B. Matsko, V. S. Ilchenko, D. Seidel, and L. Maleki, "Generation of near-infrared frequency combs from a MgF2 whispering gallery mode resonator," Opt. Lett. **36**, 2290–2292 (2011).
10. L. Razzari, D. Duchesne, M. Ferrera, R. Morandotti, S. Chu, B. E. Little, and D. J. Moss, "CMOS-compatible integrated optical hyper-parametric oscillator," Nat. Photonics **4**, 41–45 (2010).
11. J. S. Levy, A. Gondarenko, M. A. Foster, A. C. Turner-Foster, A. L. Gaeta, and M. Lipson, "CMOS-compatible multiple-wavelength oscillator for on-chip optical interconnects," Nat. Photonics **4**, 37–40 (2010).

#203476 - $15.00 USD Received 26 Dec 2013; revised 8 Feb 2014; accepted 13 Feb 2014; published 20 Feb 2014

12. H. Jung, C. Xiong, K. Y. Fong, X. F. Zhang, and H. X. Tang, "Optical frequency comb generation from aluminum nitride microring resonator," Opt. Lett. **38**, 2810–2813 (2013).
13. Y. Okawachi, K. Saha, J. S. Levy, Y. H. Wen, M. Lipson, and A. L. Gaeta, "Octave-spanning frequency comb generation in a silicon nitride chip," Opt. Lett. **36**, 3398–3400 (2011).
14. P. Del'Haye, T. Herr, E. Garvatin, M. L. Gorodetsky, R. Holzwarth, and T. J. Kippenberg, "Octave spanning tunable frequency comb from a microresonator," Phys. Rev. Lett. **107**, 063901 (2011).
15. M. A. Foster, A. C. Turner, R. Salem, M. Lipson, and A. L. Gaeta, "Broad-band continuous-wave parametric wavelength conversion in silicon nanowaveguides," Opt. Express **15**, 12949–12958 (2007).
16. L. Zhang, Y. Yue, R. G. Beausoleil, and A. E. Willner, "Analysis and engineering of chromatic dispersion in silicon waveguide bends and ring resonators," Opt. Express **19**, 8102–8107 (2011).
17. J. Riemensberger, K. Hartinger, T. Herr, V. Brasch, R. Holzwarth, and T. J. Kippenberg, "Dispersion engineering of thick high-Q silicon nitride ring-resonators via atomic layer deposition," Opt. Express **20**, 27661–27669 (2012).
18. I. S. Grudinin, L. Baumgartel, and N. Yu, "Frequency comb from a microresonator with engineered spectrum," Opt. Express **20**, 6604–6609 (2012).
19. J. Li, H. Lee, T. Chen, and K. J. Vahala, "Low-pump-power, low-phase-noise, and microwave to millimeter-wave repetition rate operation in microcombs," Phys. Rev. Lett. **109**, 233901 (2012).
20. A. A. Savchenko, A. B. Matsko, W. Liang, V. S. Ilchenko, D. Seidel, L. Maleki, "Kerr combs with selectable central frequency," Nature Photon. **5**, 293–296 (2011).
21. K. Saha, Y. Okawachi, J. S. Levy, R. K. W. Lau, K. Luke, M. A. Foster, M. Lipson, and A. L. Gaeta, "Broadband parametric frequency comb generation with a 1 μm pump source," Opt. Express **20**, 26935–26941 (2012).
22. C. Y. Wang, T. Herr, P. Del'Haye, A. Schliesser, J. Hofer, R. Holzwarth, T. W. Hänsch, N. Picque, and T. J. Kippenberg, "Mid-infrared optical frequency combs at 2.5 μm based on crystalline microresonators," Nature Commun. **4**, 1345 (2013).
23. D. J. Moss, R. Morandotti, A. L. Gaeta, and M. Lipson, "New CMOS-compatible platforms based on silicon nitride and Hydex for nonlinear optics," Nat. Photonics **7**, 597–607 (2013).
24. F. Ferdous, H. X Miao, D. E. Leaird, K. Srinivasan, J. Wang, L. Chen, L. T. Varghese, and A. M. Weiner, "Spectral line-by-line pulse shaping of on-chip microresonator frequency combs," Nat. Photonics **5**, 770–776 (2011).
25. S. B. Papp and S. A. Diddams, "Spectral and temporal characterization of a fused-quartz-microresonator optical frequency comb," Phys. Rev. A **84**, 053833 (2011).
26. S. T. Cundiff and A. M. Weiner, "Optical arbitrary waveform generation," Nat. Photonics **4**, 760–766 (2010).
27. F. Ferdous, H. X. Miao, P. H. Wang, D. E. Leaird, K. Srinivasan, L. Chen, V. Aksyuk, and A. M. Weiner, "Probing coherence in microcavity frequency combs via optical pulse shaping," Opt. Express **20**, 21033–21043 (2012).
28. P. H. Wang, F. Ferdous, H. X Miao, J. Wang, D. E. Leaird, K. Srinivasan, L. Chen, V. Aksyuk, and A. M. Weiner, "Observation of correlation between route to formation, coherence, noise, and communication performance of Kerr combs," Opt. Express **20**, 29284–29295 (2012).
29. T. Herr, K. Hartinger, J. Riemesberger, C. Y. Wang, E. Gavartin, R. Holzwarth, M. L. Gorodetsky, and T. J. Kippenberg, "Universal formation dynamics and noise of Kerr-frequency combs in microresonators," Nat. Photonics **6**, 480–487 (2012).
30. A. B. Matsko, A. A. Savchenko, D. Strekalov, V. S. Ilchenko, and L. Maleki, "Optical hyperparametric oscillations in a whispering-gallery-mode resonator: Threshold and phase diffusion," Phys. Rev. A **71**, 033804 (2005).
31. Y. K. Chembo and N. Yu, "Modal expansion approach to optical-frequency-comb generation with monolithic whispering-gallery-mode resonators," Phys. Rev. A **82**, 033801 (2010).
32. A. B. Matsko, A. A. Savchenko, W. Liang, V. S. Ilchenko, D. Seidel, and L. Maleki, "Mode-locked Kerr frequency combs," Opt. Lett. **36**, 2845–2847 (2011).
33. A. B. Matsko, A. A. Savchenko, V. S. Ilchenko, D. Seidel, and L. Maleki, "Hard and soft excitation regimes of Kerr frequency combs," Phys. Rev. A **85**, 023830 (2012).
34. Y. K. Chembo and C. R. Menyuk, "Spatiotemporal Lugiato-Lefever formalism for Kerr-comb generation in whispering gallery-mode resonators," Phys. Rev. A **87**, 053852 (2013).
35. S. Coen, H. G. Randle, T. Sylvestre, and M. Erkintalo "Modeling of octave-spanning Kerr frequency combs using a generalized mean-field Lugiato-Lefever model," Opt. Lett. **38**, 37–39 (2013).
36. T. Hansson, D. Modotto, and S. Wabnitz, "Dynamics of the modulation instability in microresonator frequency combs," Phys. Rev. A **88**, 023819 (2013).
37. C. Godey, I. Balakireva, A. Colleit, and Y. K Chembo, "Stability analysis of the Lugiato-Lefever model for Kerr optical frequency combs. Part I: case of normal dispersion," arXiv: 1308.2539.
38. S. Coen and M. Erkintalo, "Universal scaling laws of Kerr frequency combs," Opt. Lett. **38**, 1790–1792 (2013).
39. A. B. Matsko, W. Liang, A. A. Savchenko, and L. Maleki, "Chaotic dynamics of frequency combs generated with continuously pumped nonlinear microresonators," Opt. Lett. **38**, 525–527 (2013).
40. T. J. Kippenberg, S. M. Spillane, K. J. Vahala, "Kerr-nonlinearity optical parametric oscillation in ultrahigh-Q toroid microcavity," Phys. Rev. Lett. **93**, 083904 (2004).
41. L. A. Lugiato and R. Lefever, "Spatial dissipative structures in passive optical systems," Phys. Rev. Lett. **58**, 2209–2211 (1987).

#203476 - $15.00 USD Received 26 Dec 2013; revised 8 Feb 2014; accepted 13 Feb 2014; published 20 Feb 2014

42. T. Herr, V. Brasch, J. D. Jost, C. Y. Wang, N. M. Kondratiev, M. L. Gorodetsky, and T. J. Kippenberg, "Temporal solitons in optical microresonators," Nat. Photonics **8**, 145–152 (2014).
43. F. Leo, S. Coen, P. Kockaert, S. P. Goza, P. Emplit, and M. Haelterman, "Temporal cavity solitons in one-dimensional Kerr media as bits in an all-optical buffer," Nat. Photonics **4**, 471–476 (2010).
44. H. Lajunen, V. Torres-Company, J. Lancis, E. Silvestre, and P. Andres, "Pulse-by-pulse method to characterize partially coherent pulse propagation in instantaneous nonlinear media," Opt. Express **18**, 14979–14991 (2010).
45. M. Erkintalo and S. Coen, "Coherence properties of Kerr frequency combs," Opt. Lett. **39**, 283–286 (2014).
46. M. Haelterman, S. Trillo, and S. Wabnitz, "Additive-modulation-instability ring laser in the normal dispersion regime of a fiber," Opt. Lett. **17**, 745–747 (1992).
47. I. V. Barashenkov and Y. S. Smirnov, "Existence and stability chart for the ac-driven, damped nonlinear Schrodinger solitons," Phys. Rev. E **54**, 5707–5725 (1996).
48. F. Leo, L. Gelens, P. Emplit, M. Haelterman, and S. Coen, "Dynamics of one-dimensional Kerr cavity solitons," Opt. Express **21**, 9180–9191 (2013).
49. Y. K. Chembo, D. V. Strekalov, and N. Yu, "Spectrum and dynamics of optical frequency combs generated with monolithic whispering gallery mode resonators," Phys. Rev. Lett. **104**, 103902 (2010).
50. J. M. Dudley and S. Coen, "Coherence properties of supercontinuum spectra generated in photonic crystal and tapered fibers," Opt. Lett. **27**, 1180–1182 (2002).
51. J. M. Dudley, G. Genty, and S. Coen, "Supercontinuum generation in photonic crystal fibers," Rev. Mod. Phys. **78**, 1135–1184 (2006).
52. G. Genty, M Surakka, J. Turunen, and A. T. Friberg, "Second-order coherence of supercontinuum light," Opt. Lett. **35**, 3057–3059 (2010).
53. T. Godin, B. Wetzel, T. Sylvestre, L. Larger, A. Kudlinski, A. Mussot, A. Ben Salem, M. Zghal, G. Genty, F. Dias, and J. M. Dudley, "Real time noise and wavelength correlations in octave-spanning supercontinuum generation," Opt. Express **21**, 18452–18460 (2013).
54. G. P. Agrawal, *Nonlinear Fiber Optics*, 4th ed. (Academic, 2007).
55. M. R. E. Lamont, Y. Okawachi, and A. L. Gaeta, "Route to stabilized ultrabroadband microresonator-based frequency combs," Opt. Lett. **38**, 3478–3481 (2013).
56. K. Saha, Y. Okawachi, B. Shim, J. S. Levy, R. Salem, A. R. Johnson, M. A. Foster, M. R. E. Lamont, M. Lipson, and A. L. Gaeta, "Modelocking and femtosecond pulse generation in chip-based frequency combs," Opt. Express **21**, 1335–1343 (2013).
57. S. B. Papp, P. Del'Haye, and S. A. Diddams, "Parametric seeding of a microresonator optical frequency comb," Opt. Express **21**, 17615–17624 (2013).
58. M. Peccianti, A. Pasquazi, Y. Park, B. E. Little, S. T. Chu, D. J. Moss, and R. Morandotti, "Demonstration of a stable ultrafast laser based on a nonlinear microcavity," Nature Commun. **3**, 765 (2012).
59. P. Del'Haye, S. B. Papp, and S. A. Diddams, "Self-injection locking and phase-locked states in microresonator-based optical frequency combs," Phys. Rev. Lett. **112**, 043905 (2014).

1. Introduction

An optical frequency comb is a laser source with a spectrum composed by a set of evenly spaced components that maintain the phase coherence across the whole bandwidth. Thanks to the self-referencing technique for femtosecond mode-locked lasers [1, 2], it is now possible to synthesize/measure absolute optical frequencies with a performance level that before was only achievable by specialized laboratories [3]. This has led to a revolution in different fields, ranging from optical clocks to precision spectroscopy [4]. These applications mainly use mode-locked lasers, whose repetition rates are typically less than 10 GHz. There are other applications (such as optical arbitrary waveform generation, coherent optical communications or radio-frequency photonics) that do not require self-referencing but would benefit from higher repetition rates and smaller sized combs [5]. Recently, a novel platform has emerged with the prospect to achieve these two features simultaneously: the microresonator frequency comb [6].

In this new configuration, a continuous-wave (CW) laser pumps an ultrahigh-Q optical cavity. When the power builds up in the cavity, new frequency components are generated and interact by nonlinear mixing. The first demonstrations used whispering gallery mode resonators made of different materials including silica [7], CaF_2 [8], or MgF_2 [9]. More recently, microresonators were fabricated in planar geometries with high-index glass [10], silicon nitride [11] or AlN [12]. Here, the loaded Q factor of the cavities is lower ($\sim 10^5$–10^6 around 1.5 μm) but the nonlinear coefficients are sufficiently high to yield frequency combs, in some cases with thousands of

#203476 - $15.00 USD Received 26 Dec 2013; revised 8 Feb 2014; accepted 13 Feb 2014; published 20 Feb 2014

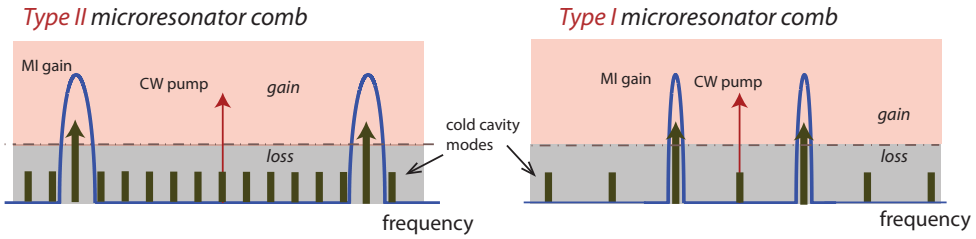

Fig. 1. Modulation instability (MI) is the underlying phenomenon that leads to parametric oscillation in microresonator frequency combs. In Type II combs, the MI sidebands generated by the CW pump lead to parametric growth of frequencies that are several FSRs away. These frequency components grow in power and nonlinear mix with the pump. This microresonator may lead to a spectrally partially coherent comb [29]. However, the comb dynamics can be altered by actively manipulating the CW pump settings in the course of comb formation. This may lead to the formation of stable combs [33, 39] and cavity solitons [42]. We show that these solutions are indeed stable and spectrally coherent, but they strongly depend on the particular initial conditions of the system. For Type I combs, the first oscillating modes are beside the pump and display a spectrally coherent behavior. These solutions are robust to the noise conditions.

modes and a bandwidth spanning tens of terahertz [13], similar to whispering-gallery-mode-based combs [14]. The appeal of microresonator frequency combs is that the repetition rate is governed by the free spectral range (FSR) of the cavity (and can thus be significantly higher than femtosecond mode-locked lasers) and the gain bandwidth is "man-made", in the sense that it can be controlled via dispersion engineering [15–19] within the transparency window of the cavity material [20–22]. In addition, the manufacturing process of microresonators with silicon nitride and high-index material is compatible with CMOS fabrication standards [23] and thus it is not difficult to envision embedding more subsystems onto the same chip with additional engineering effort.

However, before realizing the full potential of this novel platform one must ensure that the requirement of full coherence across the bandwidth is indeed satisfied. Strikingly, recent experiments by Weiner and colleagues [24] and Papp and Diddams [25] revealed that this is not always the case. They focused on getting transform-limited pulses from microresonator combs by line-by-line pulse shaping [26]. Following the nomenclature of [24], there was a clear distinction between the noise performance exhibited by combs where the spectral distance between the CW pump laser and the first oscillating frequencies in the comb corresponded to one (Type I) or more (Type II) cavity's FSRs (see Fig. 1) [24, 27–29]. The former class allows for getting transform-limited pulses after phase compensation: an indirect indication of spectrally coherent behavior. For Type II combs and for certain pump setting conditions, it was not possible to achieve transform-limited pulses. This led to a degradation in the peak to background ratio in the measured autocorrelation trace when compared to the corresponding digitally compressed one [24, 25]. The explanation for this phenomenon was that the spectral phases of the microresonator comb were fluctuating randomly over a certain range (see supplementary information from [24]). Different groups have reported similar observations. Recent multi-heterodyne experiments showed that Type II combs operating in the partially coherent regime do not have a spectrum formed by evenly spaced frequency components, leading to decreased noise performance as inferred by the broadening of the RF beat note of the microresonator comb [29]. An important conclusion is that neither the formation dynamics nor the noise behavior is exclusive of a particular material or geometry [29]. In [25, 28], it was observed that when the RF beat

#203476 - $15.00 USD Received 26 Dec 2013; revised 8 Feb 2014; accepted 13 Feb 2014; published 20 Feb 2014

note appears broadened, the comb light couldn't be temporally compressed. This has a strong implication in optical communications because this apparent lack of spectral coherence leads to degradation in the bit error rate performance when the comb is used as a multiwavelength transmitter [28].

One can find in the literature physical analyses that provide quantitative insight into the formation of microresonator combs [30–39], including approximate analytical [30, 32, 36, 40] and numerical solutions [31], as well as stability studies [33, 37–39]. It has been recognized that the essential physics of the microresonator combs (excluding modal crossing and mechanical and thermal effects) can be described by a master equation [32, 34, 35], mathematically isomorphic to the one derived by Lugiato and Lefever in the framework of spatial solitons and pattern formation in cavities [41]. Likewise, temporal cavity solitons have been observed and analyzed in microresonator frequency combs [42] and fiber-based cavities (see e.g. [43]). Notwithstanding, comparatively few efforts have been devoted towards a better theoretical understanding of the noise formation in general (and the coherence properties in particular) in microresonator frequency combs. This is a challenging task, since a thorough stochastic analysis requires computing thousands of ensemble realizations upon propagation in an instantaneous nonlinear system [44]. However, the random nature of light cannot be ignored since it is at the core of the formation of the microresonator comb. The spontaneous generation of frequency components in the cavity primarily arises by parametric amplification of vacuum fluctuations [30, 40], i.e. modulation instability (MI).

Regarding coherence studies in microresonator combs, Erkintalo and Coen [45] have analyzed numerically the first-order-degree of spectral coherence when the comb is operating under different regimes, which are linked to the solutions of the Lugiato-Lefever equation [38]. They find that stable and coherent spectra can be obtained in Type II combs at either the onset of modulation instability or when cavity solitons are formed [45]. Here, we complement this study by analyzing the connection between spectral coherence and the dynamics of Type I versus Type II microresonator combs. In line with recent observations [24, 25, 27, 28], we also find that Type II combs are coherent as long as the oscillating modes remain incapable to provide net MI gain by themselves. Otherwise, we observe a degradation of the coherence, but only in particular regions of the spectrum. We also find that cavity solitons are stable and spectrally coherent but these solutions are susceptible to the vacuum fluctuations that drive the dynamics of the comb. The most important observation of our work is that Type I combs emerge in a natural manner and are indeed spectrally coherent, regardless of the initial seed conditions. This work highlights the relevance of reporting stability, shot-to-shot fluctuations, spectral coherence and repeatability in microresonator comb experiments.

2. Parametric oscillation revisited in the framework of the Lugiato-Lefever equation

The starting point of the next analysis is the Lugiato-Lefever equation (LLE) [41]. As mentioned in the introduction, this equation has been used previously to describe modulation instability and soliton dynamics in CW-pumped fiber cavities [46–48] and microresonator combs [32, 34, 35]. For the sake of completeness, we summarize here the physics of parametric oscillation that we find more relevant in determining the coherence properties of microresonator combs. More extensive analyses can be found in [32, 36–38, 46].

The LLE reads as

$$t_R \frac{\partial E(t,\tau)}{\partial t} = \left[-\alpha - i\delta_0 + iL \sum_{k\geq 2} \frac{\beta_k}{k!} \left(i\frac{\partial}{\partial \tau} \right)^k + i\gamma L |E(t,\tau)|^2 \right] E(t,\tau) + \sqrt{\theta} E_{\text{in}} \,. \qquad (1)$$

Here, $E(t,\tau)$ describes the complex field envelope inside the ring cavity, with the time τ accounting for waveform variations within the roundtrip time t_R, whereas t is a *slow* time vari-

#203476 - $15.00 USD Received 26 Dec 2013; revised 8 Feb 2014; accepted 13 Feb 2014; published 20 Feb 2014

able related to the field evolution in succesive roundtrips. L is the cavity length; α the loss per roundtrip, i.e. $\alpha = (\alpha_i L + \theta)/2$, with α_i being the propagation loss per unit length, and θ the transmission power coefficient in the cavity coupler; δ_0 is the phase detuning of the CW pump frequency, ω_p, with respect to the closest cavity resonance, ω_0, i.e. $\delta_0 = t_R(\omega_0 - \omega_p)$. The dispersion coefficients are given by β_k, where β_2 is the lowest-order one, describing the group velocity dispersion, and the nonlinear coefficient is γ. Finally, E_{in} accounts for the complex field of the CW pump. The cavity's mean free spectral range is $\text{FSR} = 1/t_R$. It is worth reminding that for low propagation loss and under critical coupling condition, $\alpha = \theta$, the loaded quality factor is related to the roundtrip loss by $Q = \omega_0/(2\alpha\text{FSR})$.

Parametric oscillation in microresonators is analyzed by probing the LLE with the ansatz $E(t,\tau) = a_{(-)}\exp(-i\Omega\tau) + a_0 + a_{(+)}\exp(i\Omega\tau)$ [36, 46], where $a_{(-)}$ and $a_{(+)}$ are much smaller than a_0, and this last term satisfies the optical bistability equation $a_0\left[\alpha + i(\delta_0 - \gamma L P_0)\right] = \sqrt{\theta}E_{\text{in}}$, where $P_0 = |a_0|^2$. It is easy to show that in a first-order-dispersion approximation the LLE presents exponentially growing solutions for $a_{(-)}$ and $a_{(+)}$, proportional to $\exp\left[\Lambda(\Omega)t\right]$ [46]. The gain coefficient is $\Lambda(\Omega) = -\alpha + \sqrt{(\gamma L P_0)^2 - (\Delta\kappa(\Omega))^2}$ and is maximum when the phase-mismatch $\Delta\kappa(\Omega) = \delta_0 - L\beta_2\Omega^2/2 - 2\gamma L P_0$ equals zero. This occurs at the angular frequency [46]

$$\Omega_{\text{m}}^2 = \frac{2}{L\beta_2}\left(\delta_0 - 2\gamma L P_0\right). \tag{2}$$

At this frequency, the modes $a_{(-)}$ and $a_{(+)}$ will experience net gain as long as $P_0 > P_{0,\text{th}} = \alpha/(\gamma L)$, which defines the required power threshold for parametric oscillation. Considering the optical bistability condition, the above threshold for the intracavity power provides the CW pump power needed to achieve parametric oscillation,

$$P_{\text{in,th}} = \frac{1}{\gamma L}\left[\alpha^2 + (\delta_0 - \alpha)^2\right], \tag{3}$$

where critical coupling is assumed. Parametric oscillation in microresonator combs has been previously studied [30, 40]. It is interesting to note that the $1/Q^2$ dependence in the required threshold pump power (see e.g. Eq. (10) in [30]) can alternatively be obtained in the framework of the LLE. In particular, if we take Eq. (3) and consider $\delta_0 = 0$, the pump power threshold becomes $P_{\text{in,th}} = 2\alpha^2/(\gamma L)$, in agreement with [49]. Note that this threshold is different from the absolute parametric threshold, which is given for a fixed pump power when the detuning satisfies [38]

$$\delta_0 \geq \alpha - \sqrt{P_{\text{in}}\gamma L - \alpha^2}. \tag{4}$$

As firstly observed in [24, 27–29], microresonator combs whose first oscillating frequencies appear one FSR away from the pump appear to be stable and admit compressibility to the transform-limited duration [24]. Thus, it is important to assess the design rules that lead to this type of microresonator comb (so-called Type I [24, 27, 28]). From Eq. (2), the Type I condition, i.e. $\Omega_{\text{m}} = 2\pi\text{FSR}$, imposes the dispersion of the cavity to satisfy

$$\beta_2 = \frac{(\delta_0 - 2\gamma L P_0)}{2L\pi^2\text{FSR}^2}. \tag{5}$$

This indicates that, depending on the cavity detuning, either normal or anomalous dispersion may lead to Type I combs. For zero detuning and considering the intracavity power at threshold, $P_{0,\text{th}}$, we get $\beta_2 = -\alpha/(L\pi^2\text{FSR}^2)$ (in close agreement to what is found in [29]), which means that anomalous dispersion is required. Equation (5) can be considered as a generalization for the Type I design rule, where P_0 is not necessarily the intracavity power at threshold.

In the following sections, we shall verify that spectrally coherent combs are achievable for Type I combs. For completeness, these results are benchmarked to the coherence properties of

#203476 - $15.00 USD Received 26 Dec 2013; revised 8 Feb 2014; accepted 13 Feb 2014; published 20 Feb 2014

Type II combs whose detuning is just above the minimum defined by Eq. (4) [45], or temporal cavity solitons.

3. Numerical results

The spectral coherence of microresonator combs is evaluated by means of the following figure of merit [45]

$$|g(\omega;t_1,t_2)| = \frac{\left|\langle \tilde{E}^*(t_1,\omega)\tilde{E}(t_2,\omega)\rangle\right|}{\langle\left|\tilde{E}(\omega)\right|^2\rangle}. \quad (6)$$

Here, the complex field $\tilde{E}(t,\omega)$ is the Fourier transform of $E(t,\tau)$ with respect to τ. The frequency dependence of the two-time correlation function has been widely used to assess the noise performance of different supercontinuum sources [50,51]. Different figures of merit, e.g. the two-frequency correlation function [52] or higher-order correlations [53] can be studied too, but this is a topic beyond the scope of this work.

The brackets above denote ensemble averaging. In practice, we solve Eq. (1) starting from an empty ring. The waveform $E(t,\tau)$ is calculated within the temporal window $-t_R/2 \le \tau \le t_R/2$, and the steps taken in the variable t correspond to a single cavity roundtrip time. Before every step, we load the CW pump with statistically independent noise consisting of one photon per spectral bin with random phase [50, 51]. We calculate the complex degree of coherence at a fixed time difference $t_2 - t_1$ and 1000 different instants t_1 of the evolution time. As demonstrated in [45], for time differences shorter or in the order of the photon lifetime in the cavity, $t_{\rm ph} = t_R/(2\alpha)$, the light source may display coherent behavior even in a regime where the comb is inherently unstable. In order to avoid these artifacts, we choose $t_2 - t_1$ to be more than one order of magnitude longer than $t_{\rm ph}$.

3.1. Example A: Type II microresonator comb

In our first example, the microresonator is designed with FSR $= 226$ GHz, $L = 2\pi r$ with $r = 100\,\mu$m, $\alpha = \theta = 0.003$, $\gamma = 1000\,(\text{W}\cdot\text{km})^{-1}$, $\beta_2 = -48.5$ ps^2/km, $\beta_3 = 0.131$ ps^3/km and $\beta_4 = 0.0025$ ps^4/km. These parameters could be realistically obtained with a silicon nitride microresonator and are similar to the ones reported in [13,35]. We consider a CW pump power of 1.5 W. From Eq. (4), the required detuning for parametric oscillation is $\delta_0 \ge -0.028$. In Fig. 2 we plot the dynamics of the microresonator comb at different detuning values satisfying the above inequality. For values close to the threshold [see Fig. 2(a)], only a few discrete frequency components are generated. In a first step, the pump generates two new frequencies through degenerate four-wave mixing [6, 29], that is the fundamental interaction behind the modulation instability process [54]. The position of these lines corresponds to the frequencies $\pm\Omega_{\rm m}$ given by Eq. (2) and are $\pm 2\pi \times 6.7$ THz in this case, much higher than the cavity's FSR. In a second step, these three frequencies interact through a nondenegerate and stimulated four-wave mixing process. Consequently, new frequencies appear at $\pm 2\Omega_{\rm m}$ and $\pm 3\Omega_{\rm m}$, keeping in this way the equidistance between lines [6, 29]. We observe that the comb evolves towards a stable steady state after several roundtrips. Pulses are formed as soon as the new frequencies emerge. Figure 2(b) displays the comb dynamics for the case in which the CW pump is closer to resonance. Here there is an initial state similar to the case in Fig. 2(a), but the first oscillating modes acquire sufficient power to stimulate the growth of frequency components located between them and the pump through a degenerate four-wave-mixing process [27,29,55]. These new lines generate more frequency components by non-degenerate and stimulated four-wave-mixing processes. In the time domain, the mixing leads to strong intensity variations. Finally, in the case in which the comb is initiated by pumping on resonance, Fig. 2(c), a broader microresonator comb is rapidly obtained, and the spectrum fills quickly all the FSRs between the pump and the first oscillating

#203476 - $15.00 USD Received 26 Dec 2013; revised 8 Feb 2014; accepted 13 Feb 2014; published 20 Feb 2014

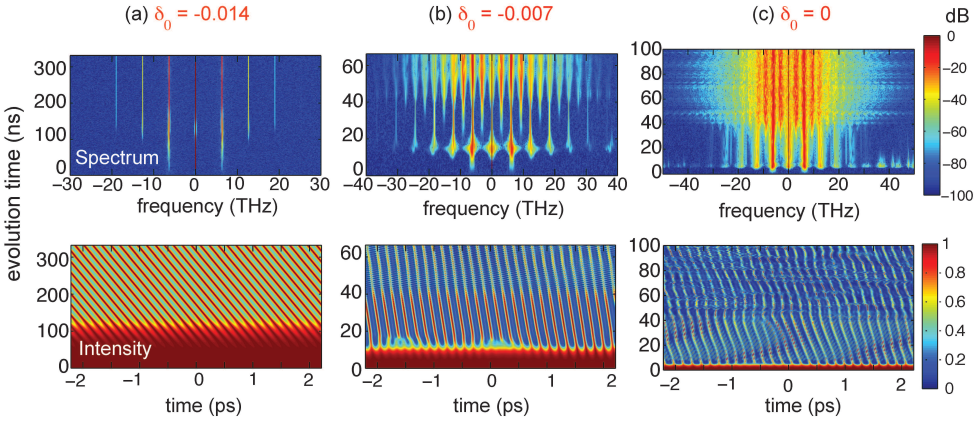

Fig. 2. Dynamics of a Type II microresonator comb in spectral domain (top row) and time domain (bottom row) for different detuning conditions. Corresponding average spectra, shot-to-shot fluctuations and spectral coherence are displayed in Fig. 3.

modes. However, the waveform does not approach a steady state and there are strong spectral and intensity variations from one roundtrip to the next.

We have calculated the spectral coherence for each example above as per Eq. (6) and the results are presented in Fig. 3. For each detuning, the evolution of the waveform over the variable t is calculated over long time distances. As explained before, the coherence is calculated for pairs of spectral waveforms separated $t_2 - t_1 > 10t_{\mathrm{ph}}$. In order to get conclusive statistics, we compute 1000 consecutive pairs. The evolution of the field over time is shown on the left column in Fig. 3. On the right column, the field realizations are superimposed and the average spectrum corresponding to the comb envelope is calculated and shown in pink. For $\delta_0 = -0.014$ in Fig. 3(a), the fluctuations appear only at the background level and the comb displays a spectrally coherent behavior. The MI lines remain highly coherent and stable upon evolution. For detuning values closer to resonance, $\delta_0 = -0.007$ in Fig. 3(b), the spectral regions around the first oscillating modes remain coherent, however the new comb lines that arise in between are partially coherent. One can indeed observe stronger amplitude fluctuations in these spectral regions and conclude that the comb is spectrally partially coherent. Finally, right on resonance, $\delta_0 = 0$ in Fig. 3(c), the spectral envelope of the combs is much smoother but there appear large spectral fluctuations from shot to shot that lead to a degradation of the spectral coherence across the whole bandwidth. These findings are in agreement with the analysis carried out in [45] based on the stability of the LLE solutions.

3.2. *Example B: Type I microresonator comb*

We now consider a slightly different microresonator, with design parameters FSR $= 2.41$ THz, $r = 10\,\mu$m, $\alpha = \theta = 0.001$, $\gamma = 1100\,(\mathrm{W{\cdot}km})^{-1}$ and $\beta_2 = -623.4\,\mathrm{ps}^2/\mathrm{km}$. These parameters are chosen so that Eq. (5) is satisfied at resonance for a CW pump power of 0.2 W. The field evolution is calculated in the same manner as before. Likewise, the complex degree of coherence is computed for a fixed time difference greater than $10t_{\mathrm{ph}}$. The average spectral envelopes and degrees of coherence are displayed in Figs. 4(a)–4(d) for different pump powers but keeping $\delta_0 = 0$.

The comb is always highly coherent in this case. The broadest comb envelope corresponds to the case in which the MI gain peak matches the FSR of the cold cavity, as Fig. 4(e) indicates. Under the spectral envelope figures, we plot the corresponding intensity profile (temporally

#203476 - $15.00 USD Received 26 Dec 2013; revised 8 Feb 2014; accepted 13 Feb 2014; published 20 Feb 2014

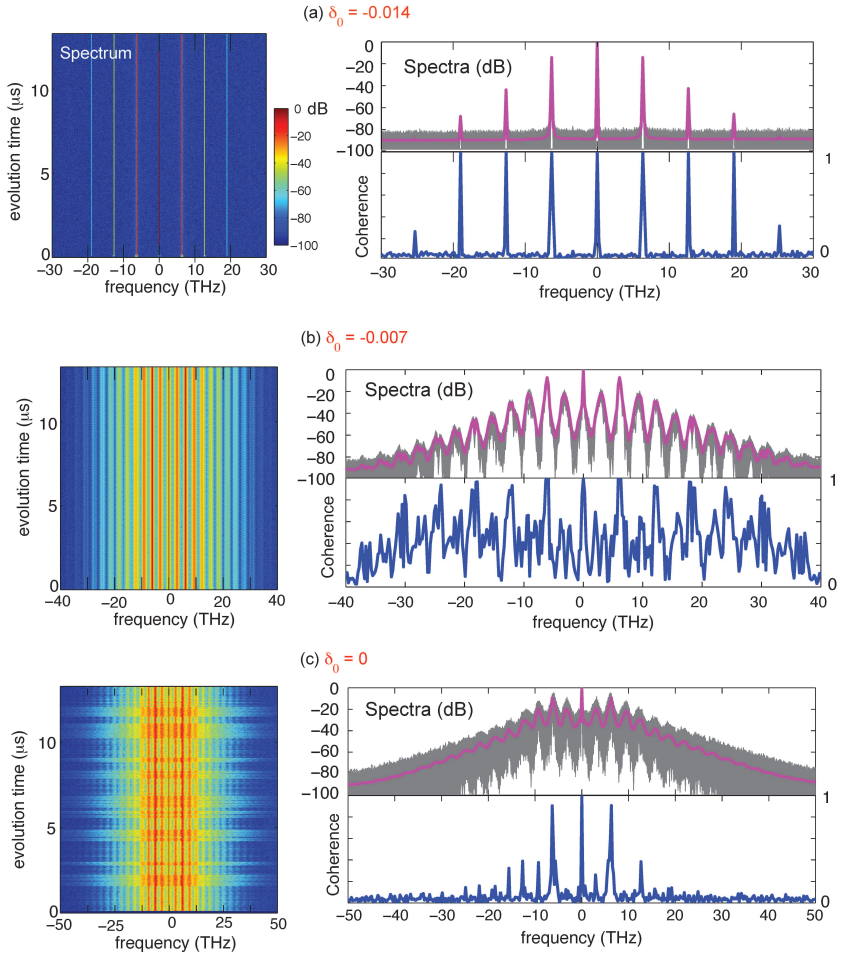

Fig. 3. Spectral coherence and shot-to-shot fluctuations for the microresonator combs in Fig. 2.

shifted for clarity) and compare it to the transform-limited case. For the optimum case in which $P_{\text{in}} = 0.2\,\text{W}$, the pulse is very close to the transform limit. For higher powers [Figs. 4(c) and 4(d)], the pulse deviates from the optimally compressed case, yet the degree of coherence is 1. This means that the spectral phase is not uniform but high-quality ultrashort pulses can be achieved with the aid of a line-by-line pulse-shaping device [24].

It is interesting to investigate whether the system approaches the above steady state regardless of the input noise conditions. To answer this, we compute a slightly different degree of coherence

$$|g_s(\omega;t)| = \frac{\left|\langle \tilde{E}_1^*(t,\omega)\tilde{E}_2(t,\omega)\rangle\right|}{\sqrt{\langle\left|\tilde{E}_1(\omega)\right|^2\rangle\langle\left|\tilde{E}_2(\omega)\right|^2\rangle}}. \tag{7}$$

Here, the pair of waveforms $\tilde{E}_1(t,\omega)$ and $\tilde{E}_2(t,\omega)$ are calculated at a fixed instant time t for different random seeds. We note that this magnitude is conceptually closer to the one considered when evaluating the coherence properties in supercontinuum fiber sources [50, 51], where the

#203476 - $15.00 USD Received 26 Dec 2013; revised 8 Feb 2014; accepted 13 Feb 2014; published 20 Feb 2014

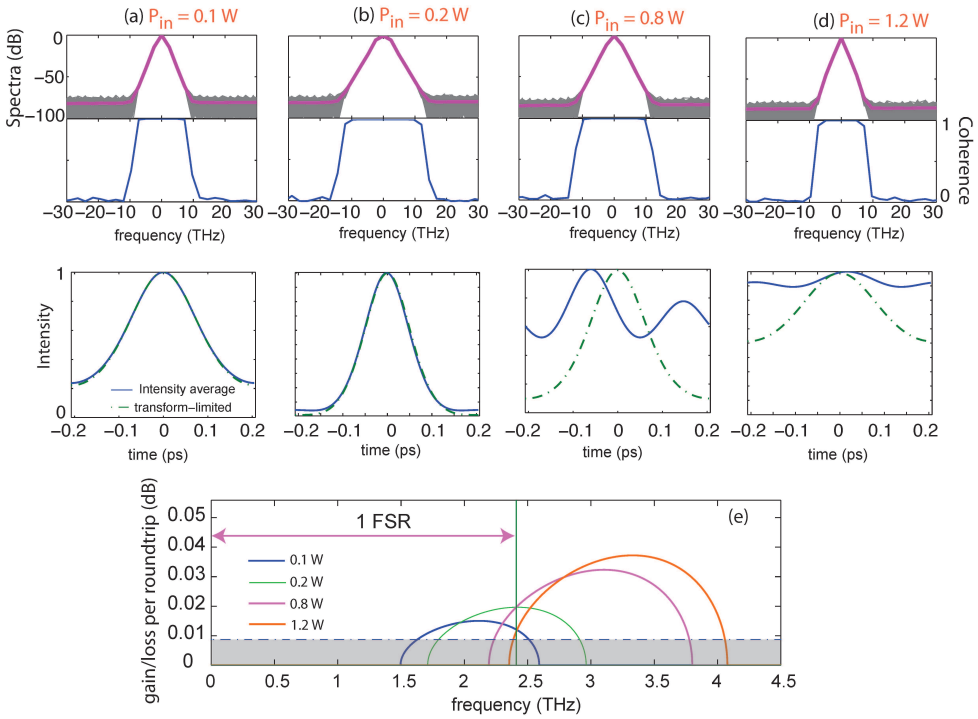

Fig. 4. (a)-(d) Average envelope spectra, degree of coherence and intensity profile for a Type I microresonator comb at different pump power leves. (e) MI gain bandwith shift for different power levels. At 0.2 W the maximum gain coincides with the FSR of the microresonator cavity.

different realizations calculated for the ensemble average are evaluated for a fixed fiber length and considering different random seeds. Our findings are summarized in Fig. 5 for the case of Fig. 4(b). In order to make sure that the system has approached the steady state we are considering $t = 10000\,t_{\mathrm{ph}}$. As in the previous case, we compute 1000 random seeds to calculate the average in Eq. (7). All the spectra are superposed (gray curves) and the average spectrum is shown in pink solid line. We observe that the spectral envelope of the comb remains constant in amplitude and is almost identical to the one calculated by averaging, for a single random seed, over multiple roundtrip times [pink solid line in Fig. 4(b) here displayed as dashed yellow]. However the degree of coherence as defined by Eq. (7), shown in dashed blue curve under the spectrum, indicates a highly incoherent behavior for all the frequency components except for the pump. What occurs is that the pulses achieve the same temporal profile as in Fig. 4(b) but appear randomly delayed within the cavity period for different random seeds. This leads to identical spectra with a linear spectral phase ramp with random slope. When the delay is compensated *offline*, we observe a substantial increase in the spectral coherence as defined by Eq. (7) (blue solid line). This curve indeed matches the degree of coherence as calculated by Eq. (6), which is displayed for completeness in red dashed line in Fig. 5.

The conclusion from the above findings is that, apart from an irrelevant arbitrary delay, Type I combs approach a steady state coherent solution regardless of the input noise seed. As shall be seen in the next section, this conclusion needs to be refined in the context of temporal cavity solitons.

#203476 - $15.00 USD Received 26 Dec 2013; revised 8 Feb 2014; accepted 13 Feb 2014; published 20 Feb 2014

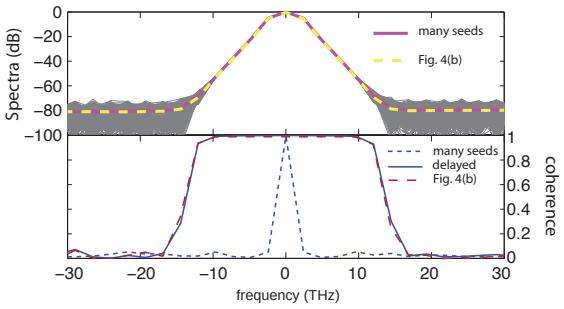

Fig. 5. Analysis of the universality of the stable solutions for Type I coherent combs. (Top) The different realizations calculated at a fixed instant time for different random seeds. (Bottom) the degree of coherence calculated at fixed time t over multiple noise seeds (blue dash curve) is however substantially different when compared to the one calculated at multiple instant times for a fixed seed (red dash curve). After compensating for a linear spectral phase ad hoc, the degree of coherence calculated at a fixed time for various noise seeds (blue solid line) is identical to the degree of coherence calculated for a fixed seed and various instant times.

4. Stability and coherence of temporal cavity solitons

In the examples in the previous section, we have considered the evolution of the system for a fixed pump power and detuning. This is what in the literature is known as the soft excitation regime [33,36]. Notwithstanding, Eq. (1) admits different mathematical solutions that are physically stable too. However, in order to gain access to these states, one must vary dynamically either the pump power or the detuning in the course of comb formation. This is what is called the hard excitation regime [33, 36, 39]. Several groups have reported stable combs achieved in this manner (see, e.g. [13, 29, 56]). One of the more impressive results of stable microresonator combs in this regime corresponds to the case of temporal cavity solitons [42]. The transition towards temporal cavity solitons (CSs) has been also studied numerically [38, 42, 55]. In [38], it was evidenced that the comb evolves from an initial MI stage through a chaotic regime to finally provide temporal CSs. This has been proved numerically by studying the evolution of the comb by inducing abrupt detuning transitions [55]. By analyzing the LLE solutions in the above-mentioned stages, it appears clear that the comb losses spectral coherence in the transition from MI to the chaotic regime, but it recovers the stability after entering the regime where cavity solitons are formed [45].

In this section we study the formation of CSs by solving the LLE. The microresonator parameters are the same as described in Sect. 3.1. For simplicity we keep only the first-order-dispersion. Instead of forcing abrupt changes in detuning parameter, we ramp it in a continuous manner. As in the previous sections, the CW pump and noise are added every roundtrip. This procedure is closer to the experimental implementations, where the laser frequency is swept continuously around the cavity resonance [42]. The programmed dynamic detuning is depicted in Fig. 6(a). We first set $\delta_0 = -0.025$ for a time duration corresponding to $120 t_{\mathrm{ph}}$. The comb remains here in the stable MI stage [as indicated by Eq. (4)]. We then sweep linearly in time the detuning for $120 t_{\mathrm{ph}}$ more until it reaches $\delta_0 = 0.070$. We note that this value lies within the range $3(P_{\mathrm{in}}\gamma L\alpha/4)^{1/3} \leq \delta_0 \leq \pi^2 P_{\mathrm{in}}\gamma L/(8\alpha)$, where CSs are expected to form [38]. This continuous ramping is different to the one evaluated in [55], but as Figs. 6(b) and 6(c) illustrate, we reach the same conclusions: upon the initial MI stage, the comb enters into a chaotic regime, with large spectral broadening but loss of temporal structure. Then, the comb moves towards

#203476 - $15.00 USD Received 26 Dec 2013; revised 8 Feb 2014; accepted 13 Feb 2014; published 20 Feb 2014

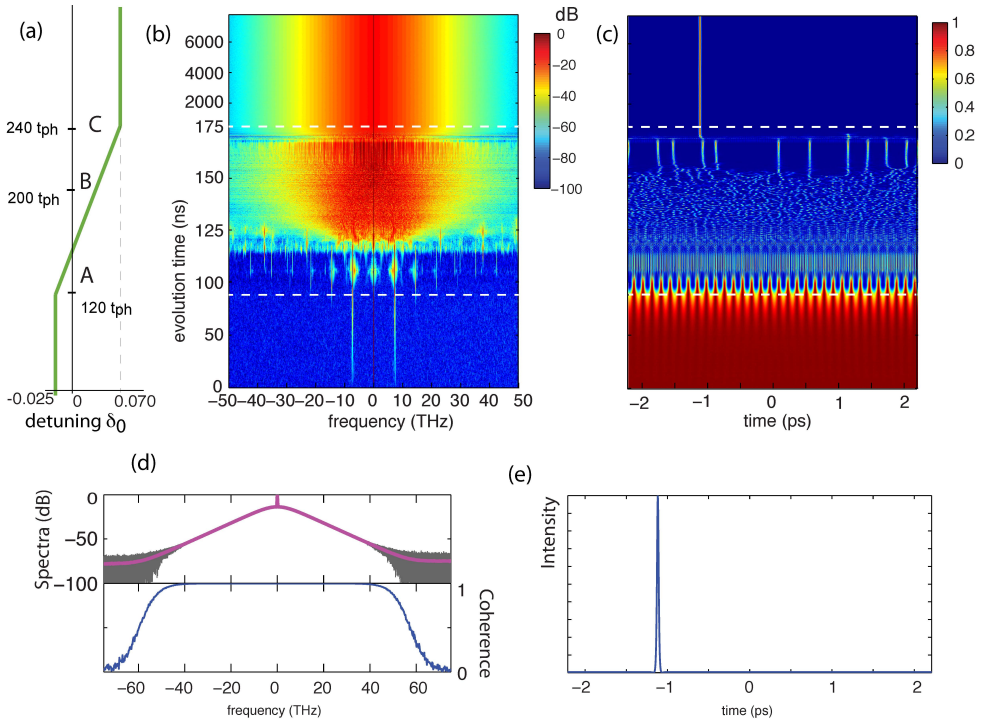

Fig. 6. Temporal cavity soliton formation in microresonators. (a) Dynamic evolution of detuning. Corresponding (b) spectral and (c) time domain evolutions. Note the difference in time scales at different stages. The detuning is changed dynamically in the course of the CS formation. In the first stage, it is kept constant. The points marked as A and C are indicated by the dashed white lines in (b) and (c). Once the cavity soliton is formed, the waveform appears stable and coherent (d). The average intensity indicates a pulse with 25 fs duration (e).

a stage where only a few pulses oscillate per period. After continuous detuning, these waveforms collapse into a stable pulse. In order to get sufficient statistics to calculate the spectral coherence, once this pulse is formed, we let the waveform evolve further in time while keeping the detuning constant. In order to compute Eq. (6), we store 1000 waveforms separated by $10t_{\mathrm{ph}}$ from each other. Snapshots in time and frequency at the relevant regimes are shown in Fig. 7. Our analysis of the spectral coherence reveals that the cavity pulse is highly coherent [Fig. 6(d)], confirming what has been recently found by analyzing the LLE solutions [45].

Next, we are interested in the robustness of this solution for different noise seeds, for which we repeat the above simulation considering the same microresonator parameters, including the sweep and pump power. The only difference now is the set of independent random noise seeds accompanying the CW pump every roundtrip, which is otherwise inaccessible by any experimental means. Interestingly, the system achieves a different steady state consisting of two temporal cavity solitons. This waveform also has a high degree of spectral coherence. Figure 7 compares the relevant waveforms in time and frequency domains obtained at particular instant times for the two sets of noise considered. In the initial MI stage, the waveforms are almost identical, simply shifted in time. However, the waveform achieved in the chaotic stage [indicated as time B in Fig. 7] is different. When the system achieves the steady state, the exact

#203476 - $15.00 USD Received 26 Dec 2013; revised 8 Feb 2014; accepted 13 Feb 2014; published 20 Feb 2014

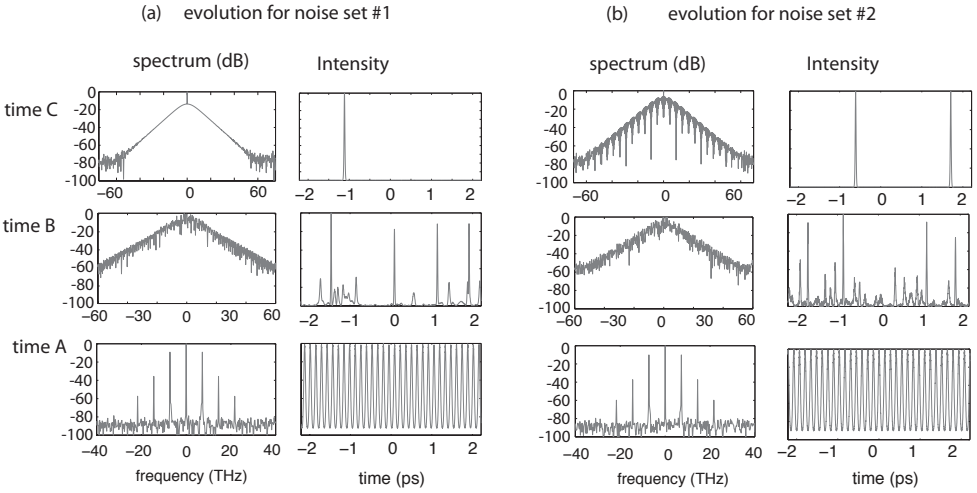

Fig. 7. Analysis of cavity soliton formation under different noise conditions. The sweep and other parameters are identical to those in Fig. 6. The points A-C are indicated in Fig. 6(a).

waveform depends on the set of noise seeds accompanying the pump every roundtrip. In the case presented in Fig. 7(b) it shows two solitons but in other runs the system evolves towards 1, 2, 3, 4, 5 solitons or simply collapses into a continuous wave. We know that the conclusion depends on the particular ramp programmed. Whether the system evolves to a single soliton regardless the noise conditions for an optimal ramp choise is an open question.

Such a fine sensitivity of CSs to the particular noise conditions has been observed experimentally [42] and discussed in [42, 45]. An expression for the maximum number of stationary (non interacting) CSs is provided in [42]. It is important to note [42] that the condition to get a maximum number of solitons equal to 1 coincides with the design rule for Type I microresonators [29].

5. Conclusions and discussion

We have analyzed the spectral coherence of microring resonator combs. There is a strikingly different behavior between Type I and Type II combs. In the soft excitation regime, Type II combs are spectrally coherent just at the onset of parametric oscillation, where only the primary lines oscillate and mix with the CW pump. The spectral coherence is severely degraded when the spectral gap between these lines and the CW pump fills in.

This type of combs may however admit the formation of temporal cavity solitons. This requires operating the microresonator in the hard excitation regime by, e.g., realizing a proper detuning of the CW pump in the course of comb formation. We showed that CSs are spectrally coherent and stable, but their formation is very sensitive to vacuum fluctuations. On the contrary, when the microresonator is designed to provide Type I combs, the system always approaches a steady state, stable, spectrally coherent solution regardless of the noise conditions.

We wish to emphasize that the above are not the only possibilities to achieve microresonator combs operating in a high-coherence state. As recent experiments indicate, stable microresonator combs can be obtained by pumping with a waveform composed of multiple CW waves (parametric seeding) [57], or by placing the microring in a fiber cavity [58]. Other observations leading to low-noise states show features akin to injection locking between ensembles of comb modes [59]. Further numerical and experimental work is needed to understand the spectral co-

#203476 - $15.00 USD Received 26 Dec 2013; revised 8 Feb 2014; accepted 13 Feb 2014; published 20 Feb 2014

herence for these new mechanisms and provide general design rules for self-starting spectrally coherent microresonator combs.

Acknowledgments

Victor Torres acknowledges stimulating discussions with Prof. A. M. Weiner. This work has been partly funded by the Swedish Research Council (VR), by the Plan Nacional I+D+I under the research project TEC2008-05490, Ministerio de Ciencia e Innovación (Spain), and by the Generalitat Valenciana under the grant PROMETEO 2009-077. David Castelló-Lurbe gratefully acknowledges funding from the Generalitat Valenciana (VALi+d predoctoral contract).

#203476 - $15.00 USD Received 26 Dec 2013; revised 8 Feb 2014; accepted 13 Feb 2014; published 20 Feb 2014

Paper IV

Inverse dispersion engineering in silicon waveguides

D. Castelló-Lurbe, V. Torres-Company, and E. Silvestre

to appear in *Journal of the Optical Society of America B*,
Vol. 31, No. 8, August 2014.

Inverse dispersion engineering in silicon waveguides

David Castelló-Lurbe,[1,*] Victor Torres-Company,[2] and Enrique Silvestre[1]

[1] *Departament d'Òptica, Universitat de València, 46100 Burjassot, Spain*

[2] *Department of Microtechnology and Nanoscience (MC2), Chalmers University of Technology, 41296 Gothenburg, Sweden*

compiled: May 22, 2014

We present a numerical tool that searches an optimal cross-section geometry of silicon-on-insulator waveguides given a target dispersion profile. The approach is a gradient-based multidimensional method whose efficiency resides on the simultaneous calculation of the propagation constant derivatives with respect to all geometrical parameters of the structure by using the waveguide mode distribution. The algorithm is compatible with regular mode solvers. As an illustrative example, using a silicon slot hybrid waveguide with 4 independent degrees of freedom, our approach finds ultra-flattened (either normal or anomalous) dispersion over 350 nm bandwidth in less than 10 iterations.

OCIS codes: (130.2035) Integrated optics. Dispersion compensation devices; (130.3120) Integrated optics. Integrated optics devices; (130.4310) Integrated optics. Nonlinear.

1. Introduction

Chromatic dispersion is one of the most important properties that controlls the physical behavior of waveguides in both the linear and nonlinear regimes. Its design is key to achieve high performance in applications such as dispersion compensation [1], parametric amplification [2], wavelength conversion [3, 4], or supercontinuum generation [5, 6]. The waveguide dispersion does not only depend on its constituent materials, but also displays a high sensitivity to changes in the geometry (see e.g. [7]). This is specially true for silicon-on-insulator (SOI) waveguides [2–6, 8]. Here, there is a high-index contrast between materials and exists the possibility to engineer the design at the nanometer scale. These characteristics enable an unprecedented control on the waveguide's dispersion properties.

Algorithms allowing for the optimization of the design are tools of great interest. The most widely spread techniques rely on commercially available software that calculates the dispersion profile given a certain structure. This favors direct optimization methods by trial and error. For example, the zero dispersion can be tuned within the C-band by adjusting the height and width of a strip waveguide [4, 5, 9]. Notwithstanding, there are advanced configurations with multiple geometrical degrees of freedom that allow for a much finer control of the dispersion curve [10–12]. The multidimensional optimization renders impractical the application of the direct methods.

Gradient-based algorithms (GBAs) [13] speed up the convergence process with estimations of the direction in the parameter space (e.g. the cross-section geometries of the waveguide) that lead to the largest improvement of the magnitude to be optimized (e.g. dispersion). Topology optimization is a particular GBA that defines some feature (e.g. the refractive index) of all the sampling points of the cross-section as free parameters. Hence it can manage a great number of degrees of freedom [14]. It has been previously used in nanophotonics design [14] and dispersion compensating fibers [15].

In [16], our group proposed an inverse dispersion engineering approach based on a multi-dimensional gradient algorithm to calculate directly the derivatives of the propagation constant with respect to all the structural parameters of a waveguide in a full vectorial framework. It is worth emphasizing that this result does not rely on any particular technique for solving the wave equation. Certainly, this approach circumvents one of the main disadvantages of direct methods and, therefore, provides results in just a few iterations. Previously, it was succesfully applied in the context of photonic crystal fibers [16, 17]

In this work, we apply this technique to SOI waveguides. Due to its intrinsic high index-contrast, we take special care of the vectorial nature of the problem, since the axial component in electric and magnetic fields can be significant in these waveguides [18]. In the next section, we explain our gradient-based algorithm, paying particular attention to the specific numerical issues related to high-index-contrast waveguides. Section 3 is devoted to the numerical results computed through our procedure, including optimizations under additional constraints, and in section 4 we deal with an analysis of the solutions achieved. Finally, the main conclusions are drawn in section 5.

* david.castello-lurbe@uv.es

2. Gradient-based optimization algorithm

Gradient-based algorithms are the first choice in multidimensional optimization when the derivatives of the fitness function are available [13]. So, with the aim of tackling the dispersion engineering of waveguides, a procedure based in the evaluation of the derivatives of the propagation constant, β, with respect to the design parameters was proposed in [16]. In this section we present a close expression for those derivatives well-functioning even in the case of high-index-contrast waveguides and include a detailed description of their implementation.

For dispersion engineering purposes, a simple definition for the merit function in the optimization procedure is the mean squared of the difference between the group-velocity dispersion (GVD), namely $\beta_2(\omega) = \mathrm{d}^2\beta/\mathrm{d}\omega^2$, of a particular structure represented by p and a target GVD,

$$\chi^2(p) = \frac{1}{N_\omega}\sum_{k=1}^{N_\omega}\left(\beta_2(p;\omega_k) - \beta_2^{\text{target}}(\omega_k)\right)^2, \qquad (1)$$

where $p = (p_1, \ldots, p_N)$ is the set of parameters defining the waveguide degrees of freedom. This expression corresponds to the variance of the dispersion with respect to the target dispersion profile in the frequency range of design, and the optimum configuration will correspond to the minimum of χ^2.

In order to reach that minimum, we follow a sequential linear programming (SLP) strategy for producing a series of quadratic problems to be minimized. To be more precise, given a point in the parameter space, $p_{(m)}$, we can obtain the linear approximation of $\beta_2(p)$ around it,

$$\beta_2^{\text{lin}}(p;\omega) = \beta_2(p_{(m)};\omega) + \partial_p\beta_2(p_{(m)};\omega)\cdot(p - p_{(m)}), \quad (2)$$

and, accordingly, a local (quadratic) approximation of the actual merit function,

$$\chi^2_{\text{loc}}(p) = \frac{1}{N_\omega}\sum_{k=1}^{N_\omega}\left(\beta_2^{\text{lin}}(p;\omega_k) - \beta_2^{\text{target}}(\omega_k)\right)^2. \qquad (3)$$

Thus, if $\partial_p\beta_2$ is known, χ^2_{loc} can be built, and its minimum, $p_{(m+1)}$, can be easily determined with no additional computational effort. This new point is expected to be closer to the target and can be used as the starting point in a new iteration of the procedure.

In appendix A, we go one step further than [16] and derive the following expression for the gradient of the propagation constant in the parameter space,

$$\partial_p\beta = \frac{\epsilon_0\omega}{2}\frac{\displaystyle\int_S \left(-\mathbf{e}_\mathrm{t}\cdot(\partial_p\epsilon_{\mathrm{tt}})\mathbf{e}_\mathrm{t} + (\partial_p\epsilon_{zz})e_z^2\right)\mathrm{d}S}{\displaystyle\int_S (\mathbf{e}_\mathrm{t}\times\mathbf{h}_\mathrm{t})\cdot\hat{\mathbf{z}}\,\mathrm{d}S}, \qquad (4)$$

where integrals extend to all the transverse domain where fields are defined, S, and involve components of the electromagnetic field and derivatives of the dielectric tensor. The subscript t indicates transverse components, ϵ_0 is the permittivity of the vacuum and ω is the light frequency. It is worth emphasizing a couple of points around Eq. (4). On the one hand, $(\partial_p\epsilon_{zz})e_z^2$ is the explicit contribution of the vector nature of the electromagnetic field and must be taken into account for high-index-contrast waveguides [18]. On the other hand, Eq. (4) enables the calculation of $\partial_p\beta$ by means of the mode fields of the waveguide at only one parameter configuration. This means that there is no need to know the propagation constant at any other point $p+\delta p$ of the multidimensional parameter space to compute its derivatives.

If we focus on geometrical parameters defining waveguides composed by homogeneous materials, a smoothed effective dielectric tensor, $\hat{\epsilon}$, should be used [19]. This description of the material distribution allows us to evaluate these derivatives in an easy way, avoiding infinities at the discontinuities, whereas derivatives are nonzero only near interfaces. This tensor $\hat{\epsilon}$ must be defined at each spatial sampling point, according to the effective-medium theory [20], as explained in appendix B.

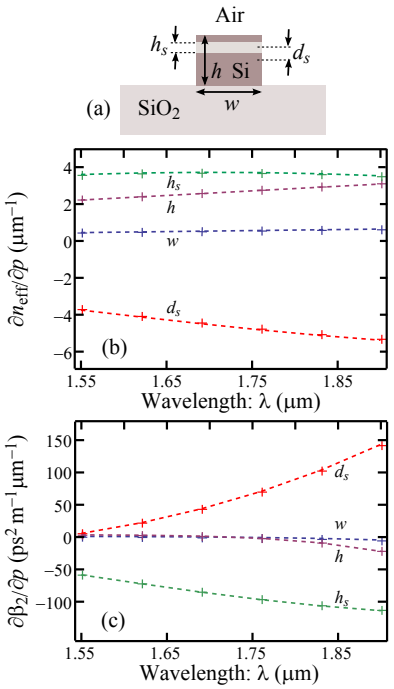

Fig. 1. (a) Outline of the slot waveguide under study [11]. Comparison of the derivatives of the effective refractive index (b) and the group-velocity-dispersion parameter (c) with respect to the geometrical parameters h, w, h_s and d_s, shown in (a), calculated numerically (dashed curves) and by the Eq. (5) (crosses).

Accurate calculations for high-index-contrast waveguides

From the numerical point of view and taking into account the discretization of the integration domain, S, the integral in the numerator of Eq. (4) can present a considerable error in its evaluation owing to the strong discontinuity around the interface of the normal component of the electric field. That difficulty can be overcome if we choose a local basis for the electric field defined by the unit vectors $(\hat{\mathbf{n}}, \hat{\mathbf{T}}, \hat{\mathbf{z}})$: the normal and the tangent to the interface in the transverse plane, $\hat{\mathbf{n}}$ and $\hat{\mathbf{T}}$, and the propagation direction, $\hat{\mathbf{z}}$. In this basis, Eq. (4) can be rewritten as

$$\partial_p \beta = \frac{\epsilon_0 \omega}{2} \frac{\int_S \left((\partial_p \epsilon_{nn}^{-1}) d_n^2 - (\partial_p \epsilon_{TT}) e_T^2 + (\partial_p \epsilon_{zz}) e_z^2 \right) \mathrm{d}S}{\int_S (\mathbf{e}_\mathrm{t} \times \mathbf{h}_\mathrm{t}) \cdot \hat{\mathbf{z}} \, \mathrm{d}S}, \tag{5}$$

where d_n is the component of the electric displacement field normal to the interface and e_T is the component of the electric field tangent to the interface in the transverse plane. It is worth remembering that the dielectric tensor is diagonal in the new local basis since the effective medium around the interface corresponds to a uniaxial anisotropic medium [19], and its extraordinary axis is normal to the interface (parallel to $\hat{\mathbf{n}}$). Therefore, Eq. (5) extends the applicability of Eq. (4) to high-index-constrast waveguides.

In order to check the numerical precision of Eq. (5), we consider a silicon strip waveguide with a horizontal silica slot proposed in [11] by Zhang et al., which is shown in Fig. 1(a). These waveguides present four geometrical degrees of freedom, which we define as the width of the waveguide (w), the height of the waveguide (h), the height of the slot (h_s) and the position of the slot center with respect to the waveguide center (d_s). This is a computationally demanding structure owing to the narrow low-index layer in the middle of a high-index strongly-confining waveguide, near the maximum of field density. Indeed, the light-guiding mechanism of the transverse magnetic (TM) mode (vertically polarized) of this kind of waveguide induces a strong change on the normal component of the electric field at the slot lower interface [11]. Let us consider the following arbitrary configuration: $w = 650\,\mathrm{nm}$, $h = 460\,\mathrm{nm}$, $h_s = 50\,\mathrm{nm}$ and $d_s = 115\,\mathrm{nm}$. We calculate the propagation constant and the fields of the TM mode using an iterative two-dimensional procedure [21] within a squared sampling window of $1.8\,\mu\mathrm{m}$ long and a sampling distance of $6.25\,\mathrm{nm}$. Furthermore, if a sampling grid parallel to the structure were used, the derivatives would then be highly sensitive to the position of the sampling points around the slot horizontal interfaces. To deal with this numerical problem, we rotate the structure slightly (1.5°) with respect to the sampling grid. In Fig. 1(b), we compare results from Eq. (5) with those computed numerically (in particular, solving the wave equation also for neighbor configurations by changing the initial value of each parameter by $\pm 0.5\,\mathrm{nm}$ and $\pm 1.0\,\mathrm{nm}$, fitting the results to a second order polinomial, and calculating its derivative at the initial point). We can observe that the analytical derivatives are in very good agreement with the numerical calculations.

Equation (5) allows us to easily compute the first derivatives of β and engineer magnitudes that depend algebraically on β. Nevertheless, there is no closed expression for calculating higher-order derivatives in a straighforward manner [21]. Despite this, if we are interested in optimizing the chromatic dependency of a derivative of β, we just need to evaluate Eq. (5) for different frequencies, fit those data as a function of ω and perform successive derivatives with respect to frequency. This approach is fast and, as can be appreciated in Fig. 1(c), keeps a high accuracy.

Table 1. Geometrical parameters and merit function after convergence for the five dispersion targets shown in Fig. 2.

$\beta_2^{\mathrm{target}}$ ($\mathrm{ps^2 m^{-1}}$)	iter.	χ ($\mathrm{ps^2 m^{-1}}$)	w (nm)	h (nm)	h_s (nm)	d_s (nm)
(a) +0.0	4	0.018	788	504	42	110
(b) −0.2	8	0.011	634	547	42	114
(c) +0.2	8	0.012	840	599	40	108
(d) −0.8	6	0.052	665	537	51	129
(e) +0.8	9	0.042	887	518	39	93

3. Numerical results

We illustrate our approach in Fig. 2, where we plot five different examples of the optimization processes with different flattened dispersion profiles over 350 nm, in the range $1.55\,\mu\mathrm{m} \leq \lambda \leq 1.90\,\mu\mathrm{m}$ as target, namely, $\beta_2(\omega) = 0$, ± 0.2 and $\pm 0.8\,\mathrm{ps^2 m^{-1}}$. For all five cases, we start from the same waveguide configuration [11], hence showing this choice is not particularly relevant. It corresponds to the geometry used to test the accuracy of the analytical derivatives in the previous section, whose dispersion is far from being flattened. In our simulations, we describe the refractive index of silicon and silica using the Sellmeier coefficients provided in [22]. In these examples, 6 wavelengths in the above range are considered as the points used for evaluating the local approximation of the merit function [Eq. (3)].

It is worth noting that the target curves are recovered to different extent. In other words, the achievable minimum of χ^2 depends on the target curve and on the waveguide's degrees of freedom. In order to ensure that the procedure converges properly, it is convenient to moderate the speed of convergence. In Fig. 3, the evolution of the parameters at each step along the procedure is shown, in which we have allowed variations up to 10 % in each step and we consider the process has converged when the difference of χ between two successive steps is smaller than $0.001\,\mathrm{ps^2 m^{-1}}$. The specific designs obtained after convergence are indicated in Table 1. Note that, for the $\beta_2 = 0$ case, the slot parameters, which are the most sensitive ones [see Fig. 1(c)], are in close

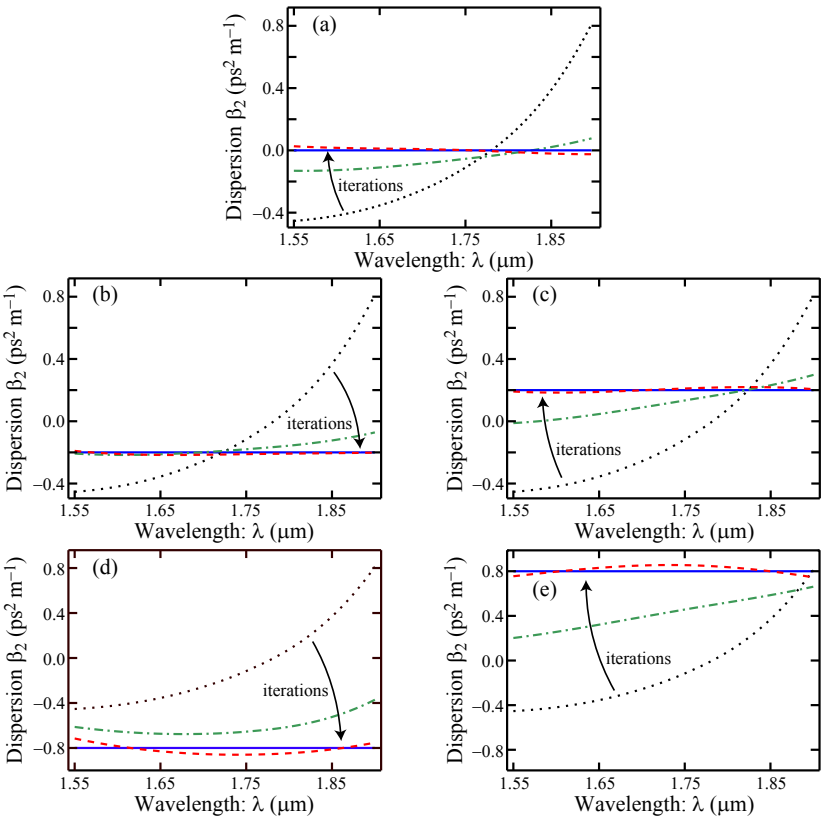

Fig. 2. Five examples of optimization starting from the same geometry (dotted black curve, see details in the text) and with five different flattened dispersion profiles as a goal (solid blue line), namely, low and anomalous (a), low and normal (b), high and anomalous (c) and high and normal (d). Dispersion profiles between the first iteration (dotted-dashed green curve) and the last one (dashed red line) are omitted.

agreement with those reported in [12], where $h_s = 40\,\text{nm}$ and $d_s = 104\,\text{nm}$. We emphasize that curves close to the target are found in a few steps (see Fig. 3). It illustrates the efficiency of this approach compared to trial-and-error methods.

Since Eq. (1) has been defined in this work for engineering β_2, other magnitudes can be altered during the optimization process. In the cases shown in Fig. 2, for instance, the effective refractive index grows as β_2 approaches its target and, therefore, modes become more confined. The effective index behavior is associated to the fact of being positive its derivatives with respect to the height of the waveguide and this parameter has been increased along the processes [see Figs. 1(a) and 3].

Inclusion of feasibility restrictions

The manufacturing of integrated waveguides is, of course, constrained to the limitations of the fabrication method. Therefore, any realistic design procedure must include this kind of additional requirements. Our algorithm also allows us to deal with these fabrication restrictions. They are implemented as constraints in the variables of the local merit function, χ_{loc}, i.e., limiting the possible values of p or bounding them.

The dispersion profile is more sensitive to those parameters related to the slot [see Fig. 1(c)]. So, to illustrate the possibility of including some constraints in our algorithm, we have imposed a lower boundary of 45 nm to the slot height in the optimization processes of Fig. 2. The dispersion profiles obtained under such a condition are shown in Fig. 4. Of course, the impact of this constraint depends on each case. In our examples, it affects the two cases of normal dispersion in a greater extent (see results in Fig. 4), since such cases show the narrowest slots in the unrestricted optimization (see Table 1).

4. Analysis of tolerances

In this work, we have engineered the dispersion profile of SOI waveguides in an efficient way, implementing a

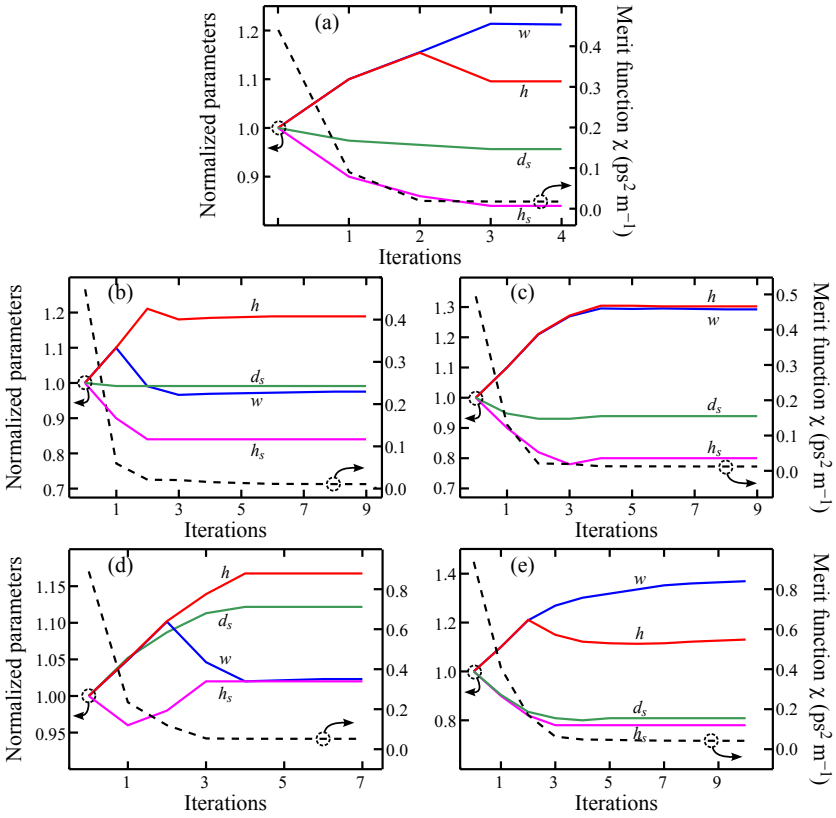

Fig. 3. Plot of the evolution of the geometrical parameters during the optimization procedure of the same five examples shown in Fig. 2, normalized to its starting values (solid colored curves, left-hand axis). Dashed black curves represent the evolution of the square root of the merit function, the standard deviation of β_2 with respect to the target in the design frequency range (right-hand axis).

powerful differential tool that allows us to evaluate, with no additional computational effort, the gradient of the propagation constant in the parameter space. We used a kind of slot waveguide proposed by Zhang et al. [11, 12] to illustrate our inverse dispersion engineering proposal. Nonetheless, we cannot omit the practical interest of the specific structures obtained applying our tool. For example, the cross-section designs that provide the dispersion curves of Figs. 2(a–c) could have applications for soliton formation in optical microresonators [23] or coherent ultraflat supercontinuum generation [12, 17], whereas the dispersion profiles shown in Figs. 2(d,e) could be used for dispersion compesation of ultrashort pulses [1]. In this sense, a crucial point to test the feasibility of any design is to know how it performs facing inevitable changes with respect to the optimized structure. To this end, and for the sake of completeness, we characterize in this section the sensitivity of the waveguides shown in Fig. 3 to fabrication tolerances. In addition, note that our approach also allows to analytically evaluate the uncertainty of the effective index or the dispersion due to the fabrication tolerances by using the standard technique of propagation of errors (see e.g. [16]).

In Fig. 5 the effect of small perturbations of the geometrical parameters on dispersion curves is represented. We take the geometry obtained by means of the optimization process shown in Fig. 2(b) as reference. Since current integrated waveguides can be fabricated with typical tolerances of a few nanometers [24], we have increased and decreased by 2 nm the parameters of that structure. As expected from Fig. 1(c), the GVD is more sensitive to changes that affect the slot compared to perturbations of the strip.

5. Summary

The physical properties of subwavelength waveguides are highly dependent on its geometry due to their small dimensions and high index contrasts. This feature becomes an advantage as long as their cross section can be

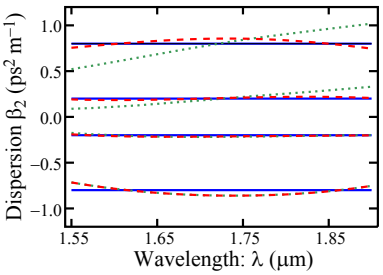

Fig. 4. The last four target (solid blue lines) and optimized (dashed red curves) dispersion profiles shown in Fig. 2 together with those obtained under the restriction $h_s \geq 45\,\mathrm{nm}$ (dotted green curves).

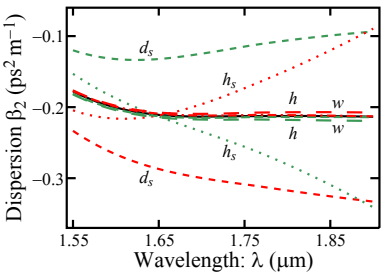

Fig. 5. Plot of the dispersion profiles corresponding to the optimized geometry for the system described in Fig. 2(b) (solid black curve, see details in the text); and the same geometry with each one of the design parameters (h, w, h_s and d_s) increased (red lines) or decreased (green lines) by 2 nm.

suitably designed. Usually, optimum waveguide designs are found by varying separately the geometrical degrees of freedom in their transverse planes. Consequently, this trial-and-error procedure becomes much more challenging when one considers advanced designs containing multiple degrees of freedom.

In this work, we overcome this issue by means of an inverse dispersion engineering approach. Given a target for the dispersion curve, we can simultaneously modify all geometrical parameters of the waveguide towards new values where the structure shows dispersion profiles closer to the target. In this way, in a few iterations we find specific structures with dispersion curves matching, as much as possible, the target. The key fact is the possibility of computing the gradient of the propagation constant with respect to all the geometrical parameters by means of the information provided by the analysis of only one geometry. In addition, our algorithm is compatible with any wave equation solver, since it only needs the information of the mode fields.

Appendix A: Derivative of the propagation constant

Let us write the two-dimensional wave equation for the transverse components of the magnetic field of a mode in a waveguide [16],

$$L\,\mathbf{h}_\mathrm{t} = \left\{\nabla_\mathrm{t}\nabla_\mathrm{t}^\mathrm{T} + \eta\epsilon_\mathrm{tt}\eta^\mathrm{T}\frac{\omega^2}{c^2} - \eta\epsilon_\mathrm{tt}\nabla_\mathrm{t}\left[\epsilon_{zz}^{-1}\nabla_\mathrm{t}^\mathrm{T}\eta\right]\right\}\mathbf{h}_\mathrm{t} = \beta^2\mathbf{h}_\mathrm{t}, \tag{A1}$$

where the subscript t indicates transverse components, the superscript T refers to the transpose of a matrix or vector, ϵ is the — effective — dielectric tensor [19], and η represents the completely antisymmetric tensor in two dimensions, $[(0,+1),(-1,0)]$. The above equation can be recognized as an eigenproblem and therefore the Hellmann-Feynman theorem [25] could be used for calculating derivatives of its eigenvalues. This strategy has been applied in solving electromagnetic problems in cavities, where eigenvalues are the resonant frequencies [14, 26]. However, as the operator L defined by the left-hand side of Eq. (A1) is non-self-adjoint (*cf.* [15], where polarization effects are discarded, and L becomes self-adjoint), a generalization based on biorthogonality [27] must be used. The general expression for this mathematical problem turns out to be [16]

$$\frac{\partial(\beta^2)}{\partial p} = \frac{\langle\tilde{\mathbf{h}}_\mathrm{t}|(\partial_p L)\mathbf{h}_\mathrm{t}\rangle}{\langle\tilde{\mathbf{h}}_\mathrm{t}|\mathbf{h}_\mathrm{t}\rangle}, \tag{A2}$$

where $p = (p_1,\ldots,p_N)$ are the parameters defining the waveguide, $\tilde{\mathbf{h}}_\mathrm{t}$ is the eigenvector of the adjoint operator of L whose eigenvalue is the complex conjugate of β^2 [i.e., $L^\dagger\tilde{\mathbf{h}}_\mathrm{t} = (\beta^2)^*\tilde{\mathbf{h}}_\mathrm{t}$] and therefore $\tilde{\mathbf{h}}_\mathrm{t} = \eta\mathbf{e}_\mathrm{t}^*$, being $\mathbf{e}_\mathrm{t}$ the transverse components of the electric field of the considered waveguide mode [27]. $\langle\circ|\circ\rangle$ stands for the standard scalar product for complex vector functions. It is worth recalling that only the elements explicitly dependent on any p_k contribute to the derivation of L.

In order to derive Eq. (4) from Eq. (A2), first we explicitly write the numerator on the right-hand side in Eq. (A2),

$$\langle\tilde{\mathbf{h}}_\mathrm{t}|(\partial_p L)\mathbf{h}_\mathrm{t}\rangle = \int_S \mathrm{d}S\Big(\frac{\omega^2}{c^2}\mathbf{e}_\mathrm{t}^\mathrm{T}(\partial_p\epsilon_\mathrm{tt})\eta^\mathrm{T}\mathbf{h}_\mathrm{t} - \mathbf{e}_\mathrm{t}^\mathrm{T}(\partial_p\epsilon_\mathrm{tt})\nabla_\mathrm{t}\left[\epsilon_{zz}^{-1}\nabla_\mathrm{t}^\mathrm{T}\eta\mathbf{h}_\mathrm{t}\right] - \mathbf{e}_\mathrm{t}^\mathrm{T}\epsilon_\mathrm{tt}\nabla_\mathrm{t}\left[(\partial_p\epsilon_{zz}^{-1})\nabla_\mathrm{t}^\mathrm{T}\eta\mathbf{h}_\mathrm{t}\right]\Big). \tag{A3}$$

Let us consider now the following Maxwell equations

$$\nabla\times\mathbf{H} = -i\sqrt{\frac{\epsilon_0}{\mu_0}}\frac{\omega}{c}\epsilon\mathbf{E}, \tag{A4}$$

$$\nabla\times\mathbf{E} = i\sqrt{\frac{\mu_0}{\epsilon_0}}\frac{\omega}{c}\mathbf{H}, \tag{A5}$$

$$\nabla\cdot\mathbf{D} = 0. \tag{A6}$$

If we separate the transverse and longitudinal fields components, $\mathbf{E} = (\mathbf{e}_\mathrm{t} + e_z\,\hat{\mathbf{z}})\exp(i\beta z)$ and $\mathbf{H} = (\mathbf{h}_\mathrm{t} +$

$h_z\,\hat{\mathbf{z}})\exp(i\beta z)$, we obtain

$$\nabla_{\rm t}^{\rm T}\eta\mathbf{h}_{\rm t} = -i\sqrt{\frac{\epsilon_0}{\mu_0}}\frac{\omega}{c}\epsilon_{zz}e_z, \tag{A7}$$

$$\nabla_{\rm t}e_z = -i\sqrt{\frac{\mu_0}{\epsilon_0}}\frac{\omega}{c}\eta\mathbf{h}_{\rm t} + i\beta\mathbf{e}_{\rm t}, \tag{A8}$$

$$\nabla_{\rm t}^{\rm T}(\epsilon_{\rm tt}\mathbf{e}_{\rm t}) = -i\beta\epsilon_{zz}e_z, \tag{A9}$$

from Eqs. (A4), (A5) and (A6), respectively. If we take into account Eqs. (A7) and (A8), we can simplify the second term on the right-hand side in Eq. (A3),

$$\begin{aligned}-\int_S {\rm d}S\ \mathbf{e}_{\rm t}^{\rm T}(\partial_p\epsilon_{\rm tt})\nabla_{\rm t}\left[\epsilon_{zz}^{-1}\nabla_{\rm t}^{\rm T}\eta\mathbf{h}_{\rm t}\right]\\ = -\int_S {\rm d}S\ \mathbf{e}_{\rm t}^{\rm T}(\partial_p\epsilon_{\rm tt})\left[-\frac{\omega^2}{c^2}\eta\mathbf{h}_{\rm t} + \epsilon_0\omega\beta\mathbf{e}_{\rm t}\right].\end{aligned} \tag{A10}$$

Next, by using Eqs. (A7) and (A9) and integrate by parts the third term on the right-hand side in Eq. (A3), we find

$$\begin{aligned}-\int_S {\rm d}S\ \mathbf{e}_{\rm t}^{\rm T}\epsilon_{\rm tt}\nabla_{\rm t}\left[(\partial_p\epsilon_{zz}^{-1})\nabla_{\rm t}^{\rm T}\eta\mathbf{h}_{\rm t}\right]\\ = \epsilon_0\omega\beta\int_S {\rm d}S\ (\partial_p\epsilon_{zz})e_z^2.\end{aligned} \tag{A11}$$

Finally, Eq. (4) is directly derived using Eqs. (A10) and (A11).

Appendix B: Effective dielectric tensor

Permittivity is a space averaged magnitude involving microscopic parameters [28]. At the interface the averages only change softly, ensuring smooth transitions between media [20]. This description avoids unphysical discontinuities that would otherwise be detrimental for the numerical algorithms [19].

Following [19, 20], let us consider an interface between two homogeneous media of permittivities ϵ_1 and ϵ_2. On the one hand, components of the dielectric tensor affecting the electric field parallel to the interface must be calculated as a weighted average of the permittivities, $\langle\epsilon\rangle = f_1\epsilon_1 + f_2\epsilon_2$. On the other hand, components of the dielectric tensor acting on the electric field normal to the interface must be computed as the inverse of a weighted average of the inverse permittivities, $\langle 1/\epsilon\rangle = f_1/\epsilon_1 + f_2/\epsilon_2$. The weight functions f_a at each sampling point are evaluated in this work as the relative volume occupied by the ath material in a sphere of radius equal to the sampling distance centered at each sampling point. Finally, the effective dielectric tensor can be written as [19]

$$\hat{\epsilon} = \frac{1}{\langle 1/\epsilon\rangle}P + \langle\epsilon\rangle(I - P), \tag{B1}$$

where I is the identity matrix, and P is the projection matrix onto the normal to the interface, $\hat{\mathbf{n}}$, i.e., $P_{ij} = \hat{n}_i\hat{n}_j$. It is worth noting that, far from the interfaces, $\hat{\epsilon}$ is a multiple of the identity, recovering the original values for the permittivities, ϵ_1 or ϵ_2.

Acknowledgments

This work was financially supported by the Plan Nacional I+D+i under the research project TEC2008-05490, Ministerio de Ciencia e Innovación (Spain), and by the Generalitat Valenciana under the grant PROMETEO 2009-077. Victor Torres acknowledges funding from the Swedish Research Council (VR). D. C.-L. gratefully acknowledges funding from the Generalitat Valenciana (VALi+d predoctoral contract). D. C.-L. and E. S. acknowledge programming tasks by Tomás Castelló Rodríguez and Miguel Gea Milvaques.

References

[1] N. Ishikura, R. Hosoi, R. Hayakawa, T. Tamanuki, M. Shinkawa, and T. Baba, "Photonic crystal tunable slow light device integrated with multi-heaters", Appl. Phys. Lett. **100**, 221110 (2012).

[2] M. A. Foster, A. C. Turner, J. E. Sharping, B. S. Schmidt, M. Lipson, and A. L. Gaeta, "Broad-band optical parametric gain on a silicon photonic chip", Nature **441**, 960–963 (2006).

[3] A. C. Turner-Foster, M. A. Foster, R. Salem, A. L. Gaeta, and M. Lipson, "Frequency conversion over two-thirds of an octave in silicon nanowaveguides", Opt. Express **18**, 1904–1908 (2010).

[4] X. Liu, B. Kuyken, G. Roelkens, R. Baets, R. M. Osgood Jr., and W. M. J. Green, "Bridging the mid-infrared-to-telecom gap with silicon nanophotonic spectral translation", Nature Photon. **6**, 667–671 (2012).

[5] L. Yin, Q. Lin, and G. P. Agrawal, "Soliton fission and supercontinuum generation in silicon waveguides", Opt. Lett. **32**, 391–393 (2007).

[6] R. Halir, Y. Okawachi, J. S. Levy, M. A. Foster, M. Lipson, and A. L. Gaeta, "Ultrabroadband supercontinuum generation in a CMOS-compatible platform", Opt. Lett. **37**, 1685–1687 (2012).

[7] A. Ferrando, E. Silvestre, P. Andrés, J. J. Miret, and M. V. Andrés, "Designing the properties of dispersion-flattened photonic crystal fibers", Opt. Express **9**, 687–697 (2001).

[8] X. Liu, W. M. J. Green, X. Chen, I-W. Hsieh, J. I. Dadap, Y. A. Vlasov, and R. M. Osgood Jr., "Conformal dielectric overlayers for engineering dispersion and effective nonlinearity of silicon nanophotonic wires", Opt. Lett. **33**, 2889–2891 (2008).

[9] A. C. Turner, C. Manolatou, B. S. Schmidt, M. Lipson, M. A. Foster, J. E. Sharping, and A. L. Gaeta, "Tailored anomalous group-velocity dispersion in silicon channel waveguides", Opt. Express **14**, 4357–4362 (2006).

[10] S. Mas, J. Caraquitena, J. V. Galán, P. Sanchis, and J. Martí, "Tailoring the dispersion behavior of silicon nanophotonic slot waveguides", Opt. Express **18**, 20839–20844 (2010).

[11] L. Zhang, Y. Yue, R. G. Beausoleil, and A. E. Willner, "Flattened dispersion in silicon slot waveguides", Opt. Express **18**, 20529–20534 (2010).

[12] L. Zhang, Q. Lin, Y. Yue, Y. Yan, R. G. Beausoleil, and A. E. Willner, "Silicon waveguide with four zero-dispersion wavelengths and its application in on-chip octave-spanning supercontinuum generation", Opt. Express **20**, 1685–1690 (2012).

[13] W. H. Press, S. A. Teukolsky, W. T. Vetterling, and B. P. Flannery, *Numerical Recipes*, 3rd ed. (Cambridge, 2007).
[14] S. Jensen and O. Sigmund, "Topology optimization for nano-photonics", Laser Photon. Rev. **5**, 308–321 (2011).
[15] Jesper Riishede and Ole Sigmund, "Inverse design of dispersion compensating optical fiber using topology optimization," J. Opt. Soc. Am. B **25**, 88–97 (2008).
[16] E. Silvestre, T. Pinheiro-Ortega, P. Andrés, J. J. Miret, and A. Coves, "Differential toolbox to shape dispersion behavior in photonic crystal fibers", Opt. Lett. **31**, 1190–1192 (2006).
[17] J. J. Miret, E. Silvestre, and P. Andrés, "Octave-spanning ultraflat supercontinuum with soft-glass photonic crystal fibers", Opt. Express **17**, 9197–9203 (2009).
[18] S. Afshar V. and T. M. Monro, "A full vectorial model for pulse propagation in emerging waveguides with subwavelength structures part I: Kerr nonlinearity", Opt. Express 17, 2298–2318 (2009).
[19] S. G. Johnson and J. D. Joannopoulos, "Block-iterative frequency-domain methods for Maxwells equations in a planewave basis", Opt. Express **8**, 173–190 (2001).
[20] D. E. Aspnes, "Local-field effects and effective-medium theory: a microscopic perspective", Am. J. Phys. **50**, 704–709 (1982).
[21] E. Silvestre, T. Pinheiro-Ortega, P. Andrés, J. J. Miret, and A. Ortigosa-Blanch, "Analytical evaluation of chromatic dispersion in photonic crystal fibers", Opt. Lett. **30**, 453–455 (2005).
[22] B. Tatian, "Fitting refractive-index data with the Sellmeier dispersion formula", Appl. Opt. **23**, 4477–4485 (1984).
[23] L. Zhang, C. Bao, V. Singh, J. Mu, C. Yang, A. M. Agarwal, L. C. Kimerling, and J. Michel, "Generation of two-cycle pulses and octave-spanning frequency combs in a dispersion-flattened micro-resonator", Opt. Lett. **38**, 5122–5125 (2013).
[24] S. K. Selvaraja, W. Bogaerts, P. Dumon, D. V. Thourhout, and R. Baets, "Sub-nanometer linewidth uniformity in silicon nano-photonic waveguide devices using CMOS fabrication technology", IEEE J. Sel. Top. Quantum Electron. **16**, 316–324 (2010).
[25] R. P. Feynman, "Forces in molecules", Phys. Rev. **56**, 340–343 (1939).
[26] S. G. Johnson, M. Ibanescu, M. A. Skorobogatiy, O. Weisberg, J. D. Joannopoulos, and Y. Fink, "Perturbation theory for Maxwells equations with shifting material boundaries", Phys. Rev. E **65** 066611 (2002).
[27] E. Silvestre, M. V. Andrés, and P. Andrés, "Biorthonormal-basis method for the vector description of optical-fiber modes", J. Lightwave Technol. **16**, 923–928 (1998).
[28] J. D. Jackson, *Classical Electrodynamics*, 3rd ed., (John Wiley & Sons, 1998).

Paper V

Supercontinuum generation based on resonant optical wave-breaking

D. Castelló-Lurbe, V. Torres-Company, and E. Silvestre

to be published.

Supercontinuum generation based on resonant optical wave-breaking

David Castelló-Lurbe[1,*], **Victor Torres-Company**[2], **and Enrique Silvestre**[1]

[1]*Departament d'Òptica, Universitat de València, 46100 Burjassot, Spain*

[*]*david.castello-lurbe@uv.es*

Abstract: Dispersive waves generation from phase matched optical wave-breaking is exploited to produce a coherent mid-infrared near-octave spanning supercontinuum generation. Unlike soliton propagation, the dispersive waves emitted under these conditions can lie in the same dispersion regime of the wavelength where the input pulse is centered. The phenomenon is produced in a dispersion-engineered silicon waveguide, pumping the input pulse at 1.55 μm, where two-photon absorption strongly limits the spectral broadening. By means of a new analytical approach, we derive the phase-matching conditions for such a process. Consequently, this result could be extended to other systems governed by a nonlinear-Schrödinger equation including higher-order dispersion.

OCIS codes: (130.3120) Integrated optics devices, (190.4390) Nonlinear optics, integrated optics.

References and links

1. M. Lipson, "Guiding, modulating, and emitting light on silicon. Challenges and opportunities," J. Lightwave Technol. **23**, 4222–4238 (2005).
2. B. Jalali and S. Fathpour, "Silicon Photonics," J. Lightwave Technol. **24**, 4600–4615 (2006).
3. L. Yin and G. P. Agrawal, "Impact of two-photon absorption on self-phase modulation in silicon waveguides," Opt. Lett. **32**, 2031–2033 (2007).
4. I-W. Hsieh, X. Chen, X. Liu, J. I. Dadap, N. C. Panoiu, C.-Y. Chou, F. Xia, W. M. Green, Y. A. Vlasov, and R. M. Osgood, Jr., "Supercontinuum generation in silicon photonic wires," Opt. Express **15**, 15242–15249 (2007).
5. P. Koonath, D. R. Solli, and B. Jalali, "Limiting nature of continuum generation in silicon," Appl. Phys. Lett. **93**, 091114 (2008).
6. M. Dinu, F. Quochi, and H. Garcia, "Third-order nonlinearities in silicon at telecom wavelengths," Appl. Phys. Lett. **82**, 2954 (2003).
7. Q. Lin, J. Zhang, G. Piredda, R. W. Boyd, P. M. Fauchet, and G. P. Agrawal, "Dispersion of silicon nonlinearities in the near infrared region," Appl. Phys. Lett. **91**, 021111 (2007).
8. A. D. Bristow, N. Rotenberg, and H. M. van Driel, "Two-photon absorption and Kerr coefficients of silicon for 850–2200 nm," Appl. Phys. Lett. **90**, 191104 (2007).
9. R. M. Osgood, Jr., N. C. Panoiu, J. I. Dadap, X. Liu, X. Chen, I-W. Hsieh, E. Dulkeith, W. M. J. Green, and Y. A. Vlasov, "Engineering nonlinearities in nanoscale optical systems: physics and applications in dispersion-engineered silicon nanophotonic wires," Adv. Opt. Photon. **1**, 162–235 (2009).
10. L. Yin, Q. Lin, G. P. Agrawal, "Soliton fission and supercontinuum generation in silicon waveguides," Opt. Lett. **32**, 391–393 (2007).
11. M. Zhu, H. Liu, X. Li, N. Huang, Q. Sun, J. Wen, and Z. Wang, "Ultrabroadband flat dispersion tailoring of dual-slot silicon waveguides," Opt. Express **20**, 15899–15907 (2012).
12. F. Leo, S. Gorza, J. Safioui, P. Kockaert, S. Coen, U. Dave, B. Kuyken, and G. Roelkens, "Dispersive wave emission and supercontinuum generation in a silicon wire waveguide pumped around the 1550 nm telecommunication wavelength," Opt. Lett. **39**, 3623–3625 (2014).

13. L. Zhang, Q. Lin, Y. Yue, Y. Yan, R. G. Beausoleil, and A. E. Willner, "Silicon waveguide with four zero-dispersion wavelengths and its application in on-chip octave-spanning supercontinuum generation," Opt. Express **20**, 1685–1690 (2012).
14. L. Zhang, Q. Lin, Y. Yue, Y. Yan, R. G. Beausoleil, A. Agarwal, L. C. Kimerling, J. Michel, and A. E. Willner, "On-Chip Octave-spanning supercontinuum in nanostructured silicon waveguides using ultralow pulse energy," IEEE J. Sel. Topics Quantum Electron. **18**, 1799–1806 (2012).
15. G. P. Agrawal, *Nonlinear Fiber Optics* (Academic Press, 4th ed., 2007).
16. J. M. Dudley, G. Genty, and S. Coen, "Supercontinuum generation in photonic crystal fiber," Rev. Mod. Phys. **78**, 1135–1184 (2006).
17. A. M. Heidt, A. Hartung, G. W. Bosman, P. Krok, E. G. Rohwer, H. Schwoerer, and H. Bartelt,"Coherent octave spanning near-infrared and visible supercontinuum generation in all-normal dispersion photonic crystal fibers," Opt. Express **19**, 3775–3787 (2011).
18. K. E. Webb, Y. Q. Xu, M. Erkintalo, and S. G. Murdoch, "Generalized dispersive wave emission in nonlinear fibers," Opt. Lett. **38**, 151–153 (2013).
19. M. Conforti and S. Trillo, "Dispersive wave emission from wave breaking," Opt. Lett. **38**, 3815–3818 (2013).
20. D. Castelló-Lurbe, P. Andrés, and E. Silvestre, "Dispersion-to-spectrum mapping in nonlinear fibers based on optical wave-breaking," Opt. Express **21**, 28550–28558 (2013).
21. B. Barviau, B. Kibler, and A. Picozzi, "Wave-turbulence approach of supercontinuum generation: Influence of self-steepening and higher-order dispersion," Phys. Rev. A **79**, 063840 (2009).
22. C. Michel, P. Suret, S. Randoux, H. R. Jauslin, and A. Picozzi, "Influence of third-order dispersion on the propagation of incoherent light in optical fibers," Opt. Lett. **35**, 2367–2369 (2010).
23. C. Finot, B. Kibler, L. Provost, and S. Wabnitz,"Beneficial impact of wave-breaking for coherent continuum formation in normally dispersive nonlinear fibers," J. Opt. Soc. Am. B **25**, 1938–1948 (2008).
24. L. Cohen, *Time-Frequency Analysis* (Prentice Hall, 1995).
25. M. Erkintalo, Y. Q. Xu, S. G. Murdoch, J. M. Dudley, and G. Genty, "Cascaded phase matching and nonlinear symmetry breaking in fiber frequency combs," Phys. Rev. Lett. **109**, 223904 (2012).
26. D. Anderson, M. Desaix, M. Lisak, and M. L. Quiroga-Teixeiro,"Wave breaking in nonlinear-optical fibers," J. Opt. Soc. Am. B **9**, 1358–1361 (1992).
27. G. P. Agrawal, *Fiber-optic communication systems* (Academic Press, 3rd ed. 2002).
28. O. Boyraz, T. Indukuri, and B. Jalali, "Self-phase-modulation induced spectral broadening in silicon waveguides," Opt. Express **12**, 829–833 (2004).
29. J. Wu, F. Luo, Q. Zhang, and M. Cao, "Optical wave breaking of high-intensity femtosecond pulses in silicon optical waveguides", Opt. Laser Technol. **41**, 360–364 (2009).
30. A. C. Turner, C. Manolatou, B. S. Schmidt, M. Lipson, M. A. Foster, J. E. Sharping, and A. L. Gaeta, "Tailored anomalous group-velocity dispersion in silicon channel waveguides," Opt. Express **14**, 4357–4362 (2006).
31. S. Mas, J. Caraquitena, J. V. Galán, P. Sanchis, and J. Mart, "Tailoring the dispersion behavior of silicon nanophotonic slot waveguides," Opt. Express **18**, 20839–20844 (2006).
32. D. Meshulach and Y. Silberberg, "Coherent quantum control of two-photon transitions by a femtosecond laser pulse," Nature **396**, 239–242 (1998).
33. D. Castelló-Lurbe, E. Silvestre, P. Andrés i V. Torres-Company, "Spectral broadening enhancement in silicon waveguides through pulse shaping," Opt. Lett. **37**, 2757–2759 (2012).
34. D. Castelló-Lurbe, V. Torres-Company, and E. Silvestre, "Inverse dispersion engineering in silicon waveguides," accepted in J. Opt. Soc. Am. B.
35. N. Akhmediev and M. Karlsson, "Cherenkov radiation emitted by solitons in optical fibers," Phys. Rev. A **51**, 2602–20607 (1995).
36. S. Afshar V. and T. M. Monro, "A full vectorial model for pulse propagation in emergin waveguides with sub-wavelength structures. Part I: Kerr nonlinearity," Opt Express **17**, 2298–2318 (2009).
37. V. P. Tzolov, M. Fontaine, N. Godbout and S. Lacroix, "Nonlinear self-phase-modulation effects: a vectorial first-order perturbation approach," Opt. Lett. **20**, 456–458 (1995).
38. B. Tatian, "Fitting refractive-index data with the Sellmeier dispersion formula," Appl. Opt. **23**, 4477–4485 (1984).
39. J. Dudley and S. Coen, "Coherence properties of supercontinuum spectra generated in photonic crystal and tapered optical fibers," Opt. Lett. **27**, 1180–1182 (2002).

1. Introduction

Silicon-on-insulator (SOI) is a material platform of great interest for all-optical on-chip signal processing. Some of its main advantages are CMOS compatibility and strong third-order nonlinear optical effects enhanced by a tight optical confinement due to its high-index contrast [1, 2]. Among other functions, on-chip light generation can get particular benefit of this last feature. However, it has been demonstrated both numerically and experimentally that si-

licon nonlinear losses limit significantly the spectral broadening ability of this platform when pumping at telecom wavelengths [3–5]. Indeed silicon nonlinearities measurements indicate that the relative weight of two-photon absorption (TPA) is still high compared to Kerr effect around $1.55\,\mu$m [6–8]. Moreover, for picosecond or longer pulses, free-carriers induced by TPA produce additional effects, namely, free-carrier dispersion (FCD) and free-carrier absorption (FCA), that also affect new frequency generation [9].

Some works addressing these issues have been published. Most of them have exploited higher-order soliton fission and radiative effects to induce the spectral broadening [10, 11], being the input pulse pumped at telecom wavelengths. Recently, this approach has been experimentally demonstrated through a supercontinuum (SC) generation spanning from $1.2\,\mu$m to $1.7\,\mu$m [12]. In [13, 14], the negative impact of TPA was directly reduced by centering the input pulse at $1.81\,\mu$m. In this case, self-phase modulation (SPM) reinforced by a pulse compression leads to the spectral broadening at the first stages. Furthermore an energy transfer to high and low frequencies was observed at later stages. SC spectra have been obtained in these works pumping in the anomalous dispersion regime, where the broadening mechanism can be sensitive to input pulse noise [15, 16]. Here we adopt an entirely different strategy pumping in the normal dispersion regime, where good stability, smoothness and coherence are expected [17]. Nevertheless, it could seem challenging since efficient new frequency production requires anomalous dispersion [4].

Dispersive wave (DW) emission in the normal dispersion regime has been newly pointed out [18] and related to the so-called optical wave breaking (OWB) [19]. Recently, our group has studied this process by means of an analytical approach to justify a dispersion-to-spectrum mapping achieved under all-normal dispersion regime [20]. Going one step further, in this work we will firstly apply this new method to find a suitable dispersion profile leading to a resonant OWB enabling the radiation of DW and a SC generation. Secondly, we will exploit this phenomenon to mitigate the impact of nonlinear losses on SC generation pumping at $1.55\,\mu$m in a realistic SOI waveguide obtained by inverse dispersion engineering.

2. Spectral broadening produced by optical wave breaking

Nonlinear pulse propagation in waveguides is usually described by means of the generalized nonlinear Schrödinger equation,

$$\frac{\partial}{\partial z}\tilde{A}(z,\omega-\omega_0) = i\beta_p(\omega)\tilde{A}(z,\omega-\omega_0) + i\gamma_0\mathscr{F}\left[|A(z,t)|^2A(z,t)\right], \tag{1}$$

where A is the complex envelope of the electric field, ω_0 is the carrier frequency, $\beta_p(\omega) = \beta(\omega)-\beta_0-\beta_1(\omega-\omega_0)$, being $\beta(\omega)$ the propagation constant of the mode that supports the pulse propagation and $\beta_k = \partial^k\beta(\omega)/\partial\omega^k|_{\omega=\omega_0}$, γ_0 represents the waveguide nonlinear coefficient evaluated at ω_0 and $\mathscr{F}(\circ) = \int_{-\infty}^{+\infty}\mathrm{d}t\, e^{i(\omega-\omega_0)t}\circ$ is the Fourier transform.

Our group has recently introduced a generalized version of the length scales where SPM and the group-velocity dispersion (GVD) act at each propagation distance z [20],

$$\mathscr{L}_{\mathrm{NL}}^{-1}(z) = \frac{\int_{-\infty}^{\infty}\gamma_0|A(z,t)|^4\mathrm{d}t}{2\int_{-\infty}^{\infty}|A(z,t)|^2\mathrm{d}t}, \qquad \mathscr{L}_{\mathrm{D}}^{-1}(z) = \frac{\int_{-\infty}^{\infty}\beta_p(\omega)|\tilde{A}(z,\omega-\omega_0)|^2\mathrm{d}\omega}{\int_{-\infty}^{+\infty}|\tilde{A}(z,\omega-\omega_0)|^2\mathrm{d}\omega}. \tag{2}$$

These functions satisfy the equality $\mathscr{L}_{\mathrm{NL}}^{-1}(z)+\mathscr{L}_{\mathrm{D}}^{-1}(z) = \mathscr{L}_{\mathrm{NL}}^{-1}(0)+\mathscr{L}_{\mathrm{D}}^{-1}(0)$ [20–22]. In addition, if the inequalities $\mathscr{L}_{\mathrm{NL}}^{-1}(0) \gg \mathscr{L}_{\mathrm{D}}^{-1}(0) > 0$ hold, we can analyze the nonlinear pulse propagation in two steps [20]. Since $\mathscr{L}_{\mathrm{NL}}^{-1} > \mathscr{L}_{\mathrm{D}}^{-1}$ at the first stage, $\delta\omega = -\partial_t\varphi(z_{\mathrm{OWB}},t) \approx -\gamma_0\partial_t|A(0,t)|^2z_{\mathrm{OWB}}/\sqrt{2}$, where $\delta\omega$ is the instantaneous frequency or pulse chirp, φ stands for the phase of A, and $\mathscr{L}_{\mathrm{D}}^{-1}(z_{\mathrm{OWB}}) = \mathscr{L}_{\mathrm{NL}}^{-1}(z_{\mathrm{OWB}})$ defines z_{OWB}, that we consider the OWB

distance. At the second stage, while $\mathscr{L}_{\mathrm{D}}^{-1} > \mathscr{L}_{\mathrm{NL}}^{-1}$, a temporal overlapping between waves in the pulse tails is produced. Consequently, their nonlinear interactions through four wave mixing (FWM) strengthen [17, 20, 23]. Moreover, the degenerate FWM could take place on phase matching if the pump waves involved in such a processes lied in the anomalous dispersion regime [15], $\beta_2(\omega) < 0$, keeping $\mathscr{L}_{\mathrm{D}}^{-1} > 0$. Particularly, we are interested in this work in the spectral broadening towards longer wavelengths, so we will study the interaction between waves in the leading pulse edge. Note that mixing between red-shifted (leading edge) and blue-shifted (trailing edge) frequencies does not play a significant role under these conditions. It allows to study separately the interactions in the leading and trailing edges.

The simplest dispersion curve that can lead to phase matching on red-shifted frequencies is $\beta_2(\omega) = \beta_2 + \beta_3(\omega - \omega_0)$ with $\beta_3 > 0$ [15]. We will address this case here. To determine the frequencies that will overlap we proceed as follows. Firstly, we write $\mathscr{L}_{\mathrm{D}}^{-1}(z) = \sum_{k=2}^{3} \beta_k \mu_k(z)/k!$ where μ_k is the kth normalized moment of the pulse spectrum at the baseband. Attending to [24], $\mu_k(z) = \int_{-\infty}^{\infty} A^*(z,t)(-i\partial_t)^k A(z,t)\mathrm{d}t / \int_{-\infty}^{\infty} |A(z,t)|^2 \mathrm{d}t \approx \int_{-\infty}^{\infty} \delta\omega^k(z,t)|A(z,t)|^2\mathrm{d}t / \int_{-\infty}^{\infty} |A(z,t)|^2\mathrm{d}t$, where we only retain the instantaneous frequency contribution. According to our above reasoning, it leads to $\mu_3 = 0$ if symmetric pulses are considered. With the aim of dealing with β_3 effects, we can consider $-\beta_3$ for $\omega > \omega_0$ due to it does not alter red-shifted frequencies behavior. Equivalently, we can redefine $\mu_k(z) = 2\int_{-\infty}^{0} \delta\omega^k(z,t)|A(z,t)|^2\mathrm{d}t / \int_{-\infty}^{\infty} |A(z,t)|^2\mathrm{d}t$.

The equation that defines z_{OWB} can be expressed as $2\mathscr{L}_{\mathrm{D}}^{-1}(z_{\mathrm{OWB}}) \approx \mathscr{L}_{\mathrm{NL}}^{-1}(0)$, and rewritten under the above approximations and up to third-order dispersion as

$$\frac{1}{\sqrt{2}}\frac{L_{\mathrm{NL}}}{L_{\mathrm{D}}^{(2)}}\sigma_2\zeta_{\mathrm{OWB}}^2 - \frac{1}{6}\frac{L_{\mathrm{NL}}}{L_{\mathrm{D}}^{(3)}}\sigma_3\zeta_{\mathrm{OWB}}^3 = 1, \tag{3}$$

where $L_{\mathrm{NL}} = 1/\gamma P_0$, $L_{\mathrm{D}}^{(k)} = T_0^k/\beta_k$, $\zeta_{\mathrm{OWB}} = z_{\mathrm{OWB}}/L_{\mathrm{NL}}$, $\sigma_k = 2\int_{-\infty}^{0}(\partial_x U)^k U\mathrm{d}x / \int_{-\infty}^{+\infty} U^2\mathrm{d}x$, being U the normalized instantaneous input power. At this point, we concentrate on the degenerate FWM where the frequency corresponding to the minimum chirp, $\delta\omega_{\mathrm{min}}$, acts as pump wave and ω_0 (located at the leading pulse edge) acts as signal wave. Since $\mathscr{L}_{\mathrm{D}}^{-1} > \mathscr{L}_{\mathrm{NL}}^{-1}$ beyond z_{OWB} and in accordance to [19,25], the nonlinear contribution of the phase mismatch, κ, can be neglected, $\kappa = \Delta\beta + 2\gamma_0 P_p \approx \Delta\beta = \beta(\omega_i) + \beta(\omega_s) - 2\beta(\omega_p) = 2\sum_{k=1}^{\infty}\beta_{2k}(\omega_p)(\omega_s - \omega_p)^{2k}/(2k)! = \beta_2(\omega_p)(\omega_s - \omega_p)^2$ [15], where P indicates the power, p, s and i stands for pump, signal and idler waves, respectively, and a linear dispersion curve has been considered. Now, if phase matching is imposed on this process, $\kappa = 0$, we derive from Eq. (3)

$$\beta_3^2 = \frac{\sqrt{2}}{\varepsilon^2}\left(\sigma_2 - \frac{\sigma_3}{3\varepsilon}\right)L_{\mathrm{NL}}\beta_2^3, \qquad \omega_{\mathrm{res}} - \omega_0 = \frac{-2\beta_2}{\beta_3}, \tag{4}$$

where the equation $\delta\omega_{\mathrm{min}} = -\varepsilon\zeta_{\mathrm{OWB}}/T_0$ defines ε and ω_{res} is the frequency of the idler wave produced due to the interaction, *i.e* the dispersive wave. We want to emphasize some points around Eq. (4). We assume that L_{NL} and $L_{\mathrm{D}}^{(2)}$ allow OWB, *i.e.* the temporal overlapping between waves at the pulse tail [26]. Among the processes enabled by this overlapping, we impose phase matching on the interaction that can lead to the longest wavelength. For a linear disperson curve, it implies that the longest wavelength produced by SPM at z_{OWB}, that is associated to $\delta\omega_{\mathrm{min}}$, corresponds to the zero-dispersion wavelength (ZDW). Furthermore, this process is favored due to the pump power is much higher than the signal power [20] and this choice agrees with [17,23]. Note that this interaction is produced by the evolution experienced by the temporal frequency distribution in the normal dispersion regime. This fact was already pointed out in [18] to explain the overestimate of the resonant DW location when it is analyzed through a cascaded FWM [25] in a regime that allows OWB. We will return to this point later. Therefore, we expect efficient spectral broadening produced by OWB when such a dispersion is considered.

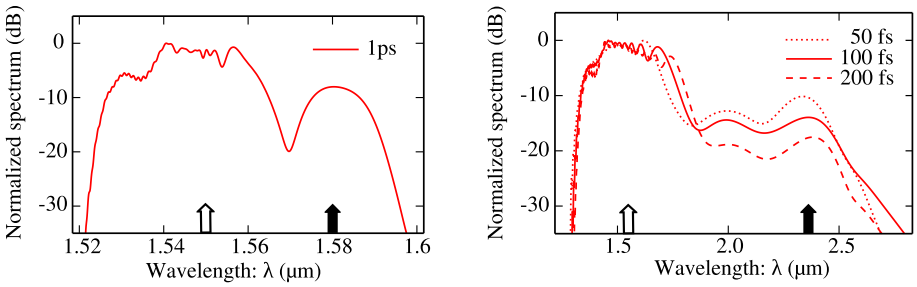

Fig. 1. Output spectrum at the long pulse (a) and (b) short pulse regime pumping at 1.55 μm (open arrow) in the normal dispersion regime after propagation throughout an optical fiber and integrated optical waveguide, respectively (see details in the text). Significant DW emission (solid arrow) induced by optical wave-breaking is observed when β_3 indicated by Eq. (4) is used.

To check the validity of Eq. (4), we consider in Fig. 1 two systems with normal dispersion at the pumping wavelength, $\lambda_0 = 1.55\,\mu$m, and high nonlinearity (to ensure that OWB takes place): one corresponding to an optical fiber, and the other to an integrated optical waveguide. On the one hand, the parameters corresponding to Fig. 1(a) are $\beta_2 = 7.5\,\mathrm{ps^2km^{-1}}$, $\gamma_0 = 2.5\,\mathrm{W^{-1}km^{-1}}$, an hyperbolic secant input pulse with 0.6 kW of peak power and 1 ps of temporal width, that has been taken from Ref. [18] to ensure the temporal overlapping, $\beta_3 = 0.5\,\mathrm{ps^2km^{-1}}$, and a propagation length of 35 m. On the other hand, in Fig. 1(b) we consider $\beta_2 = 0.2\,\mathrm{ps^2m^{-1}}$, $\gamma_0 = 4.0\,\mathrm{W^{-1}m^{-1}}$, a Gaussian input pulse with 1 kW of peak power and 100 fs of temporal width, $\beta_3 = 0.001\,\mathrm{ps^2m^{-1}}$, and a propagation length of 11 mm. In both cases, the conditions $\mathscr{L}_{\mathrm{NL}}^{-1}(0) \gg \mathscr{L}_{\mathrm{D}}^{-1}(0) > 0$ are satisfied and β_3 is calculated by means of Eq. (4). We can observe in Fig. 1 a strong spectral broadening towards longer wavelengths.

Equation (4) leads to $\lambda_{\mathrm{res}} = 1.589\,\mu$m for the case of Fig. 1(a), where the resonance is observed at 1.58 μm, and $\lambda_{\mathrm{res}} = 2.311\,\mu$m for the case of Fig. 1(b), where the resonance is produced at 2.362 μm. Despite of the approximations assumed in our two-step approach, the analytical predictions about β_3 and λ_{res} are in good agreement with the numerical simulations of Eq. (1). It is worth to emphasize the broadband nature of the resonances appeared in Fig. 1. We want to stress here that OWB involves a temporal overlapping of frequencies belonging to the interval $[\delta\omega_{\mathrm{min}}, 0]$. Furthermore, the phase-matching does not significantly increase within this range. This allows to estimate that the bandwidth of each resonance is β_2/β_3, which is in accordance with Fig. 1.

In the next section, we study SC generation in silicon waveguides using short pulses. So, now it is interesting to examine the effects related to the input pulse duration at this regime. Attending to Eq. (4), pulse duration does not affect to the optimum β_3 and consequently, neither the location of the resonant DW (provided, of course, that OWB is produced). That is confirmed in Fig. 1(b), where the resonance peak appears nearly at the same wavelength regardless of the input pulse duration. Notwithstanding, we emphasize that the temporal shift of frequencies is not fully included in our analysis. In fact, Fig. 1(b) illustrates how the energy transfer to longer wavelengths up to the resonance enhances when shorter pulses are injected.

3. Supercontinuum generation in silicon waveguides

For telecom applications, on-chip light sources pumped around 1.55 μm is the preferred choice due to it corresponds to the amplification range of erbium doped fiber amplifiers (EDFAs) [27]. For SOI platform, it remains difficult because TPA highly reduce the effective nonlinearity of

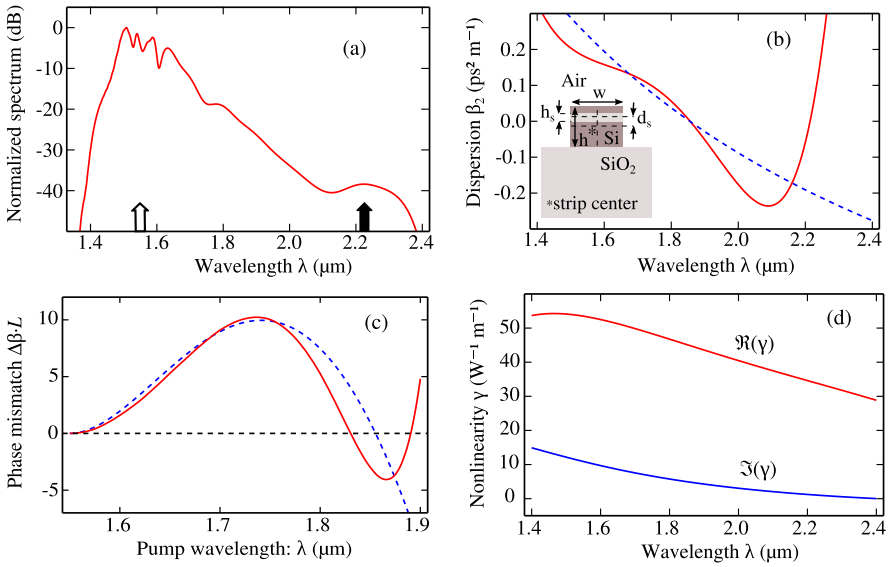

Fig. 2. (a) Output spectrum of a pulse propagated throughout a 1-cm-long waveguide in presence of TPA pumped at 1.55 μm (open arrow). The characteristic lobe generated by resonant OWB is also observed (solid arrow). (b) Target dispersion (dashed line) and dispersion curve (solid line) of the waveguide design, which is shown at the inset, after optimization. (c) OWB phase mismatch corresponding to the target dispersion (dashed line) and the dispersion of the design (solid line). See details in the text. (d) Nonlinear coefficient of the waveguide of (b).

these systems [3, 5]. It becomes even challenging if pumped at the normal dispersion regime, where SPM plays by itself a key role in the new frequency production [28]. In spite of TPA not including in the previous section, it does not necessarily prevent the temporal overlapping required to produce OWB [29]. Therefore, this mechanism could be of great interest. On the one side, the spectral broadening ability of SPM should not be strong enough to generate the whole supercontinuum but induce OWB. On the other side, pump red-shifted waves involved in OWB would be located far from telecom wavelengths and so, the impact of TPA on this additional frequency generation would be smaller. Based on a previous work of us [33], SPM undergone by a skewed input pulse throughout a SOI waveguide should be enough to induce OWB. Moreover, according to [33], for a Gaussian pulse chirped by a cubic spectral phase $\eta(\omega-\omega_0)^3$, we can estimate the optimum skewness as $\eta \sim -0.1\,T_0^3$. For such a pulse, and considering $\gamma_0 = 40 + 8\,i\,\mathrm{W}^{-1}\mathrm{m}^{-1}$, that is not particularly large for SOI waveguides [4, 9], the dispersion coefficients of Fig. 1(b) are an excellent starting point to numerically find the dispersion profile of a SOI waveguide where OWB takes place. We show in Fig. 2(a) the spectrum of a 100-fs-long Gaussian input pulse of 1 kW peak power, skewness $\eta = -0.14\,T_0^3$, $\beta_2 = 0.24\,\mathrm{ps}^2\mathrm{m}^{-1}$ and $\beta_3 = 0.0012\,\mathrm{ps}^3\mathrm{m}^{-1}$. Note that this result corresponds to a simulation done by numerically solving Eq. (1) with a complex γ_0.

The results obtained confirm the possibility of generating SC spectra under significant TPA losses (note we considered $\Im(\gamma_0)/\Re(\gamma_0) = 0.2$ in accordance with [7, 8]). The physical processes included in our previous analysis, namely, GVD, SPM, and TPA, possess a major impact on short pulse propagation in silicon waveguides [4, 10]. Nevertheless, processes such as

higher-order dispersive effects, FCD, FCA or self-steepening must also be included in a realistic description. So, this section will be devoted to find a realistic waveguide where the physical behavior previously described takes place and perform a complete simulation of a pulse propagation throughout it.

The dispersion profile that we found above defines a curve that can be used as a target in our inverse dispersion engineering approach [34] to find a realistic SOI waveguide recovering this dispersion profile. We choose a strip silicon waveguide with one horizontal silica slot to achieve the above goal [13]. Our inverse design algorithm provides, after convergence, a structure with $w = 840\,\text{nm}$, $h = 524\,\text{nm}$, $h_s = 39\,\text{nm}$, and $d_s = 108\,\text{nm}$, where the parameters are defined in the inset of Fig. 2(b). In addition, the dispersion curve of this design and the target profile are also compared in Fig. 2(b). On the basis of our approach, this dispersion curve should induce a phase matched OWB process, with the corresponding emission of dispersive waves. Figure 2(c) shows phase matching around $\lambda = 1.86\,\mu\text{m}$, which, according to our reasoning, should produce a resonance around $\lambda = 2.325\,\mu\text{m}$. It is consistent to the numerical result in Fig. 2(a), where the resonance peak is observed at $\lambda = 2.224\,\mu\text{m}$. Furthermore, Fig. 2(c) confirms that the agreement between both dispersion curves in Fig. 2(b) preserves the location of the phase matching interval, which is actually the key fact. Unlike the output spectrum obtained after propagation throughout a waveguide with the target dispersion profile, the DW lies at the normal dispersion regime for the realistic waveguide, see Fig. 2(b). Right after we will observe that this fact does not prevent the DW emission, in contrast to DW radiated by solitons [25, 35]. In a DW emitted by a soliton-like pulse, the frequencies do not temporally disperse enough to distort the cascaded FWM identified by Erkintalo and co-workers as the underlying fundamental process [18, 25].

Since SOI waveguides have a high index contrast, the vectorial nature of the mode fields must be considered [36]. Therefore, we use the following expression for the nonlinear coefficient [37],

$$\gamma(\omega) = \sum_k \left[\frac{\omega n_2^{(k)}}{c} + i\frac{\beta_{\text{TPA}}^{(k)}}{2} \right] \left[\frac{\rho^{(k)} [n^{(k)}]^2 \varepsilon_0 \int_{\mathscr{S}_k} \left[(\mathbf{e}_\text{t} \cdot \mathbf{e}_\text{t})^2 + \frac{2}{3} \mathbf{e}_\text{t} \cdot \mathbf{e}_\text{t} |e_z|^2 + |e_z|^4 \right] \text{d}S}{2\mu_0 (\int_{\mathscr{S}} (\mathbf{e}_\text{t} \times \mathbf{h}_\text{t}) \cdot \hat{\mathbf{z}}\, \text{d}S)^2} \right], \tag{5}$$

where the subindex k denotes each homogeneous region of the cross-section, $\mathscr{S}_k$, $\mathbf{e}$ and $\mathbf{h}$ represent the electric and magnetic fields of the mode that supports the pulse propagation, the subindex t accounts for the transverse components and z for the longitudinal ones, $\mathscr{S}$ is the cross-section where the fields are defined, n, n_2, and β_{TPA} indicate the refractive index, Kerr index, and TPA coefficient, respectively, and $\rho \approx 1.27$ for silicon and $\rho = 1.0$ for silica stands for the anisotropy coefficient. In addition, following [36], we do not consider the anisotropic contribution of nonlinearity in our waveguides. We calculated n_2 and β_{TPA} for each frequency as the mean value of Cauchy fits of the measurements in [7, 8]. Of course, we also consider the dispersion of both the refractive index of materials [38] and of the mode fields. The nonlinear coefficient of the optimized structure is plotted in Fig. 2(d). It clearly shows how TPA notably affects at telecom wavelengths.

At this point we have properly characterized our waveguide to simulate a pulse propagation. We use an extended version of the nonlinear Schrödinger equation to include free-carrier related processes and higher-order dispersion [3, 4]

$$\begin{aligned} \partial_z \tilde{A}(z, \omega - \omega_0) = &-\frac{\alpha}{2} \tilde{A}(z, \omega - \omega_0) + i[\beta(\omega) - \beta_0 - \beta_1(\omega - \omega_0)] \tilde{A}(z, \omega - \omega_0) \\ &+ i\gamma(\omega) \mathscr{F}\left[|A(z,t)|^2 A(z,t) \right] - \frac{\sigma}{2}(1 + i\mu) \mathscr{F}\left[N_c(z,t) A(z,t) \right], \end{aligned} \tag{6}$$

$$N_c(z,t) = \frac{2\pi [\Im(\gamma_0)]^2}{h\omega_0 \beta_{\text{TPA}}(\omega_0)} \int_{-\infty}^{t} e^{-\frac{t-t'}{\tau_c}} |A(z,t')|^4 \text{d}t', \tag{7}$$

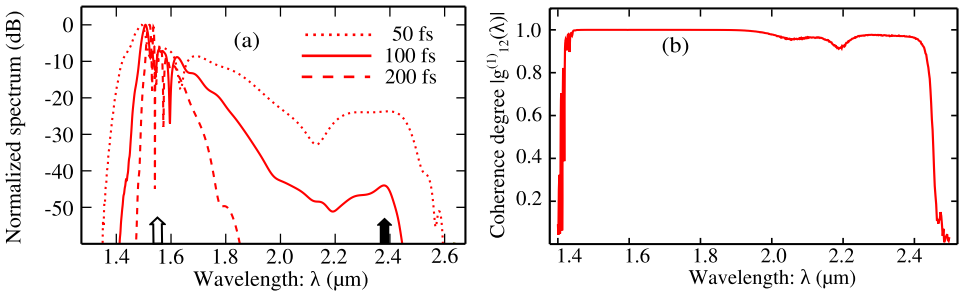

Fig. 3. (a) Output pulse spectra for input pulses of 50 fs at $z = 4$ mm, 100 fs at $z = 8$ mm and 200 fs at $z = 10$ mm. All pulses are pumped at 1.55 μm (open arrow). For 100-fs-long input pulse a lobe centered at 2.379 μm is observed (solid arrow). This resonance also appears for 50-fs-long input pulse but not for the case of 200 fs. (b) Degree of coherence of the pulse ensemble (see details in the text).

where $\sigma = 1.45 \times 10^{-21}$ m^2 is the FCA coefficient, $\mu = 7.5$ accounts for the relative weight of FCD, $\tau_c = 1$ ns represents the carrier lifetime [9], α corresponding to 7 dB cm^{-1} is the linear loss coefficient [14], and ω_0 corresponds to 1.55 μm. With these data, we evaluate the propagation of a Gaussian input pulse with 1 kW of peak power and $T_0 = 100$ fs throughout a 8-mm-long waveguide. Furthermore, we numerically found the optimum skewness, $\eta = -0.16\,T_0^3$, to achieve the broadest spectrum at the output. Figure 3(a) shows the SC spectrum generated spanning from 1.45 μm to 2.4 μm (beyond $2/3$ of an octave) at 45 dB. Moreover, the position of the zero dispersion wavelength in Fig. 2(c) and the location of the resonance in Fig. 3(a) are in agreement with our theoretical scheme based on OWB. Finally, as previously stated, OWB has an additional advantage that is not always achieved by other mechanisms like higher-order soliton fission [11]. Since the input pulse is pumped at the normal dispersion regime, the shot-to-shot fluctuations will not affect the SC obtained, which turns out a key element to reach high performance. This fact is confirmed in Fig. 3(b), where we computed the degree of coherence for an ensemble of 1000 realizations with random input noise of one photon per mode [39].

Finally, we study the impact of input pulse duration on the SC generation in silicon waveguides. In addition to the dispersive effects commented at the end of the previous section, the input pulse duration also affects TPA. Particularly, it gives rise to a shorter z_{OWB} and hence, TPA losses suffered by the pulse during the OWB diminishes. We also plot in Fig. 3(a) the spectra after z_{OWB} for Gaussian pulses with $T_0 = 50$ fs and $T_0 = 200$ fs chirped by means of a cubic spectral phase with skewness $\eta = -0.16\,T_0^3$ (T_0 corresponding to each pulse). For the 50-fs-long input pulse, a SC spanning from 1.35 μm to 2.5 μm (beyond $4/5$ of an octave) at 30 dB is produced. The position of the resonance is very close to the 100 fs case, while a more efficient energy transfer to longer wavelengths is observed. As explained above, the resonant DW is related to the ZDW, which has not been modified. Moreover, the reduction of nonlinear losses can justify the higher spectral powers of the wavelength generated during OWB. For the 200-fs-long input pulse no so broad spectral broadening is observed. In this case, the spectral broadening does not takes place at enough shorter lengths. Unlike the case of 200 fs of Fig. 1(b), here TPA prevents the generation of new frequencies during OWB.

4. Conclusions

OWB has not been so far sufficiently exploited as a SC generation mechanism, at least compared to other processes such as high-order soliton fission that provide, in principle, broader

spectra. However, it is well-known that pumping at the normal dispersion regime allows to reduce the input noise influence and so, achieve better performance. Here we present analytical expressions to compute the third-order dispersion required to improve the spectral broadening induced by OWB and the output spectral width. In a dispersion engineered SOI waveguide and pumping at telecom wavelengths, where TPA is stronger, we obtain a near octave SC spectrum at 30 dB keeping good coherence along all the bandwidth. We expect that this work opens new possibilities to design on-chip light sources.

Acknowledgments

This work was financially supported by the Plan Nacional I+D+I under the research project TEC2008-05490, Ministerio de Ciencia e Innovación (Spain), and by the Generalitat Valenciana under the grant PROMETEO 2009-077. One of the authors, D. C.-L., gratefully acknowledges funding from the Generalitat Valenciana (VALi+d predoctoral contract).